MICROWAVE REMOTE SENSING AND RADAR POLARIZATION SIGNATURES OF NATURAL FIELDS

Prepared for
NATIONAL AERONAUTICS AND SPACE ADMINISTRATION
Goddard Space Flight Center
Greenbelt, Maryland

By

COMPUTER SCIENCES CORPORATION

FINAL REPORT

Under
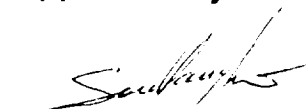
Contract NAS 5-30116
Task Assignment 5183

NOVEMBER 1989

Prepared by: Approved by:

Tsan Mo 11/2/89   *S.Y. Liu* Nov 2, 1989

T. Mo   Date   S. Y. Liu   Date
Task Leader   Manager, Systems and
                                                Engineering Operations

ACKNOWLEDGMENTS

ABSTRACT

This report describes the theoretical models developed for simulation of microwave remote sensing of the Earth surface from airborne/spaceborne sensors. Theoretical model calculations were performed and the results were compared with data of field measurements. Data studied include polarimetric image at the frequencies of P-band (0.45 GHz), L-band (GHz) and C-band (5 GHz), acquired with airborne polarimeters over a test site of agricultural field. Radar polarization signatures from bare soil surfaces and from tree-covered fields were obtained from the data. The models developed in this report include: (1) Small perturbation model of wave scatterings from randomly rough surfaces, (2) Physical optics model, (3) Geometrical optics model, and (4) Electromagnetic wave scattering from dielectric cylinders of finite lengths, which replace the trees and branches in the modeling of tree-covered field. In addition, a three-layer emissivity model for passive remote of vegetation-covered soil surface is also developed. The effects of surface roughness, soil moisture contents and tree parameters on the polarization signatures were investigated.

For bare soil surfaces, it was found that the effects of surface roughness parameters on the polarization signatures are negligibly small. This is primarily due to the normalization process which eliminates the common factor introduced by variation of surface roughness parameters. On the other hand, soil moisture has significant effect on the polarization signatures obtained from the small perturbation and physical optics models. Calculations from both the small perturbation and physical optics models show strong dependence on the radar look angle θ. However, calculated

results at fixed angle θ are insensitive to frequency variation. Comparison of the calculated and observed polarizations signatures shows good agreement, especially for the results at P-band frequency.

For tree-covered fields, the theoretical models were developed for simulating the data of both polarization signature and polarization phase difference. The radius and direction of tree branches are considered as random variables and are allowed to vary in the model. Scattering mechanisms included in the model are: (1) Specular reflection from vertical branches and tree trunk, followed by another Fresnel reflection from the ground surface, (2) Backscattering from non-vertical branches, and (3) Propagation through the canopy, as represented by the forward scattering matrix. The simulated results for both polarization signatures and phase differences are found to be in good agreement with the observations within experimental uncertainty.

The results presented in this report are useful for polarimetric investigation of the interaction between the vegetation canopy and the underlying scattering surface which is ubiquitously involved in the scattering process.

TABLE OF CONTENTS

List of Illustrations

SECTION 1 - INTRODUCTION

Remote sensing techniques using microwave sensors have been developed for many applications (References 1 through 5) in recent years. Recent research emphasis has been placed on measuring soil moisture and vegetation covers (References 6 through 12) on the Earth's surface for global monitoring of renewable resources using spaceborne/airborne sensor systems. These are also considerable interests in using microwave sensors for geological exploration (Reference 13) and subsurface geoarcheological studies (References 14 and 15). Spaceborne sensors are able to provide high-resolution imagery of even the most remote parts of the world, and can produce large quantity of information. Furthermore, microwave signals can penetrate clouds which render visible sensors useless and severely degrade the performance of infrared sensors. Also microwave sensors can be operated either day or night, under clear-sky or cloudy conditions. For these reasons, microwave remote sensing systems are currently being adopted for various practical applications.

Remote sensing is generally classified into two classes: passive and active. For active remote sensing, a sensor (e.g., a radar) sends out a beam of electromagnetic waves and in the same time receives (or detects) the

backscattered waves. For passive remote sensing, the electromagnetic power intensity emitted by a medium, such as a layer of soil, is measured by a microwave sensor (e.g., a radiometer).

Development of theoretical models is essential in understanding how the physical parameters of the scattering medium can affect the measurements, and in interpreting the remote sensing data. Recently, theoretical model developments contribute greatly to the understanding of the physical processes involved in the wave scatterings by vegetation and randomly rough surfaces (References 10 through 12, and 16).

Recent approach (References 17 through 21) to experimental and theoretical work, developed primarily for airborne radar remote sensing, uses the imaging radar polarimeters, to measure both the magnitude and relative polarization phases of the backscattered waves. Using these measured wave magnitude and polarization phase information, one can construct the polarization signatures of the scattering targets. A polarization signature displays the radar scattering cross sections in all possible combinations of polarization states for both the transmit and receive waves, and it provides a convenient way for visualization of the dominant scattering features of scatterers. Recent studies (References 13, 18 and 20) have demonstrated that it is a potentially useful technique for studying the characteristics of the geological surfaces and vegetation covers. From an experimentalist's viewpoint, it would be desirable to have a simple model for parametric description of the scattering media with a minimum number of parameters

necessary to interpret the observed polarization signatures and polarization phase differences (PPD) from various scattering targets.

This report presents some model developments for simulation of the measured polarization signatures obtained from randomly rough surfaces and tree-covered fields. The models are based on the electromagnetic wave scatterings from randomly rough surface and dielectric cylinders of finite lengths and various magnitudes of radius, similar to the tree trunks and branches. The scattering matrix, which relates the incident electric fields to the scattered ones, was firstly obtained from these model calculations, and then its corresponding Stokes matrix was constructed from the elements of the scattering matrix. Polarization signatures were then calculated and displayed in three-dimensional (3-D) plots which are compared with the observations.

The data used in this report were taken with the NASA/JPL airborne imaging radar polarimeter, operating at the P-band, L-band, and C-band frequencies. The flight was over an agricultural area near Raisin City, California. The region under the flight passes had a variety of crops, including cotton, lettuce, bare field, and orchard tree-covered field. Different crops fields produce different polarization signatures and phase difference between the hh- and vv-polarizations. Our primary interests in this report are the polarization signatures. Polarization phase differences over the tree-covered areas and the bare field are also presented. In addi-

tion, a three-layer emissivity model for passive remote sensing of vegetation-covered fields is also developed.

Section 2 gives a brief description of the scattering and Stokes matrix, relating to polarization signatures. The data used in this report are described in Section 3. The results of radar polarization signatures of randomly rough surfaces are described in Section 4, which presents both observations and calculations. Comparison of the two results are also discussed. Section 5 describes the modelling of wave scattering from dielectric cylinders and polarization signatures from tree-covered fields, while polarization phase differences is given in Section 6. Section 7 presents a model for passive remote sensing of vegetation-covered fields. It consist of one vegetation layer and two soil layers, which allow different soil moisture contents in the calculation. A summary and discussion are given in Section 8. Appendix A gives the formulas related to Stokes vectors and Stokes matrix. A user's guide to the Multiview software package, which processes the polarimetric image data, is presented in Appendix B.

SECTION 2 - SCATTERING MATRIX AND STOKES MATRIX

For study of polarization signature, both the incident and the scattered electromagnetic fields are commonly represented by a polarization ellipse (Figure 2-1), which is specified by two angles, the orientation angle ψ, and the ellipticity angle χ, respectively. The backscattering cross sections can be directly expressed in term of the Stokes matrix and these two angles of orientation and ellipticity for both the transmit and receive waves (References 17 and 21).

When a plane radar wave is scattered by a target, its polarized components of the scattered electric field $\mathbf{E}^s$ at the far-zone region can be related to the incident fields $\mathbf{E}^i$ by a 2x2 complex scattering matrix [S]

$$\begin{bmatrix} E_h^s \\ E_v^s \end{bmatrix} = \frac{e^{ikr}}{r} \mathbf{S} \begin{bmatrix} E_h^i \\ E_v^i \end{bmatrix} \tag{2-1}$$

with

$$\mathbf{S} = \begin{bmatrix} S_{hh} & S_{hv} \\ S_{vh} & S_{vv} \end{bmatrix} \tag{2-2}$$

where r is the distance between the scatterer and the receiving antenna, k is the wave number in free space, and the S_{rt} (where the subscripts r, t = h or v) is the scattering matrix element corresponding to a transmit wave with polarization t and receive wave with polarization r, respectively. If the scattering matrix [S] of a target is known, one can construct a 4x4 Mueller matrix [M], which relates the scattered Stokes vector $\mathbf{F}^s$ to the incident Stokes vector $\mathbf{F}^i$ in the form (References 17 and 21)

$$\mathbf{F}^s = \frac{1}{r^2}\left(\mathbf{R}\ \tilde{\mathbf{R}}\ \mathbf{M}\right)\mathbf{F}^i \qquad (2-3)$$

where $\tilde{\mathbf{R}}$ denotes the transpose of $\mathbf{R}$, and the matrices $\mathbf{F}^i$, $\mathbf{M}$, $\mathbf{R}$, and $\mathbf{F}^s$ are defined in Appendix A.

The bistatic scattering cross section for any combination of transmit and receive polarizations is given (References 21)

$$\sigma_{rt}(\psi_r, \chi_r, \psi_t, \chi_t) = 4\pi\ \tilde{\mathbf{Y}}^r\ \mathbf{M}\ \mathbf{Y}^t \qquad (2-4)$$

where (ψ_t, χ_t) and (ψ_r, χ_r) are the orientation and ellipticity angles of the transmit and receive polarizations, respectively. The $\mathbf{Y}^t$ and $\mathbf{Y}^r$ are the normalized Stokes vectors for the transmit and receive waves, and are defined by

$$\mathbf{Y}^t = \begin{bmatrix} 1 \\ \cos 2\psi_t \cos 2\chi_t \\ \sin 2\psi_t \cos 2\chi_t \\ \sin 2\chi_t \end{bmatrix} \quad \text{and} \quad \mathbf{Y}^r = \begin{bmatrix} 1 \\ \cos 2\psi_r \cos 2\chi_r \\ \sin 2\psi_r \cos 2\chi_r \\ \sin 2\chi_r \end{bmatrix} \qquad (2-5)$$

The normalized σ_{rt} in Equation (2-4), as a function of polarizations states, can be displayed in a three-dimensional surface plot, which is called the polarization signature in the literatures (References 17 and 21). According the convention adopted in Reference 17, the polarization of the transmit antenna is taken as the standard one. For co-polarizations, the receive polarization is equal to the transmit polarization and the two angles are related by: $\psi_r = \psi_t$ and $\chi_r = \chi_t$. The cross-polarization signature is obtained by setting $\chi_r = -\chi_t$ and $\psi_r = \dfrac{\pi}{2} + \psi_t$. From Figure 2-1, one can easily see that all linear polarizations occur at $\chi = 0°$. The horizontal polarization is along the direction $\psi = 0°$ and $\chi = 0°$, whereas the vertical polarization is in the direction of $\psi = 90°$ and $\chi = 0°$. Also the left- and right-hand circular polarizations are obtained by setting $\chi = \pm 45°$. These commonly used polarizations are summarized in Table 2-1. The scattering matrix $\mathbf{S}$, as shown in Equation (2-2) contains all the information required for complete representation of the polarization states of a scattering medium. Polarization signature can be obtained if $\mathbf{S}$ is known. Figure 2-2 shows some calculated polarization signatures obtained from three scattering matrices corresponding to three simple scattering models.

Table 2-1. Four commonly used polarizations with corresponding values of χ and ψ.

Polarization	χ	ψ
Horizontal H	0°	0°
Vertical V	0°	90°
Right Circular	−45°	any
Left Circular	45°	any

The first model calculation shown in Figure 2-2 is an istropically scattering sphere with a scattering matrix as described by Van de Hulst (Reference 22)

$$S = \begin{bmatrix} 1 & 0 \\ 0 & 1 \end{bmatrix}$$

(2 − 6)

The backscattering coefficient is unity for both hh- and vv- polarizations, and the backscattering coefficients for cross-polarizations vanish. Figure 2-2a shows that the co-polarization has the largest return along $\chi = 0°$ and its value is independent of the orientation angle ψ. This is because that there is no preferred orientation for a sphere. On the contrary, the cross-polarization shows the lowest return for the linear polarization along $\chi = 0°$ and the highest return for circular polarization along $\chi = \pm 45°$.

The results of a Bragg model is shown in Figure 2-2b which was obtained with a scattering matrix

$$S = \begin{bmatrix} 1 & 0 \\ 0 & 1.5 \end{bmatrix} \qquad (2-7)$$

In this matrix, we have $S_{hh} < S_{vv}$, therefore the vv-polarization in the co-polarization is larger than the hh-polarization. According to Reference 18, the scattering from sea water can be accounted for by the Bragg model. It will be shown in Section 3 that observed polarization signatures from some smooth and moderately rough soil surfaces are also similar to this Bragg model results.

Figure 2-2c shows the results which represent a dielectric dihedral corner reflector model. The scattering matrix for this model is of the form

$$S = \begin{bmatrix} -1.25 & 0 \\ 0 & 1 \end{bmatrix} \qquad (2-8)$$

It requires that the matrix elements S_{hh} and S_{vv} differ in sign and that $|S_{hh}| > |S_{vv}|$. For example, the Fresnel reflection coefficients from a smooth surface usually have such characteristics. Figure 2-2c shows that two minima in the co-polarization and two maxima in the cross-polarization occur at $\psi = 45°$ and $135°$, respectively.

It should be noted that simple models can provide results which are consistent with observed polarization signatures, although one can not role out possibilities of other scattering models.
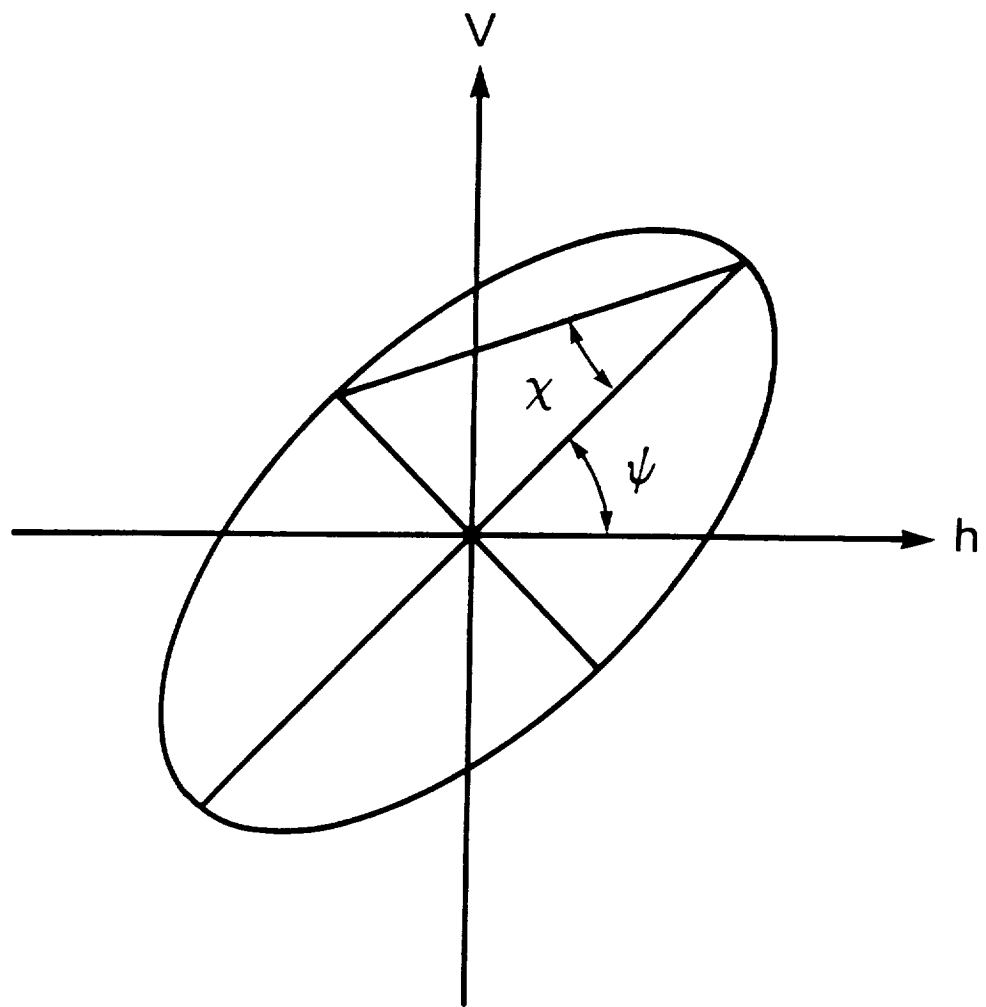
Figure 2-1   Polarization-ellipse geometry for representation of polarization states.
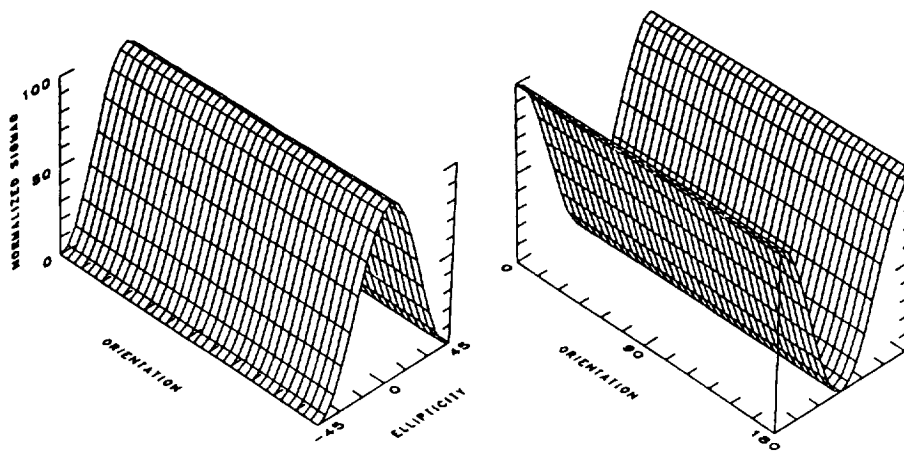
ISOTROPIC SPHERE
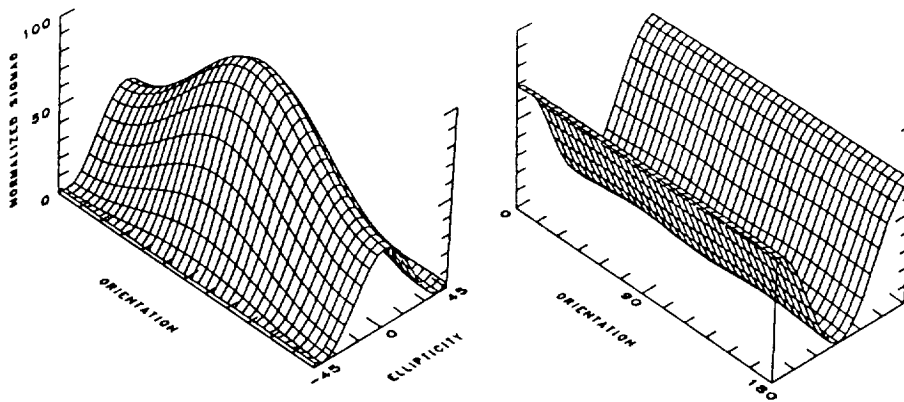
BRAGG
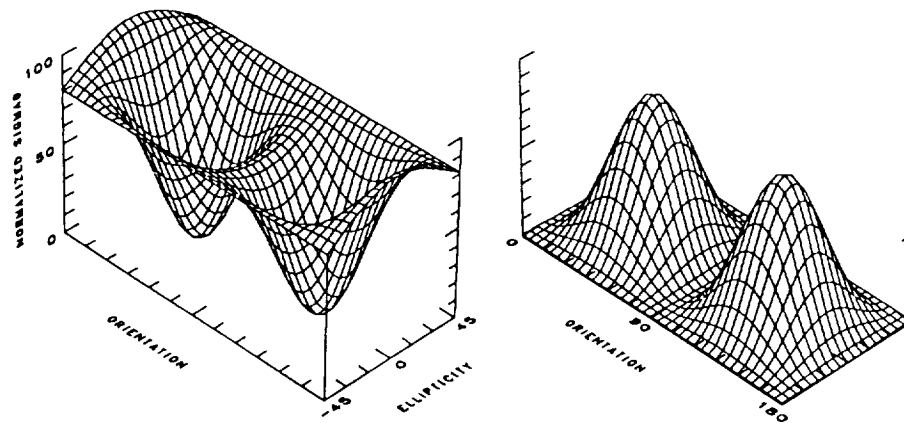
DIHEDRAL CORNER REFLECTOR

Figure 2-2   Polarization signatures of three simple scattering models.

SECTION 3 - DESCRIPTION OF DATA

This section, gives a brief description of the data used in this report. Detailed descriptions of the imaging data processing, using the Multiview software package are presented in Appendix B.

The polarimetric data described here were acquired with the NASA/JPL airborne imaging radar polarimeter operating at the frequencies of 0.45 GHz (P-band), 1.225 GHz (L-band), and 5 GHz (C-band) respectively. Our data were acquired in two flights over a test site of agricultural fields near Raisin City, California. The first flight of data collection was taken on September 28, 1984 and only L-band imaging data were collected. The areas covered during the flight included bare field, tree-covered region and other vegetation-covered fields (References 1 and 23). The second flight was conducted on May 23, 1988 and the polarimetric imaging data for all three bands were acquired simultaneously over the same region which included bare and vegetation-covered fields.

An imaging radar polarimeter measures the amplitude and phase of all elements of the scattering matrix corresponding to each individual pixel in a radar image. Subsequent data processing can synthesize any desired combination of transmit and receive antenna polarization by combining

these scattering matrix elements. In the data processing, the data were compressed for efficient storage on tape. Compression of multipolarized data is based on the validity of reciprocity principle, i.e., the data collected in horizontal-transmit vertical-receive (hv) mode are assumed identical to the data collected in vertical-transmit horizontal-receive (vh) mode. However, in practice the data do not reflect the above condition due to system imperfections and ambient noise, therefore phase calibration of the cross-polarized data is needed before data compression is performed. Initial calibration of the cross-polarized data was performed at JPL so that the average phase difference between hv data and vh data is zero. In addition, phase calibration based on the phase difference of co-polarized data (between hh and vv) is also required in order to remove errors introduced by system imperfections. However, this step may be done after data compression since the compression algorithm does not depend on the accuracy of the phase difference between co-polarized data. The data distributed by JPL do not include this co-polarization phase calibration. The users must perform this calibration by themselves. Typically, one chooses to calibrate the entire image based on measurements of a small area of the image where the phase information is known in terms of theoretical model (Reference 24).

The JPL compressed multipolarization data are phase calibrated in cross-polarization but not in co-polarization. A re-calibration program is included in the Multiview software package (Reference 25) for

co-polarization phase calibration. The program asks the user to choose a small area of the data image. The co-polarization phase difference is calculated for all pixels within the chosen area and then the mean is computed. The co-polarization phases for the entire data image are then re-calibrated based on setting this mean to zero. Here are some suggestions for choosing the area to be used in the RECAL program (Reference 25). The area should be large enough to assure a good statistical set of input data for computing the phase difference between co-polarized signals. Scattering models (Reference 12) predict that the co-polarization phase difference for dry and slightly rough surfaces should be zero. Therefore, one should choose a homogeneous area that is only slightly rough. However, the area chosen should not be too smooth because the backscattering coefficients of smooth areas are susceptible to noise in the system. Instead, this area should be of some uniformly small roughness where the measured backscattering coefficient is bigger than that of the system noise.

The polarimetric data distributed by JPL are in the 10 mega byte compressed format (Reference 25). The Multiview software package, which is an interactive menu-based program, was used to process these data and to synthesize images using various transmit and receive polarization combinations for creating polarization signatures.

The importance of co-polarization phase calibration of the polarization signatures is demonstrated in Figure 3-1 which compares a calibrated

polarization signature with its uncalibrated one. Both were obtained over the same area of a bare field located at $\theta = 20°$. The calibration was performed over a region of 200 pixels within the chosen area over which the polarization signatures were obtained. Figure 3-1 shows that the uncalibrated polarization signature is considerably distorted in shape for both the co- and cross-polarizations and that the calibrated and uncalibrated ones differ significantly. The calibrated co-polarization and cross-polarization in Figure 3-1 are very similar to those of the Bragg model results as shown in Figure 2-2b.
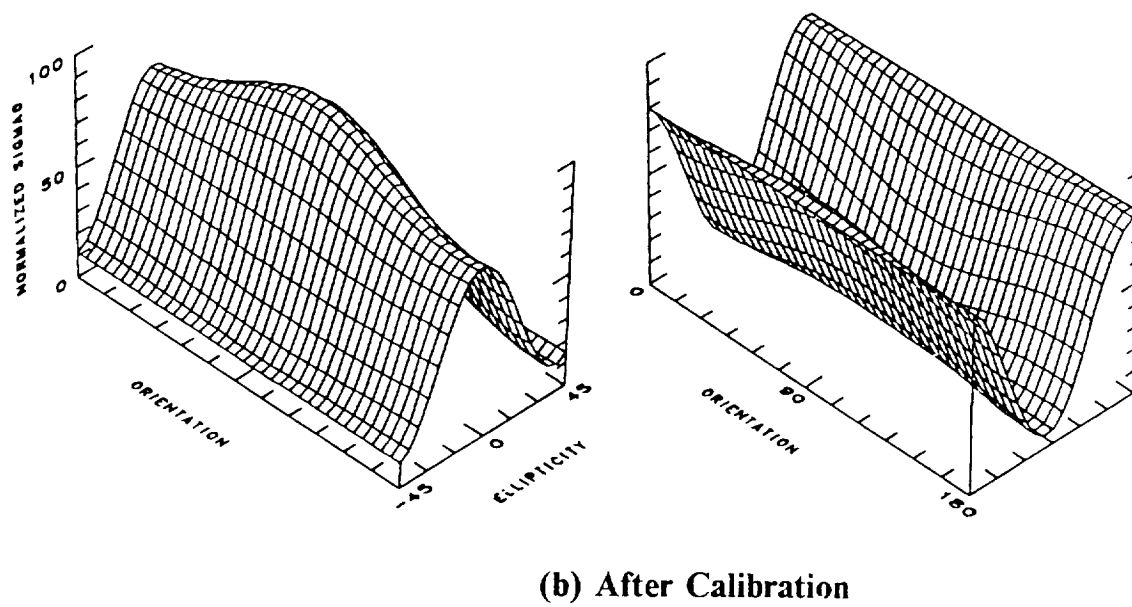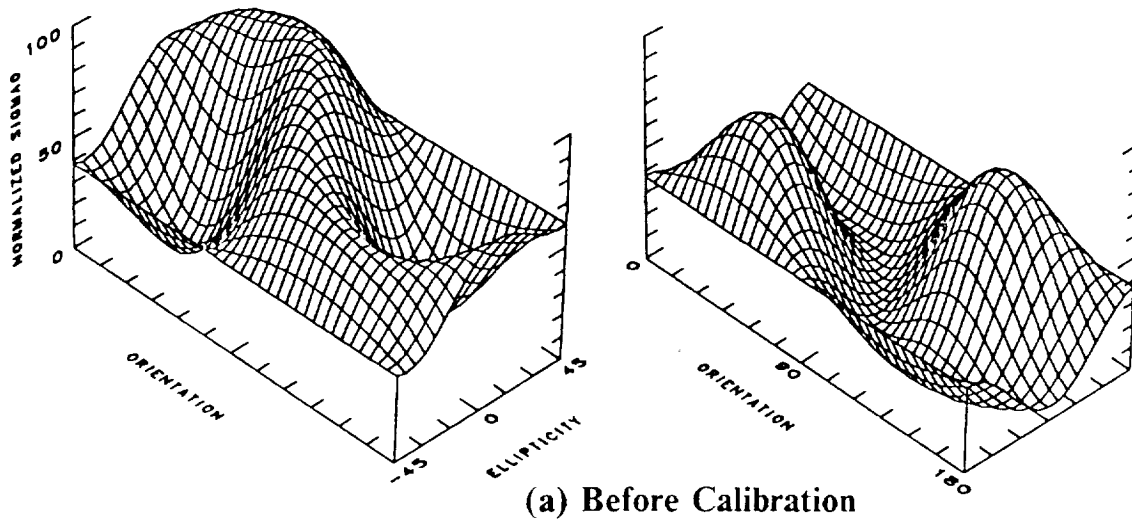
(a) Before Calibration

(b) After Calibration

Figure 3-1   Comparison of calibrated and un-calibrated polarization signatures.

SECTION 4 - RADAR POLARIZATION SIGNATURES OF ROUGH SURFACES

In the microwave remote sensing of vegetation-covered fields, there are underlying rough surfaces involved in the scattering process. Features of the scattering surface are usually imbedded in the observed polarization signatures of vegetation-covered fields (References 19 and 20). Individual effects of surface characteristics, such as surface roughness, soil moisture contents and surface correlation functions on the observed polarization signatures are not fully understood. Furthermore, interaction between the vegetation (e.g. trees) and the underlying scattering surface make it more difficult to determine the surface contribution to the remotely sensed data of a polarization signature, which is supposedly to provide the prominent features of the radar beam illuminated areas (References 17 and 18). Thus, it would be desirable to perform an investigation of the extent the surface characteristic parameters may affect the polarization signature.

In this section, we present some measured polarization signatures of rough soil surfaces obtained with the JPL airborne polarimeter. For comparison, we also performed a series of theoretical model studies of the effect of a rough surface on the polarization signatures. The models included in the study are (References 11 and 12): (1) the small perturbation model, (2) the

physical optics model, and (3) the geometrical optics model. The small perturbation model is suitable for a smooth surface, while the physical and geometrical optics models are appropriate for a moderately rough and very rough surface, respectively. For a very rough surface, the returned radar signals are probably completely unpolarized and the backscattering coefficients for such a rough surface are independent of polarization (i.e., $\sigma^0_{hh} = \sigma^0_{vv}$).

The model calculations of polarization signatures were performed at the frequencies of P-, L-, and C-bands under various conditions of surface roughness and soil moisture contents.

4.1 OBSERVATIONS

The calculated results were also compared with the observed polarization signatures acquired with the NASA/JPL airborne imaging radar polarimeter, operating at the P-band, L-band, and C-band frequencies. The data were taken over an agricultural field near Raisin City, California on May 23, 1988.

Polarization signatures in 3-dimensional (or 3-D) plots were extracted from polarimetric image data, which were properly calibrated according to the method described in Reference 24. A modified version of the JPL MULTIVIEW software package (Reference 25) was used for processing

the observed data of polarimetric Stokes matrix, and for obtaining the observed polarization signatures.

Figures 4-1 through 4-3 show three sets of the three-band plots of observed polarization signatures of rough soil surfaces at the look angles of $\theta = 25°$, $37°$, and $54°$, respectively. There were little vegetation covers on the soil surface at the time of data collection. In these figures, co-polarizations are displayed on the left-hand side, while cross-polarizations are on the right-hand side. The 3-D plots of polarization signatures in these figures demonstrate that there are some changes in the polarization signatures as a function of frequency and the look angle θ, particularly in the co-polarizations. For example, Figures 4-1 and 4-2 show that the hh-polarization ($\psi = 0°$ and $\chi = 0°$) and the vv-polarization ($\psi = 90°$ and $\chi = 0°$) at P-band differ only slightly, however, the corresponding polarizations at $\theta = 54°$ (Figure 4-3) are quite different, and the vv-polarization is dominant. There are also large changes in appearance for the cross-polarizations at P-band as the look angle increases from $\theta = 25°$ to $\theta = 54°$. Another prominent feature shown in Figure 4-3 is that the central peak in the co-polarization signature gradually decreases as the frequency changes from P-band to C-band, while the circular polarization (i.e., $\chi = \pm 45°$) for co- and cross-polarization increases in the mean time.

This increment in circular polarization may be attributed to the un-polarized component (Reference 26) in the returned radar signals due to multiple scattering from rough surfaces, since the relative magnitude of the

roughness to the incident wave length increases as the latter becomes shorter.

These observed polarization signatures will be compared with the theoretical model calculations described in the followings.

4.2 THE MODELS

In this subsection, a brief description of the theoretical models for scattering from a randomly rough surface is presented. The surface roughness is usually characterized by a root-mean-square (rms) surface height, s, which specifies the vertical scale of the surface roughness, and a surface correlation function $\rho(\xi)$, which is a function of the surface correlation lengths ℓ and L, representing the horizontal scales of the surface roughness (References 11 and 12).

The three models described here are the small perturbation model, the physical optics model, and the geometrical optics model. These models have been extensively used for simulation of microwave remote sensing of rough terrains (References 11 and 12). Formulas for the small perturbation and geometrical optics models are relatively simple and were often used for quick applications in the microwave remote sensing work for prediction of backscattering coefficients from rough scattering surfaces. Formulas related to the physical optics model (References 11 and 12) is more complicated than those of other two models, but expressions for

scattering coefficients depending on the correlation function $\rho(\xi)$ exist in literatures (Reference 21).

For application to polarimetric studies, one must specify the 2x2 scattering matrix [S], as defined in Equations (2-1) and (2-2), which relates the polarized components of the incident fields $\mathbf{E}^i$ at the scatterer to the scattered electric field $\mathbf{E}^s$ at the far-zone region. Once the scattering matrix [S] of a target is known, one can construct the 4x4 Stokes or Mueller matrix [M], which can be used to obtain the bistatic scattering cross section in connection with the polarimetric studies for any combination of transmit and receive polarizations (Equation 2-4).

In the first-order approximation of backscattering coefficients, the off-diagonal elements of the scattering matrix [S] vanish (i.e., $S_{hv} = S_{vh} = 0$) for all three scattering models (References 11 and 12). Therefore, there are only two diagonal matrix elements S_{hh} and S_{vv} required to be specified for the three scattering models, which will be described individually.

4.2.1 SMALL PERTURBATION MODEL

For a relatively smooth surface, the first-order small perturbation model can be used to predict the backscattering coefficients from a randomly rough surface. The scattering matrix corresponding to the small perturbation model can be written in the form (Reference 21 and 27)

4-5

$$\mathbf{S} = U_o \begin{bmatrix} S_{hh} & 0 \\ 0 & S_{vv} \end{bmatrix} \qquad (4-1)$$

where

$$S_{hh} = - \frac{2k \cos \theta (\varepsilon - 1)}{\left[\cos \theta + \sqrt{\varepsilon - \sin^2\theta} \right]^2}$$

$$S_{vv} = 2k \cos \theta (\varepsilon - 1) \frac{\sin^2\theta - \varepsilon(1 + \sin^2\theta)}{\left[\varepsilon \cos \theta + \sqrt{\varepsilon - \sin^2\theta} \right]^2} \qquad (4-2)$$

$$U_o = k^2 \cos^2\theta \ W(2k \sin \theta)$$

where ε is the relative dielectric constant of the soil and θ is the incidence angle. $W(2k \sin \theta)$ is the power spectrum (References 11 and 12) of the rough surface sampled at the spatial wave number $2k \sin \theta$.

For a Gaussian surface with a correlation length ℓ, rms surface height s, and correlation function $\rho(\xi) = \exp(-\xi^2/\ell^2)$, the power spectrum is given by (Reference 11)

$$W(2k \sin \theta) = \frac{(s\ell)^2}{2} \exp[-(k\ell \sin \theta)^2] \qquad (4-3)$$

In study of polarization signatures, the backscattering coefficient as defined in Equation (2-4) are usually normalized to the maximum value of the co-polarization signature, therefore a common factor, such as U_0, will be cancelled in the normalization process. In such case, one does not need

to specify the exact form of the power spectrum $W(2k \sin \theta)$ in this small perturbation model.

4.2.2 PHYSICAL OPTICS MODEL

The physical optics model is suitable for a moderately rough surface. In this model, the scattering matrix is not easy to obtain, however, elements of the averaged Mueller matrix [M] are relatively simple in derivation. Ulaby et al. (Reference 21) have derived the averaged modified Mueller matrix, from which one can easily extract the Mueller matrix [M] for backscattering. It should noted that the polarization ellipse for hh- and vv-polarizations used in Reference 21 differs from the one employed in this report which uses the same notations as in References 17 and 18. We have properly modified the results given in Reference 21 to conform with the notations used in this report. The final form for the [M] matrix is given by

$$
\mathbf{M} = (\frac{k}{4\pi})^2 I_p \tilde{R}^{-1}
\begin{bmatrix}
I_{hhhh} & 0 & 0 & 0 \\
0 & I_{vvvv} & 0 & 0 \\
0 & 0 & I_{vvhh} & 0 \\
0 & 0 & 0 & I_{vvhh}
\end{bmatrix}
R^{-1}
\qquad (4-4)
$$

where

$$\mathbf{R} = \begin{bmatrix} 1 & 1 & 0 & 0 \\ 1 & -1 & 0 & 0 \\ 0 & 0 & 1 & 1 \\ 0 & 0 & -i & i \end{bmatrix} \qquad (4-5)$$

and

$$I_p = \begin{bmatrix} 1 & 0 & 0 & 0 \\ 0 & 1 & 0 & 0 \\ 0 & 0 & -1 & 0 \\ 0 & 0 & 0 & -1 \end{bmatrix} \qquad (4-6)$$

The four diagonal matrix elements I_{pqmn} (where the subscripts p, q, m, n = h or v are polarization indices) for backscattering are given by

$$I_{pqmn} = I_n + I_s \qquad (4-7)$$

where

$$I_n = 2\pi a_{pq} \, a^*_{mn} \, e^{-K_0^2} \sum_{n=1}^{\infty} \frac{K_0^{2n}}{n!} \int_0^{\infty} \rho(\xi)^n J_0(2k\xi \sin\theta) \xi \, d\xi \qquad (4-8)$$

$$I_s = 2\pi K_1 \, e^{-K_0^2} \int_0^{\infty} \frac{d\rho(\xi)}{d\xi} J_1(2k\xi \sin\theta) \exp[K_0^2 \, \rho(\xi)] \xi \, d\xi \qquad (4-9)$$

with

$$K_0 = 2ks\cos\theta \qquad (4-10)$$

$$K_1 = -2k\,s^2\cos\theta(b_{pq}\,a^*_{mn} + a_{pq}\,b^*_{mn}) \qquad (4-11)$$

The $J_0(2k\xi\sin\theta)$ and $J_1(2k\xi\sin\theta)$ are the zeroth and first-order Bessel functions, respectively.

The quantities a_{pq} and b_{pq} are given by Ulaby et al. (Reference 21) in terms of surface reflection coefficients and incidence angle θ.

The quantity $\rho(\xi)$ is the surface correlation function. In this study, the function is chosen to be (References 8, 11 and 12)

$$\rho(\xi) = \exp\left[-\frac{\xi^2}{\sqrt{\ell^4 + L^2\xi^2}} \right] \qquad (4-12)$$

This correlation function characterizes a two-scale roughness model with the large scale represented by the correlation length L and the small scale by ℓ. Equation (4-12) reduces to a Gaussian form when ξ approaches zero and becomes exponential when ξ is very large. The two-scale correlation function is more realistic in simulation of the surface roughness condition, according to previous studies (References 8, 11 and 12).

Validity conditions recommended by Ulaby et al. (References 12 and 21) are $\ell\simeq\lambda/6$, $L \geq \lambda$, and $0.05\lambda\lesssim s \gtrsim 0.15\lambda$

4.2.3 GEOMETRICAL OPTICS MODEL

For a very rough surface, the geometrical optics model is appropriate for prediction of backscattering. The backscattering coefficients in this model are independent of polarization (i.e., $\sigma^0_{hh} = \sigma^0_{vv}$) (References 12 and 21). Furthermore, it is expected that the phase difference between the hh- and vv- polarizations is averaged to zero over a finite size of radar footprint for a very rough surface. Therefore the scattering matrix for this model can be written as

$$\mathbf{S} = U_g \begin{bmatrix} 1 & 0 \\ 0 & 1 \end{bmatrix} \qquad (4-13)$$

The factor U_g is dependent on the correlation function. For a Gaussian correlation function with correlation length ℓ and rms surface height s, one can show that (Reference 21)

$$U_g = \frac{R(0)}{\sqrt{8\pi}\, m \cos^2\theta} \exp\left[-\frac{\tan^2\theta}{4m^2} \right] \qquad (4-14)$$

where $m = \sqrt{2}\,(s/\ell)$ and $R(0)$ is the Fresnel reflection coefficient at the normal incidence $\theta = 0°$. As in the case of small perturbation model, the common factor U_g will be cancelled in the normalization procedure for the study of polarization signatures.

This completes the description of three scattering models for scattering surfaces with various scale of roughness. The formulas given here can be

readily applied to simulate polarization signatures observed over selected agricultural fields with little vegetation coverage.

4.3 RESULTS

The formulas given in Section 4.2 are used for simulation of polarization signatures and the simulated results are compared with observations (Figures 4-1 through 4-3) over an agricultural test area with little vegetation coverage.

The calculations of polarization signatures of rough soil surfaces were performed at three radar look angles, $\theta = 25°$, $37°$ and $54°$ (corresponding the observations available) and three volumetric soil moisture values of 0.1, 0.3 and 0.4 gm/cm^3, which correspond to dry, wet and very wet conditions of the soil surface. Results at all three bands were calculated. In addition, the formulas given in Section 4.2 also depend on surface roughness parameters, however, calculations showed that calculated polarization signatures are insensitive to the variation of the surface roughness parameters. This is because of the fact that the polarization signatures are normalized to the maximum value of the co-polarization and the dependence of the surface roughness parameters is cancelled in the normalization process.

The scattering and Stokes matrix, as defined in Equations (4-1) and (4-4) also depend on soil dielectric constant, which is a function of soil moisture and frequency.

An expression for frequency dependence of the dielectric constant of a soil medium consisting of sand, clay, silt and soil moisture given in References 21 and 28 was used to obtain the soil dielectric constant required in calculations. This expression for the dielectric constant is given in the form

$$\varepsilon_s = \varepsilon'_s - j\varepsilon''_s \qquad (4-15)$$

where the real and imaginary parts each fit a polynomial of the form

$$\varepsilon = (a_0 + a_1 S + a_2 C) + (b_0 + b_1 S + b_2 C)m_v + (c_0 + c_1 S + c_2 C)m_v^2 \qquad (4-16)$$

$$\varepsilon = \varepsilon'_s \text{ or } \varepsilon''_s.$$

Here, m_v is the soil volumetric moisture content while S and C are the sand and clay textural components of the soil in percent by weight. The polynomial coefficients are listed in Table 4-1 and the prediction accuracy of the model is given by Hallikainen et al. (Reference 28).

This model is independent of soil temperature. In general, the dielectric constant of soil changes very little with temperature for soil that is not frozen. For soil temperatures below freezing, however, the temperature dependence becomes more important. Variations in the real and imagi-

nary parts of ε_s as a function of temperature and moisture content are shown in Reference 12 (p. 2099).

Table 4-1. Coefficients of Polynomial Expressions for Soil Dielectric Constant

	Freq. (GHz)	a_0	a_1	a_2	b_0	b_1	b_2	c_0	c_1	c_2
ε'_s	1.4	2.862	-0.012	0.001	3.803	0.462	-0.341	119.006	-0.500	0.633
	4	2.927	-0.012	-0.001	5.505	0.371	0.062	114.826	-0.389	-0.547
	6	1.993	0.002	0.015	38.086	-0.176	-0.633	10.720	1.256	1.522
	8	1.997	0.002	0.018	25.579	-0.017	-0.412	39.793	0.723	0.941
	10	2.502	-0.003	-0.003	10.101	0.221	-0.004	77.482	-0.061	-0.135
	12	2.200	-0.001	0.012	26.473	0.013	-0.523	34.333	0.284	1.062
	14	2.301	0.001	0.009	17.918	0.084	-0.282	50.149	0.012	0.387
	16	2.237	0.002	0.009	15.505	0.076	-0.217	48.260	0.168	0.289
	18	1.912	0.007	0.021	29.123	-0.190	-0.545	6.960	0.822	1.195
ε''_s	1.4	0.356	-0.003	-0.008	5.507	0.044	-0.002	17.753	-0.313	0.206
	4	0.004	0.001	0.002	0.951	0.005	-0.010	16.759	0.192	0.290
	6	-0.123	0.002	0.003	7.502	-0.058	-0.116	2.942	0.452	0.543
	8	-0.201	0.003	0.003	11.266	-0.085	-0.155	0.194	0.584	0.581
	10	-0.070	0.000	0.001	6.620	0.015	-0.081	21.578	0.293	0.332
	12	-0.142	0.001	0.003	11.868	-0.059	-0.225	7.817	0.570	0.801
	14	-0.096	0.001	0.002	8.583	-0.005	-0.153	28.707	0.297	0.357
	16	-0.027	-0.001	0.003	6.179	0.074	-0.086	34.126	0.143	0.206
	18	-0.071	0.000	0.003	6.938	0.029	-0.128	29.945	0.275	0.377

The polarization signatures shown in this report were all obtained with clay = 60%, sand = 10%, silt = 30%. The soil moisture dependence of the dielectric constant is included in the formula. These soil textures are approximately the same as the field conditions of our data collection.

The calculated results from the small perturbation model are shown in figures 4-4 through 4-12, while those from the physical optics model are

displayed in Figures 4-13 through 4-21. In all these figures, the calculated co-polarization signatures are plotted on the left-hand side, and the cross-polarization signatures on the right-hand side. The P-band results are on the top part, L-band in the middle and C-band on the bottom. The volumetric soil moisture and look angle θ are also labelled on each plot. Figures 4-4 through 4-6 show the calculated polarization signatures at $\theta = 25°$, 37°, and 54°, respectively, obtained with a soil moisture contents of 0.1 gm/cm^3 from the small perturbation model. Comparison of the results in these figures shows that there are some changes in the pattern of polarization signatures as the look angle θ increases from 25° to 54°, particularly in the co-polarizations which reveal significant variations in the relative magnitudes of hh- and vv-polarization.

Small perturbation model calculations with soil moisture $= 0.3$ gm/cm^3 are shown in Figures 4-7 through 4-9. This soil moisture value is about the same as the field measured value for the field at $\theta = 54°$. These should be compared with corresponding observed results shown in Figures 4-1 through 4-3. Comparison of the calculated and observed results shows that reasonably good agreement between the two results exists, particularly the ones at P-band which has the longest wavelength, and therefore, the surface appears smoother relative to the other two frequencies.

It should be noted that the cross-polarizations along the $\chi = 0°$ direction shows significant changes in both the observed and calculated results as a

function of θ and that the patterns of these changes in the observations and calculations agree well.

Corresponding to a field with very wet soil layer, the small perturbation provides calculated results as shown in Figures 10 through 12, which were obtained with soil moisture value of 0.4 gm/cm^3. Comparison of these calculated polarization signatures of very wet fields with those of fields with less soil moisture contents (Figures 4-4 through 4-9) shows that the relative magnitude between the hh- and vv-polarizations become larger as the soil moisture increases, and that the circular polarizations in the cross-polarizatied signatures decrease.

Calculations with the physical optics model are shown in figure 4-13 through 4-21, which represent the calculated results at three look angles and three different soil moisture values. Equation (4-4) shows that Stokes matrix is a function of the surface roughness parameters (i.e. rms s, small scale correlation length ℓ, and large scale correlation length L). However, actual calculations show that the normalized polarization signatures are insensitive to any variation of these surface roughness parameters. Therefore, the surface roughness parameters were kept at a "standard" set of fixed values of s = 1.2 cm, ℓ = 4.1 cm and L = 25 cm in all the calculations as shown in Figures 4-13 through 4-21. Soil moisture contents do affect the polarization signatures. The effect of soil moisture on the physical optics model results is demonstrated in the plots of Figures 4-13 through 4-21. One can see that the soil moisture effect on the physical

optics model results (at the same angle) is more pronounced than the case of small perturbation model. Comparison of these calculated results with the observed ones (Figures 4-1 through 4-3) shows that the calculations with the volumetric soil moisture of 0.3 gm/cm^3 (Figure 4-16 through 4-18) closely match the observations (Figures 4-1 through 4-3). For example, comparison of the results in Figure 4-18 with those in figure 4-3 shows that both the co-polarization and cross-polarizations at the P-band frequency are in good agreement. The cross-polarization at L- and C-band also agree well. However, there are some differences between the observed and calculated co-polarizations at the L- and C-band.

The polarization signatures generated from geometrical optics model (Equation 4-13) is the same as the polarization signature of an isotropically scattering sphere as shown in Figure 2-3a. Polarization signature obtained from geometrical optics model is independent of frequency, radar look angle, surface roughness parameters and soil moisture contents.

COPOLARIZATION   CROSS-POLARIZATION
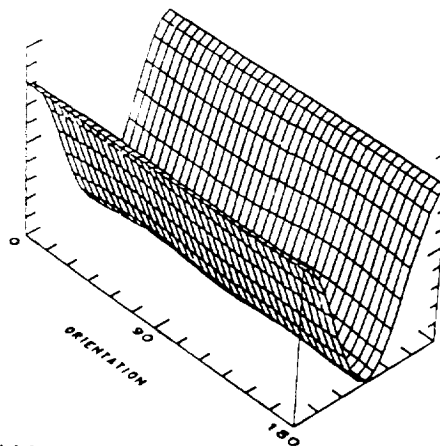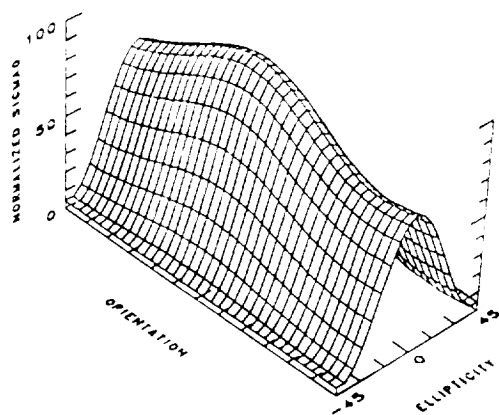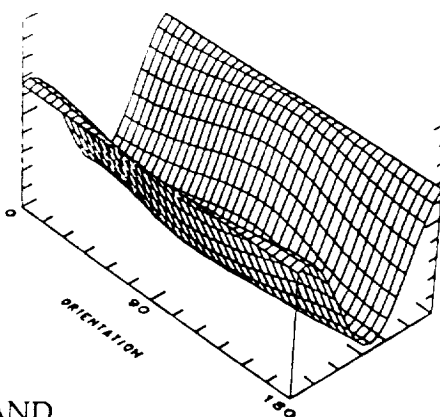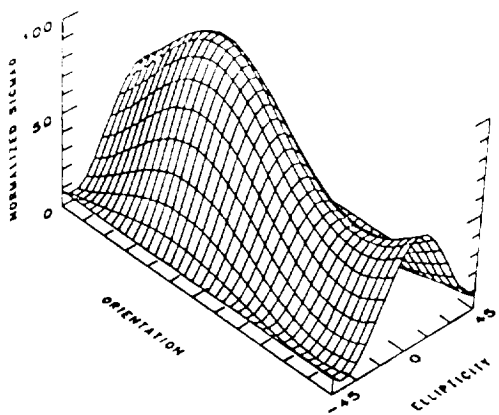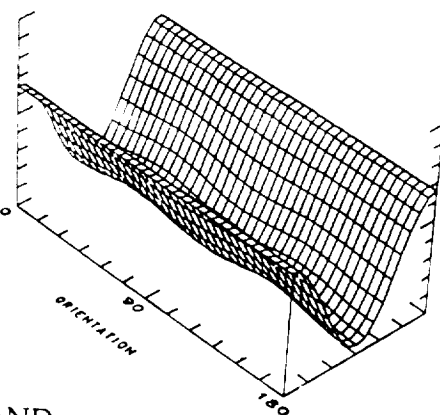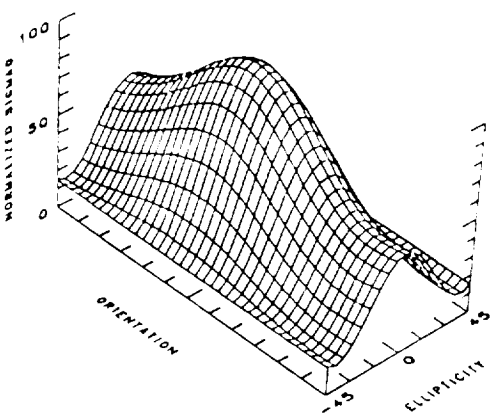
P-BAND

L-BAND

C-BAND

Figure 4-1   Observed polarization signatures at $\theta = 25°$

OBSERVATION

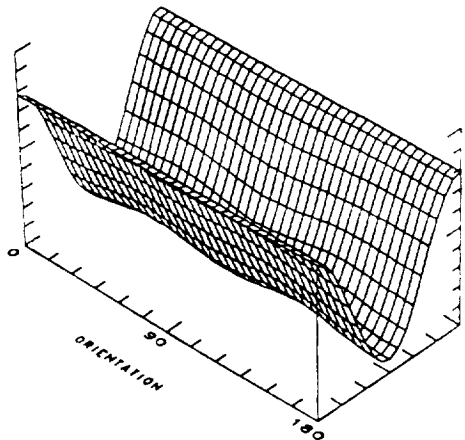COPOLARIZATION   CROSS-POLARIZATION
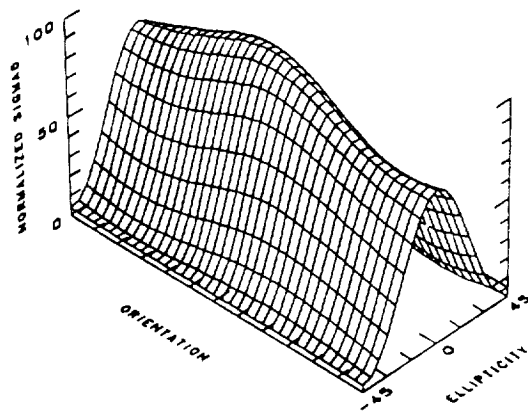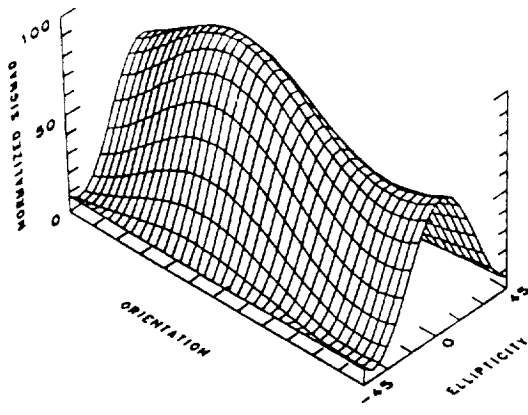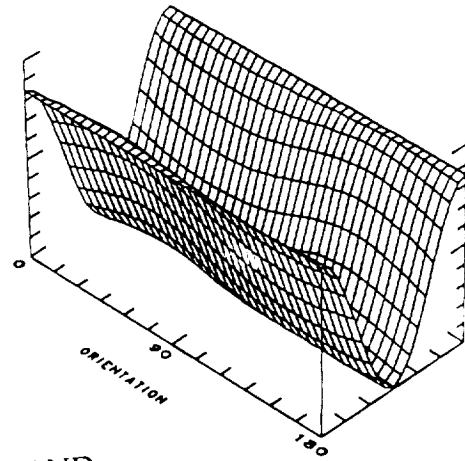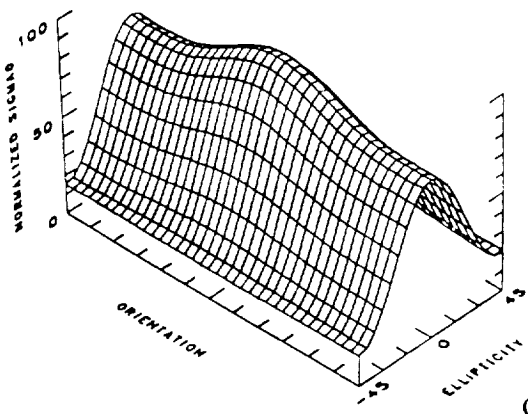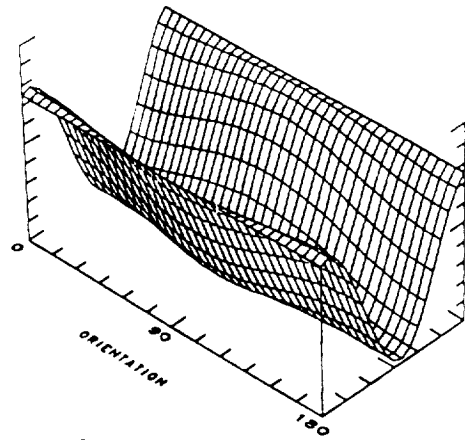
P-BAND

L-BAND

C-BAND

Figure 4-2   Observed polarization signatures at $\theta = 37°$

OBSERVATION

COPOLARIZATION

CROSS-POLARIZATION
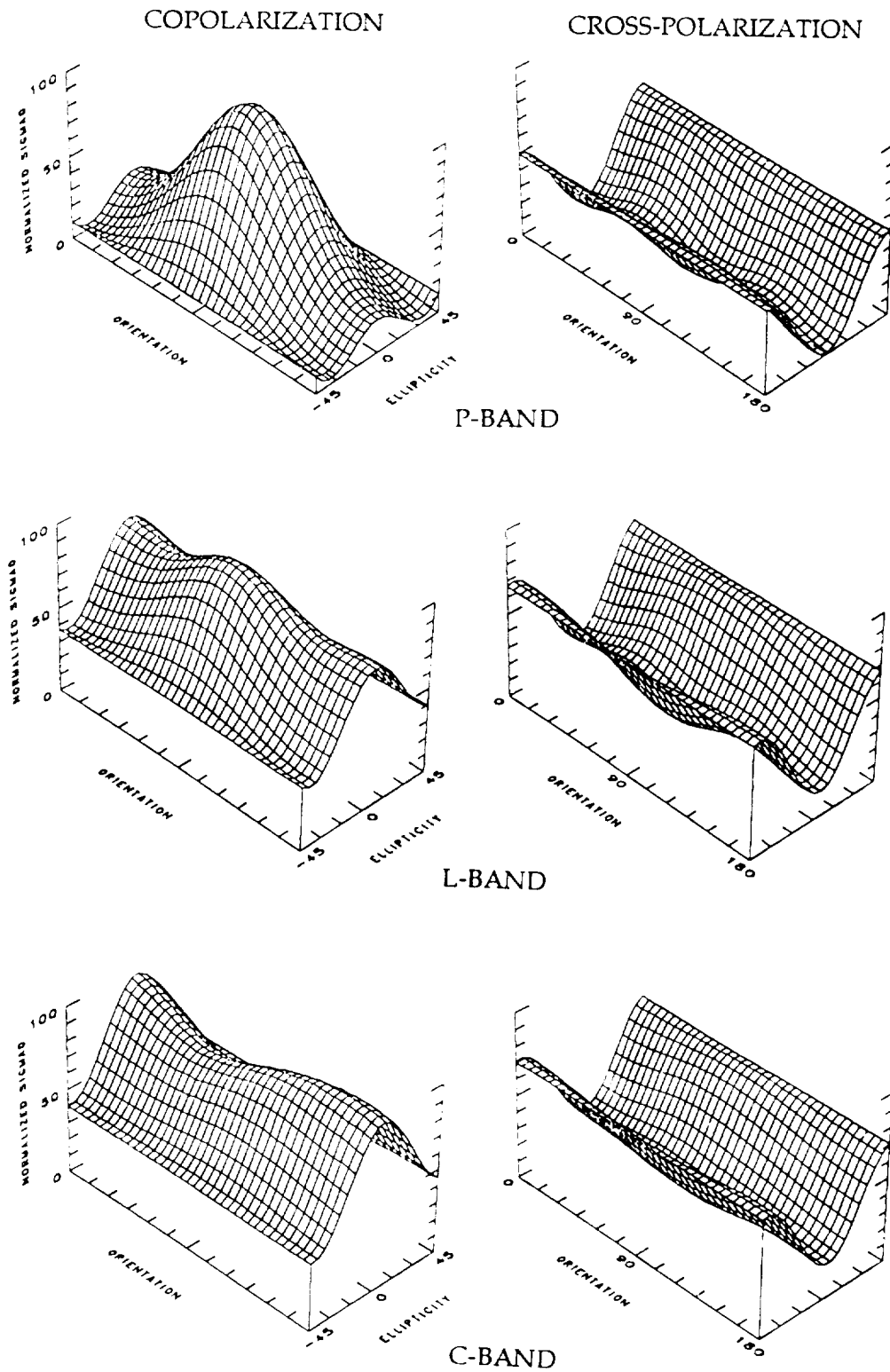
P-BAND

L-BAND

C-BAND

Figure 4-3   Observed polarization signatures at $\theta = 54°$

SMALL PERTURBATION MODEL CALCULATION
Soil Moisture = 0.1 gm/cm^3

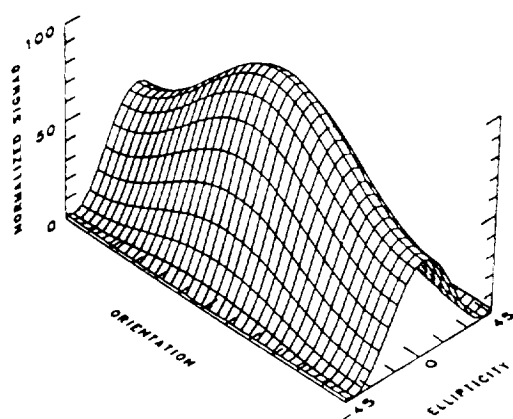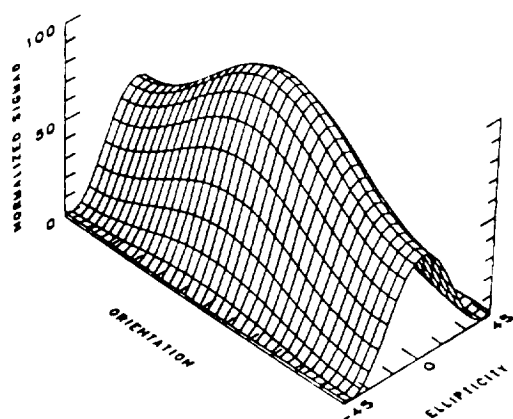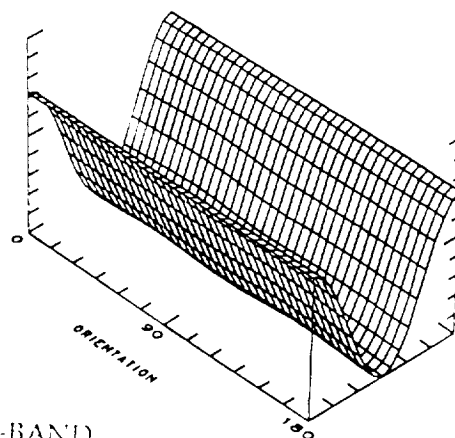COPOLARIZATION   CROSS-POLARIZATION
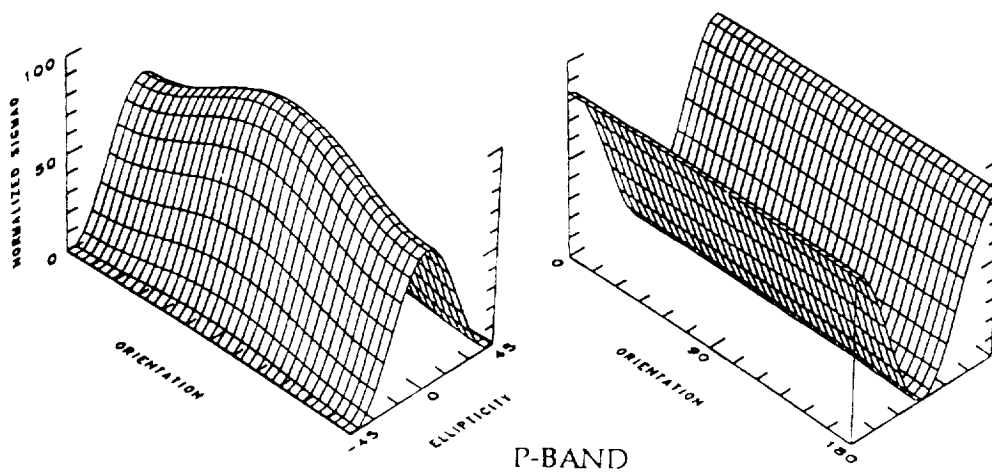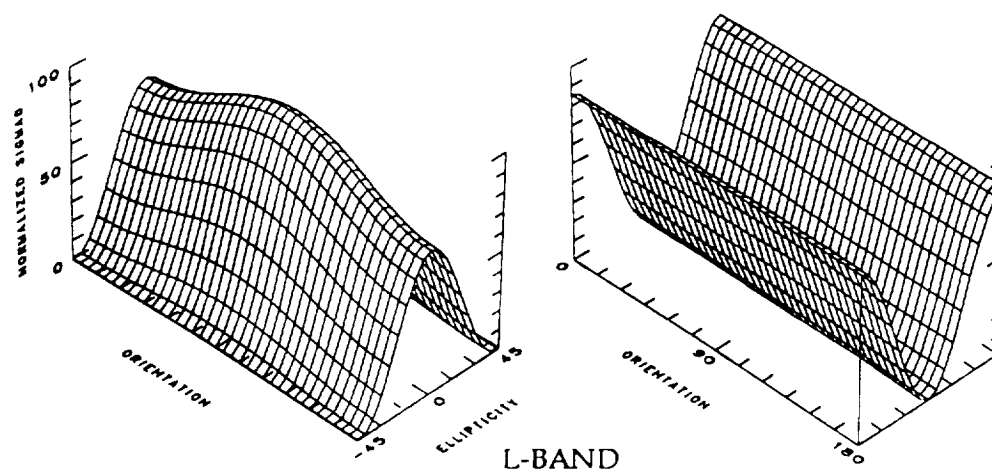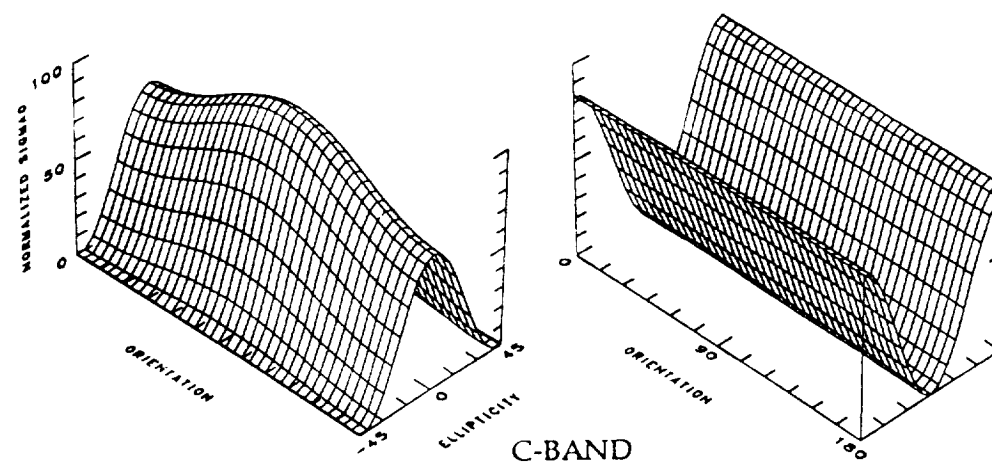
P-BAND

L-BAND

C-BAND

Figure 4-4   Small perturbation model calculations, bare field, $\theta = 25°$, and $SM = 0.1 gm/cm^3$

4-20

SMALL PERTURBATION MODEL CALCULATION
Soil Moisture = 0.1 gm/cm^3

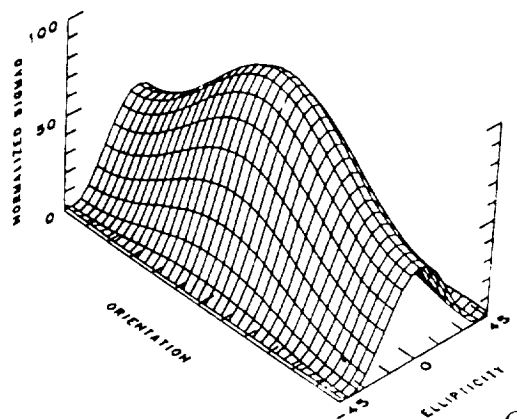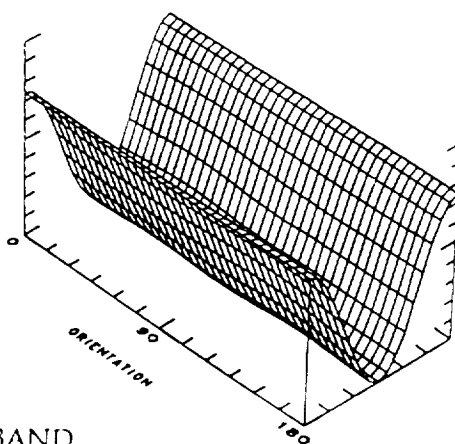COPOLARIZATION   CROSS-POLARIZATION

P-BAND

L-BAND

C-BAND

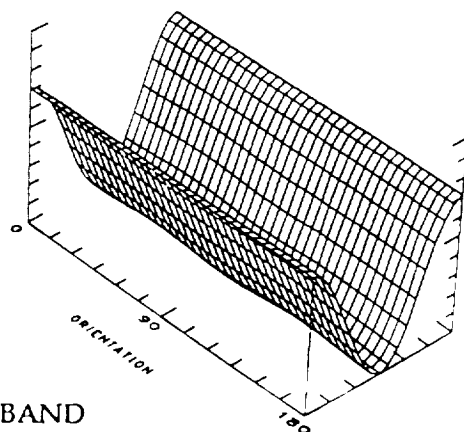Figure 4-5   Small perturbation model calculations, bare field, $\theta = 37°$, and $SM = 0.1 gm/cm^3$

SMALL PERTURBATION MODEL CALCULATION
Soil Moisture = 0.1 gm/cm^3

COPOLARIZATION   CROSS-POLARIZATION

P-BAND

L-BAND

C-BAND

Figure 4-6   Small perturbation model calculations, bare field, $\theta = 54°$, and $SM = 0.1 gm/cm^3$

SMALL PERTURBATION MODEL CALCULATION
Soil Moisture = 0.3 gm/cm^3

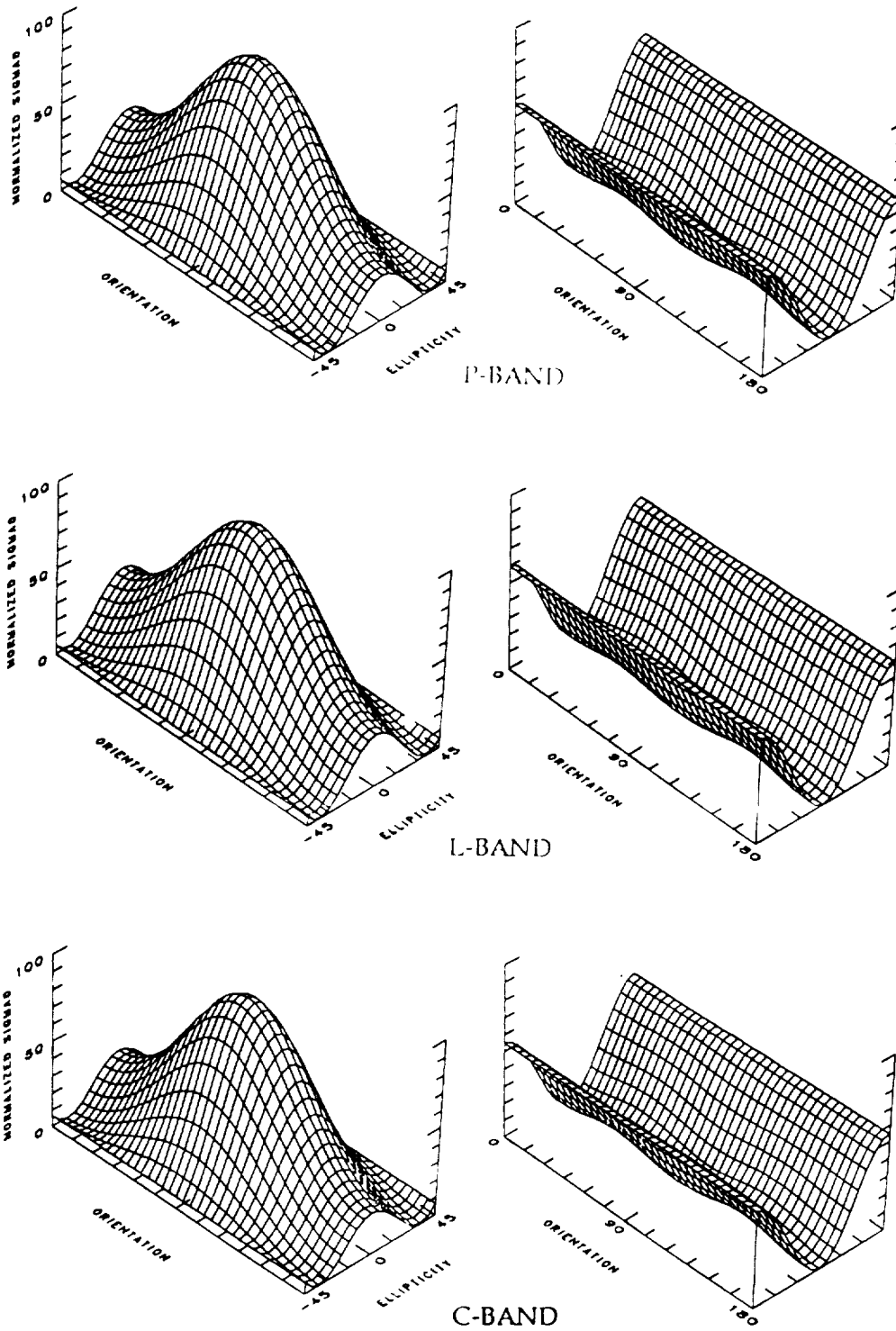COPOLARIZATION   CROSS-POLARIZATION

P-BAND

L-BAND

C-BAND
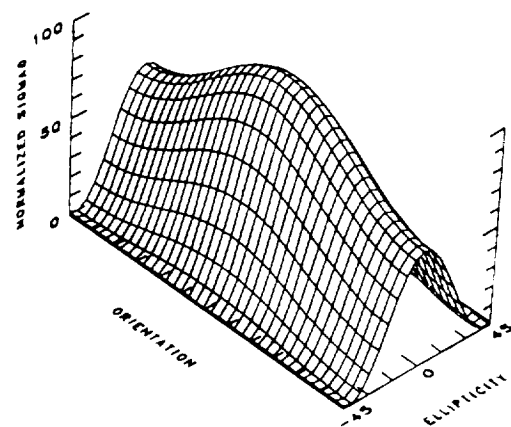
Figure 4-7   Small perturbation model calculations, bare field, $\theta = 25°$, and $SM = 0.3 gm/cm^3$

SMALL PERTURBATION MODEL CALCULATION
Soil Moisture = 0.3 gm/cm^3

COPOLARIZATION   CROSS-POLARIZATION

P-BAND

L-BAND

C-BAND

Figure 4-8   Small perturbation model calculations, bare field, $\theta = 37°$, and $SM = 0.3gm/cm^3$
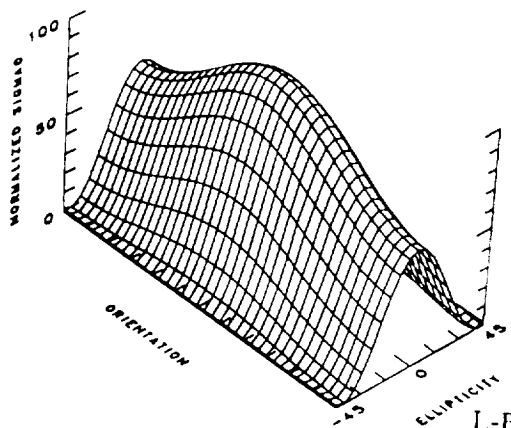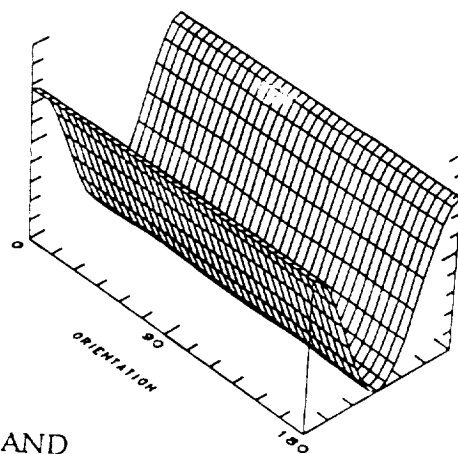
SMALL PERTURBATION MODEL CALCULATION
Soil Moisture = 0.3 gm/cm^3

COPOLARIZATION   CROSS-POLARIZATION

P-BAND

L-BAND

C-BAND

Figure 4-9   Small perturbation model calculations, bare field, $\theta = 54°$, and $SM = 0.3gm/cm^3$

SMALL PERTURBATION MODEL CALCULATION
Soil Moisture = 0.4 gm/cm³

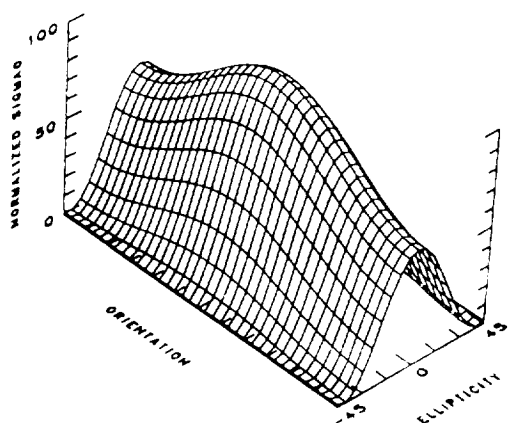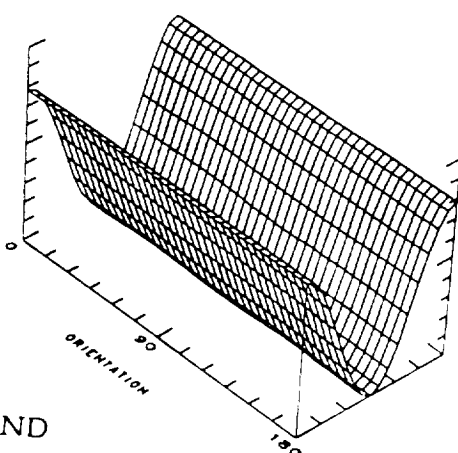COPOLARIZATION   CROSS-POLARIZATION

P-BAND

L-BAND

C-BAND
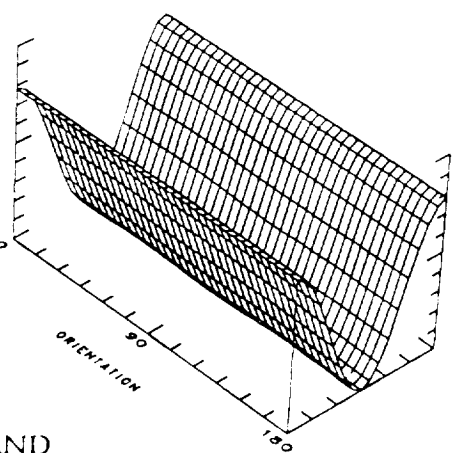
Figure 4-10   Small perturbation model calculations, bare field, $\theta = 25°$, and $SM = 0.4gm/cm^3$

SMALL PERTURBATION MODEL CALCULATION
Soil Moisture = 0.4 gm/cm³

COPOLARIZATION   CROSS-POLARIZATION
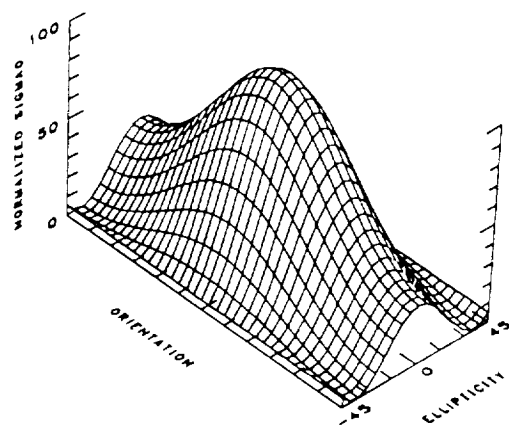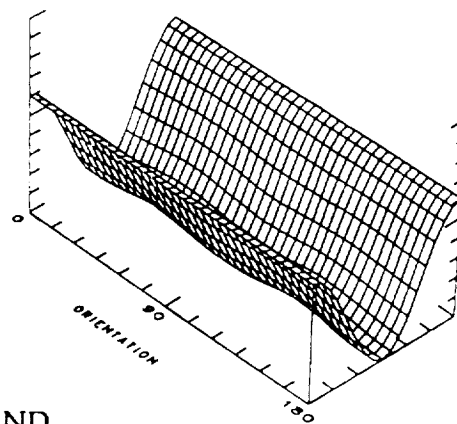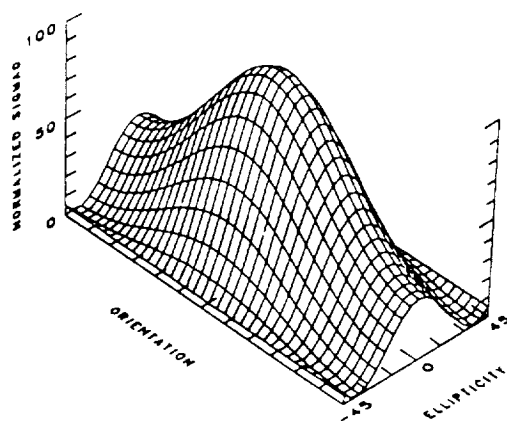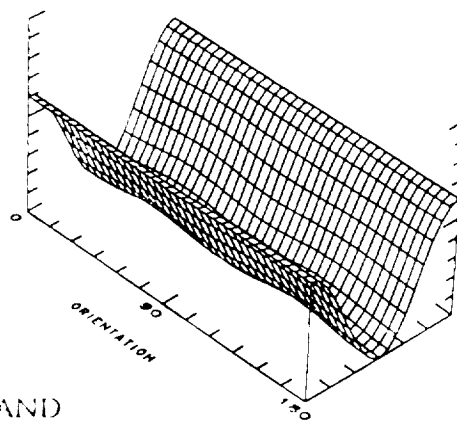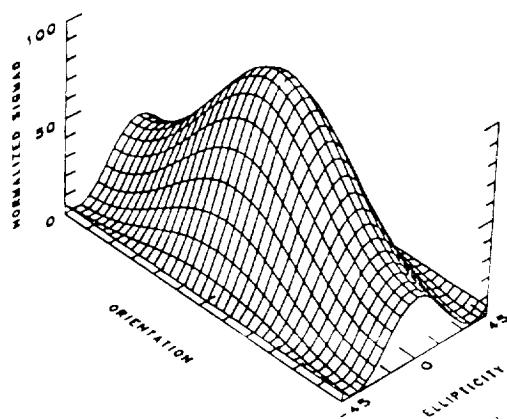
P-BAND

L-BAND

C-BAND

Figure 4-11   Small perturbation model calculations, bare field, $\theta = 37°$, and $SM = 0.4 gm/cm^3$

SMALL PERTURBATION MODEL CALCULATION
Soil Moisture = 0.4 gm/cm^3

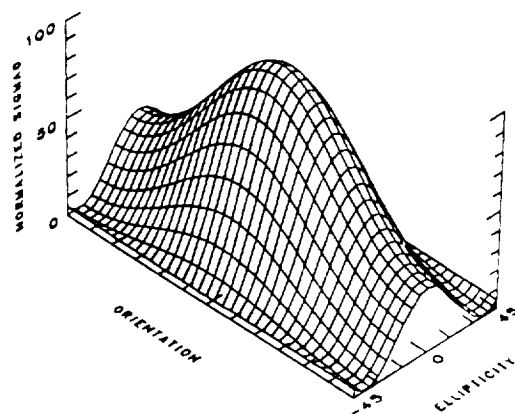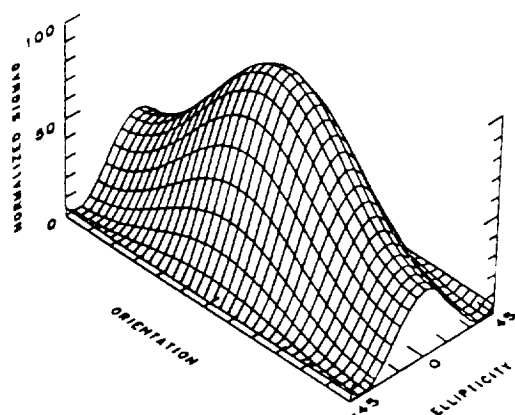COPOLARIZATION   CROSS-POLARIZATION
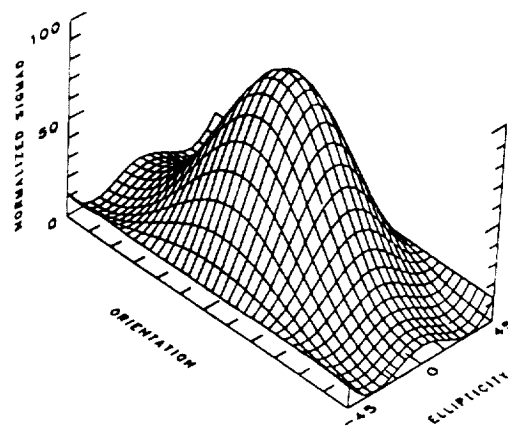
P-BAND
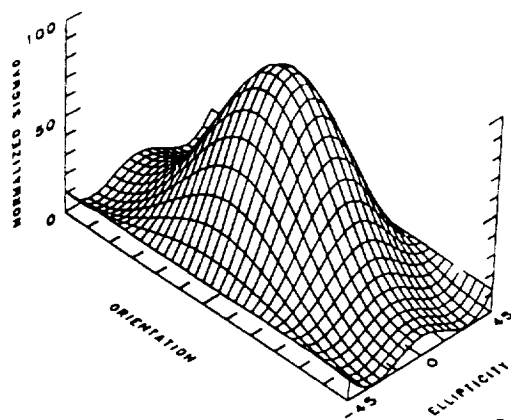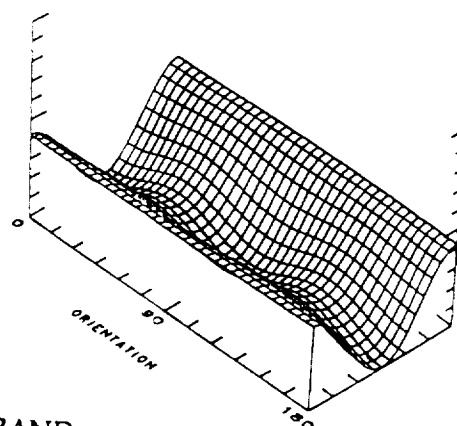
L-BAND
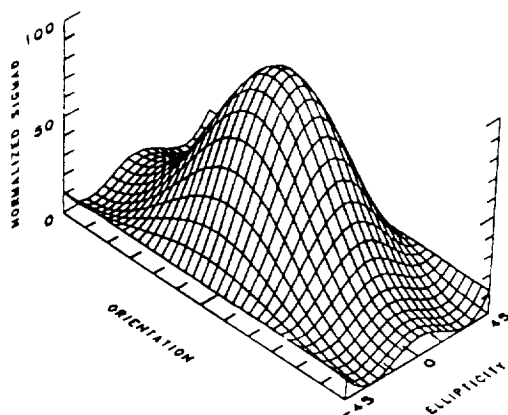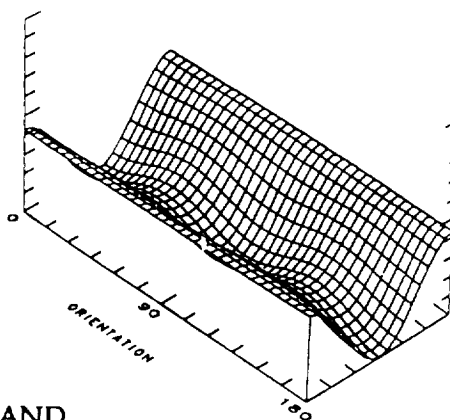
C-BAND
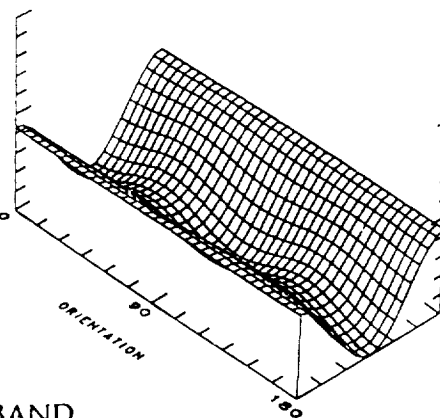
Figure 4-12   Small perturbation model calculations, bare field, $\theta = 54°$, and $SM = 0.4gm/cm^3$

PHYSICAL OPTICS MODEL CALCULATION
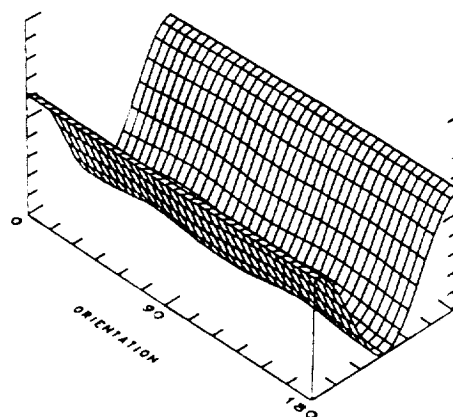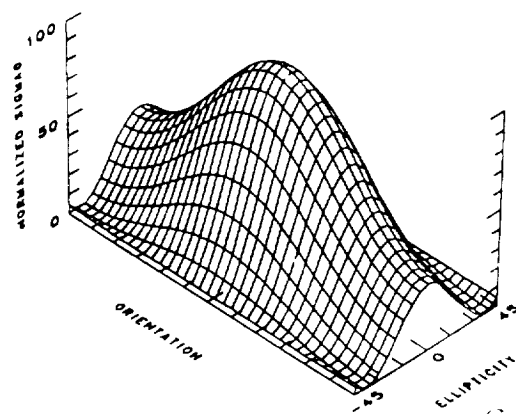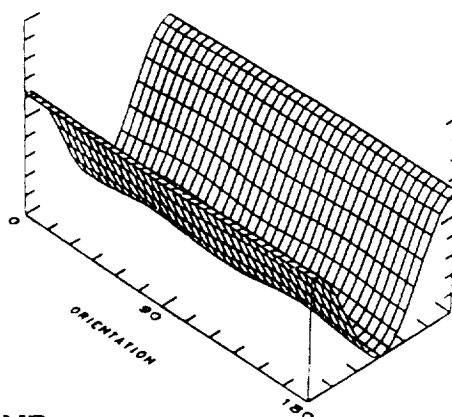## Soil Moisture = 0.1 gm/cm^3

COPOLARIZATION   CROSS-POLARIZATION
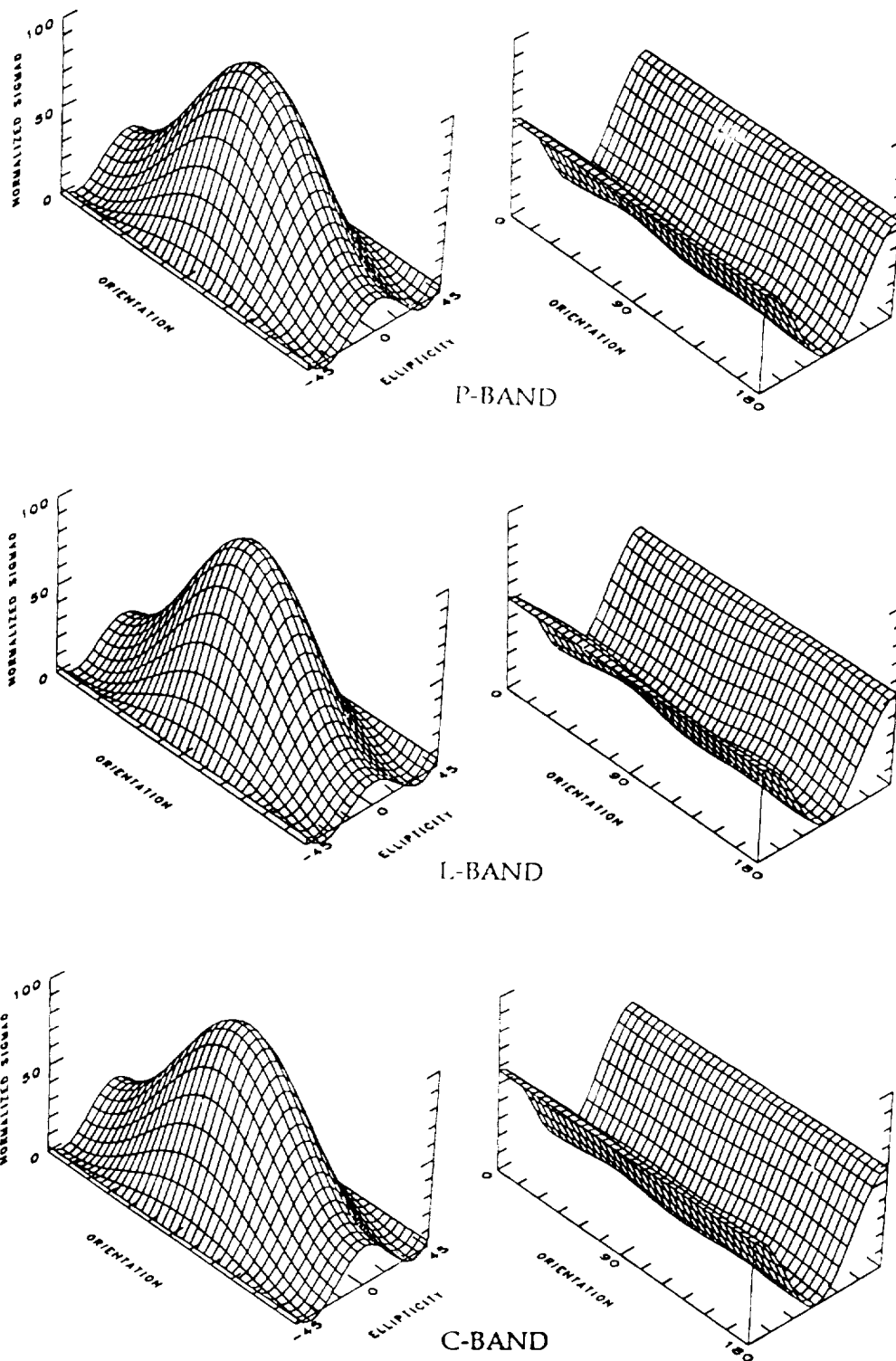
P-BAND

L-BAND

C-BAND

Figure 4-13   Physical optics model calculations, bare field, $\theta = 25°$, and $SM = 0.1 gm/cm^3$

PHYSICAL OPTICS MODEL CALCULATION
Soil Moisture = 0.1 gm/cm^3

COPOLARIZATION   CROSS-POLARIZATION
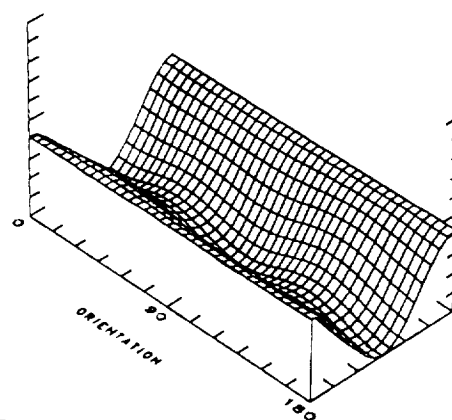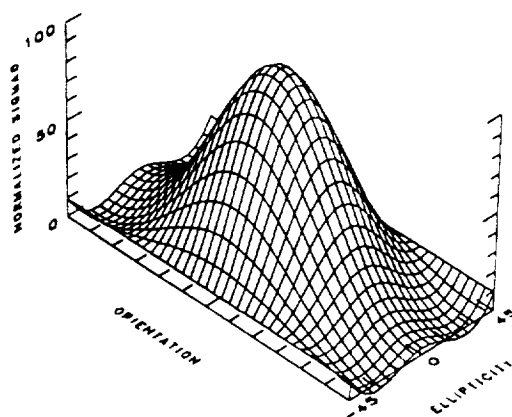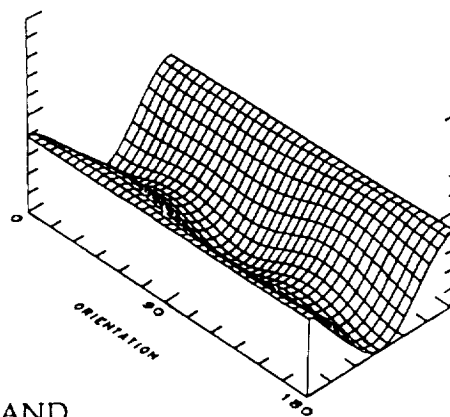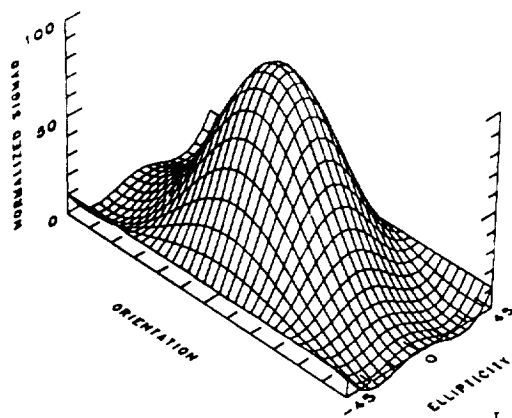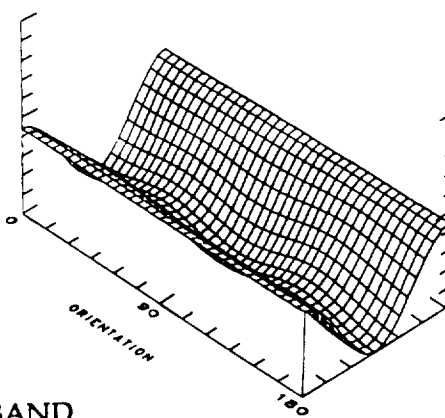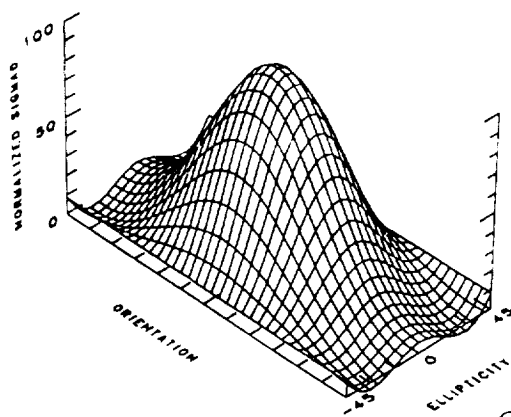
P-BAND

L-BAND

C-BAND

Figure 4-14   Physical optics model calculations, bare field, $\theta = 37°$, and $SM = 0.1 gm/cm^3$

PHYSICAL OPTICS MODEL CALCULATION
Soil Moisture = 0.1 gm/cm^3

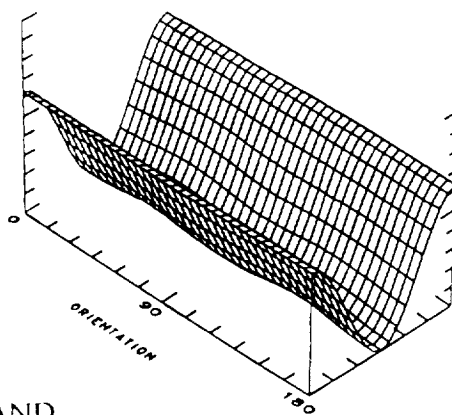COPOLARIZATION   CROSS-POLARIZATION
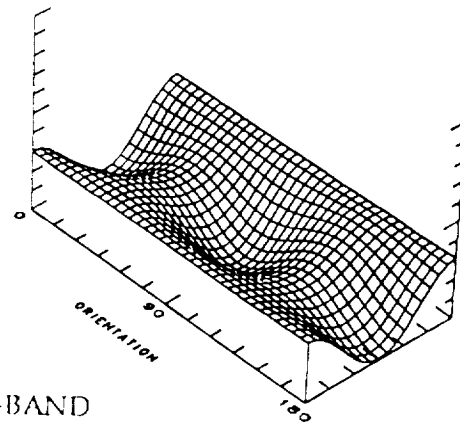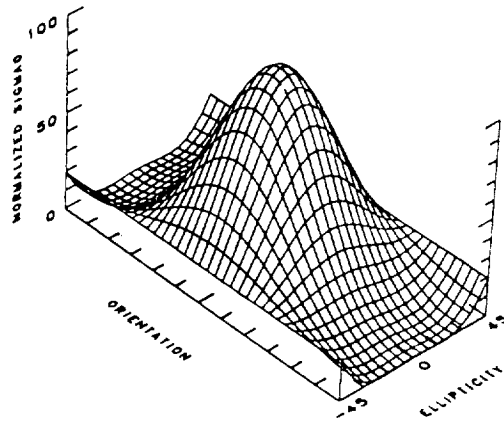
P-BAND
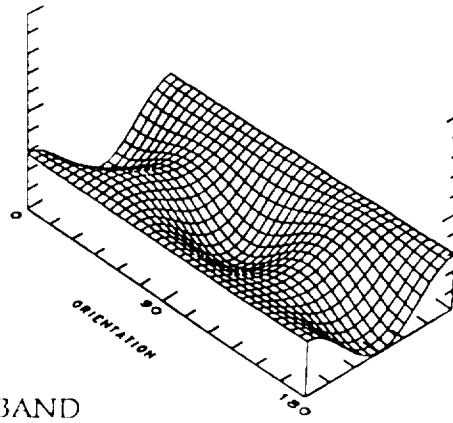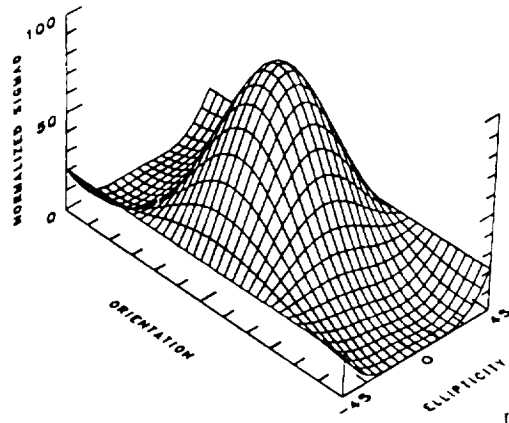
L-BAND
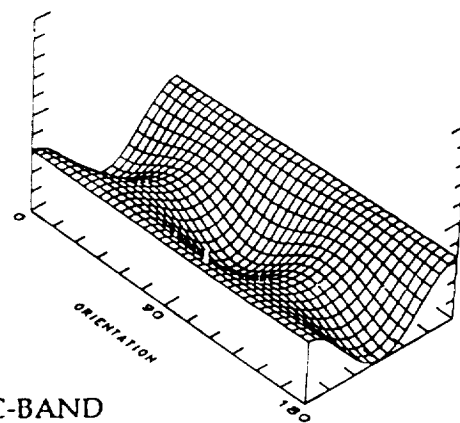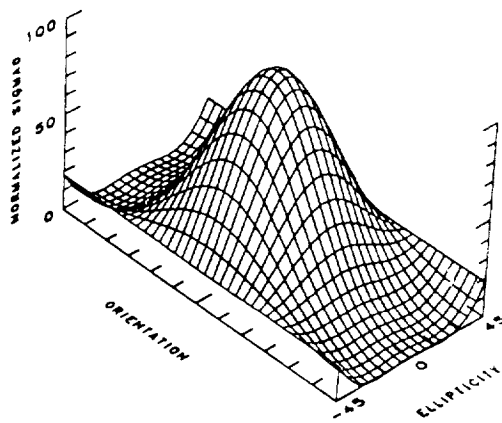
C-BAND

Figure 4-15 Physical optics model calculations, bare field, $\theta = 54°$, and $SM = 0.1 gm/cm^3$

PHYSICAL OPTICS MODEL CALCULATION
Soil Moisture = 0.3 gm/cm^3

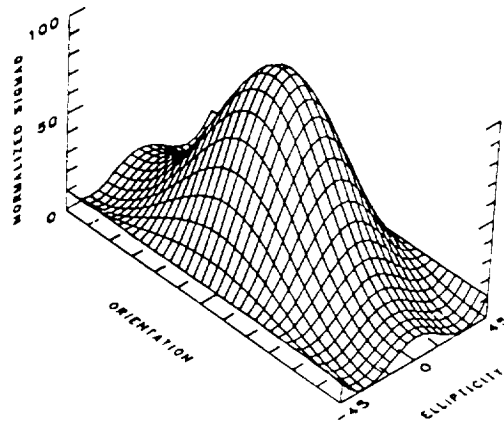COPOLARIZATION   CROSS-POLARIZATION

P-BAND

L-BAND

C-BAND
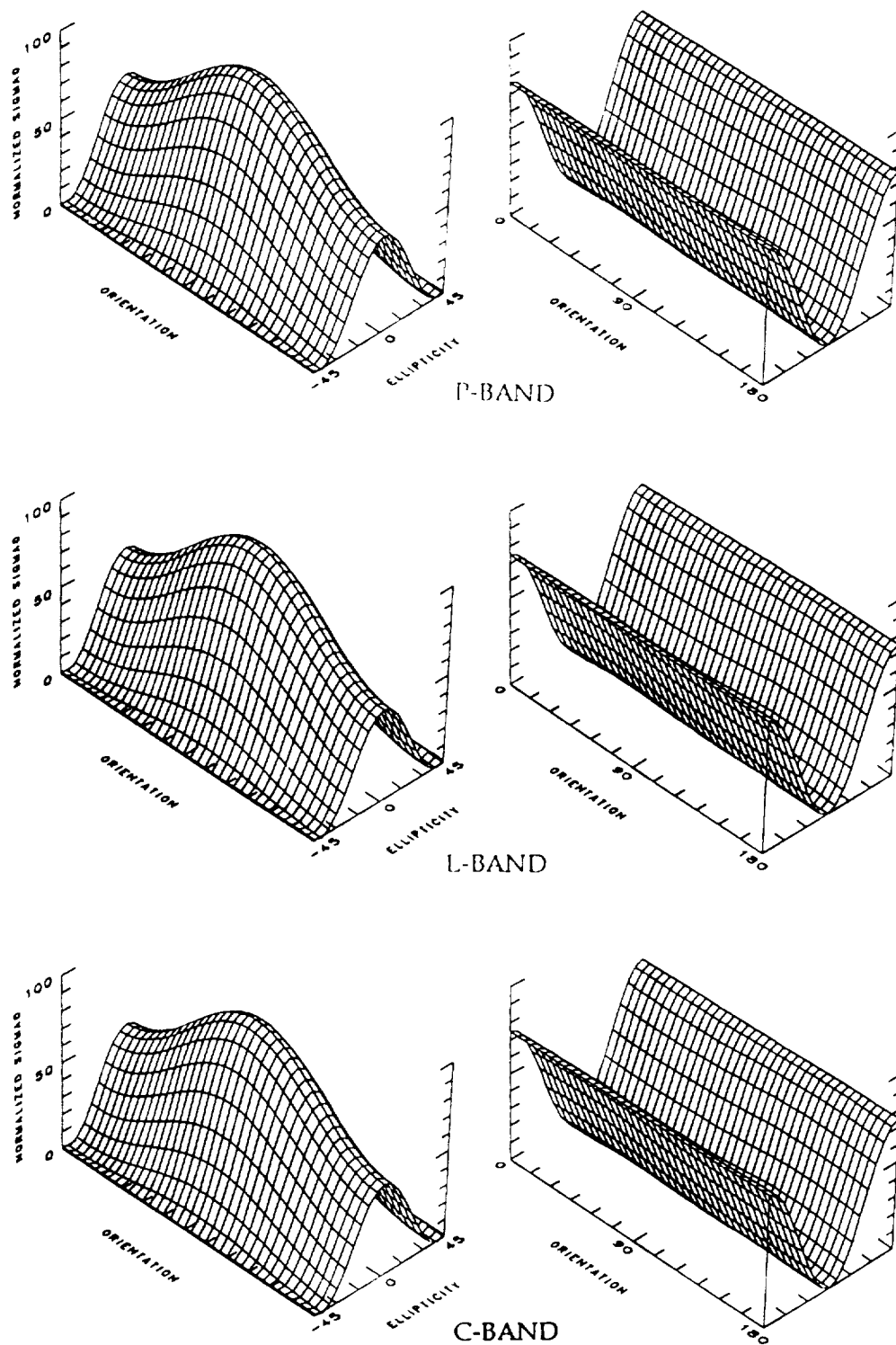
Figure 4-16   Physical optics model calculations, bare field, $\theta = 25°$, and $SM = 0.3 gm/cm^3$

PHYSICAL OPTICS MODEL CALCULATION
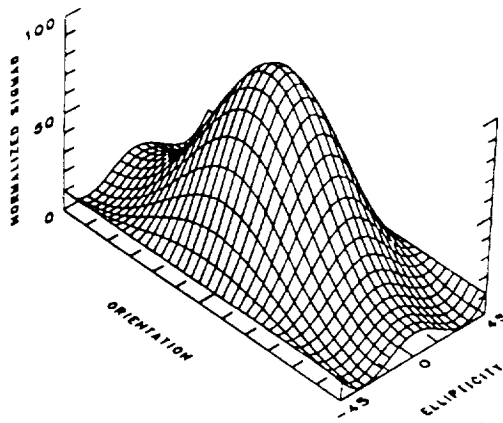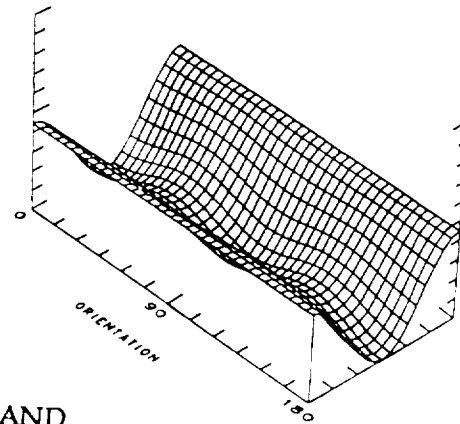## Soil Moisture = 0.3 gm/cm^3

COPOLARIZATION   CROSS-POLARIZATION

P-BAND

L-BAND

C-BAND
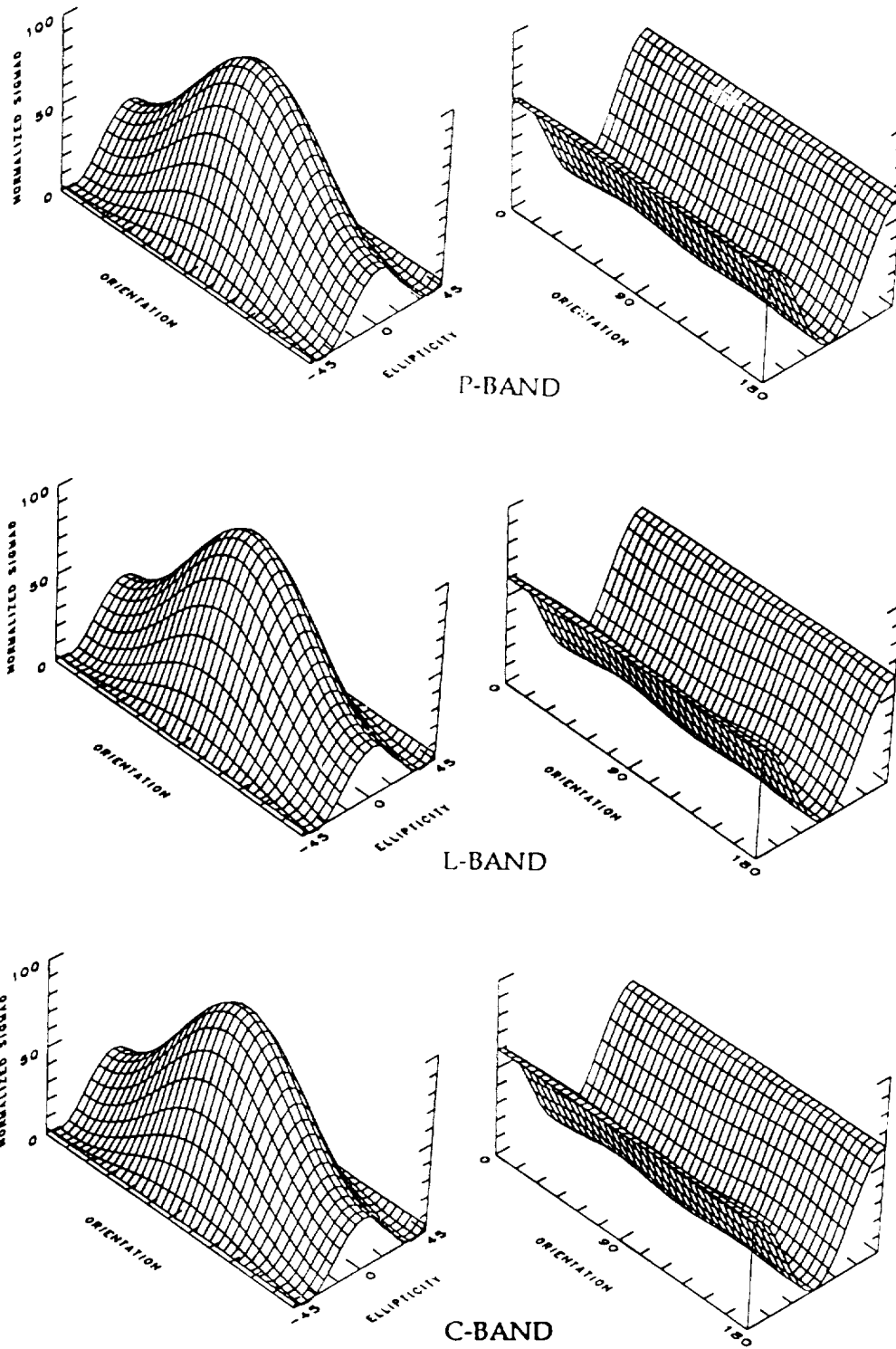
Figure 4-17   Physical optics model calculations, bare field, $\theta = 37°$, and $SM = 0.3 gm/cm^3$

PHYSICAL OPTICS MODEL CALCULATION
Soil Moisture = 0.3 gm/cm^3

COPOLARIZATION   CROSS-POLARIZATION
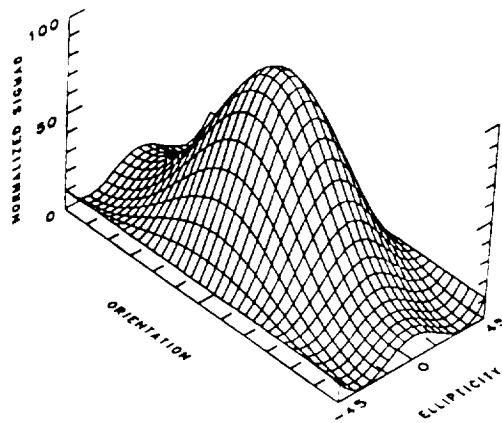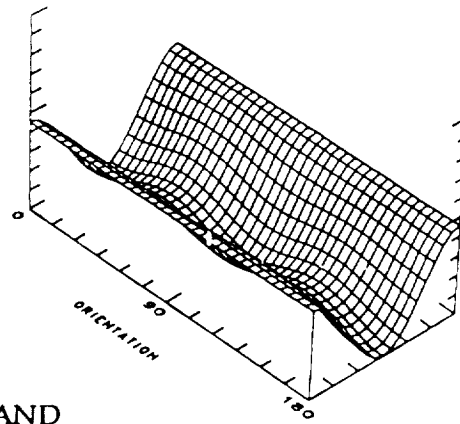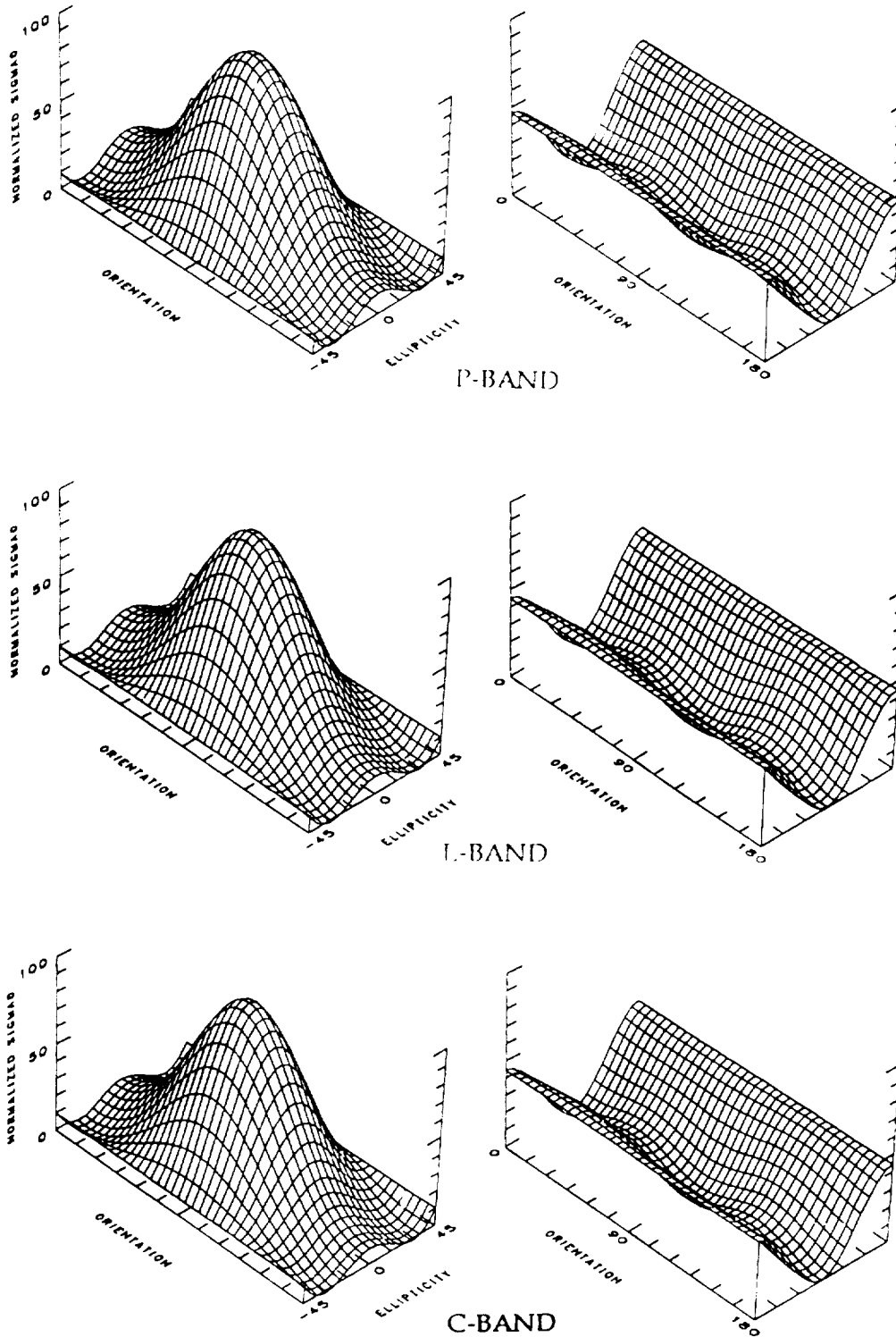
P-BAND

L-BAND

C-BAND

Figure 4-18   Physical optics model calculations, bare field, $\theta = 54°$, and $SM = 0.3 gm/cm^3$

PHYSICAL OPTICS MODEL CALCULATION
Soil Moisture = 0.4 gm/cm^3

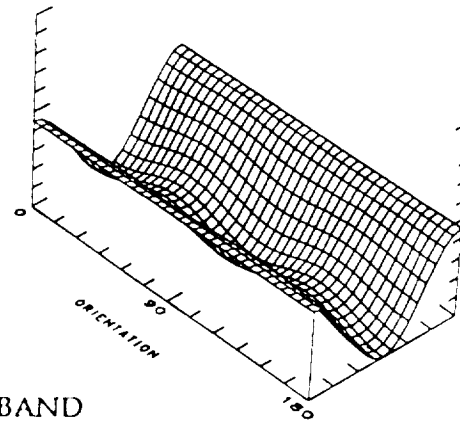COPOLARIZATION   CROSS-POLARIZATION
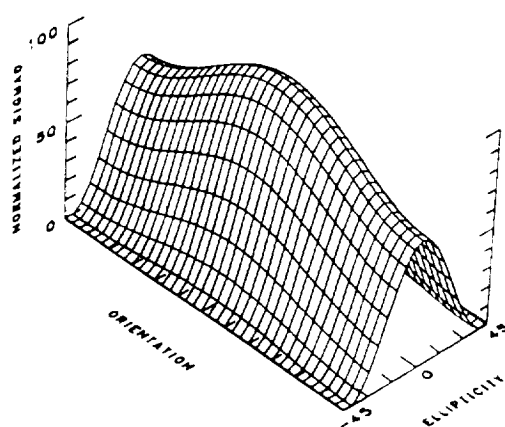
P-BAND
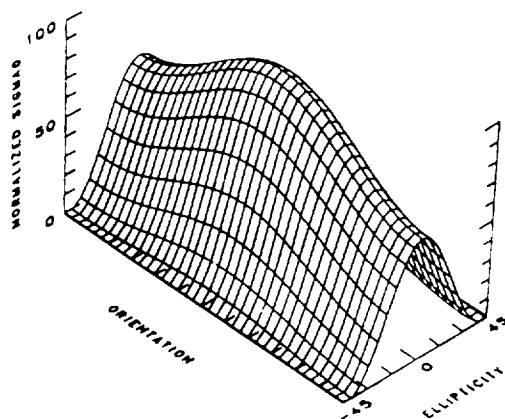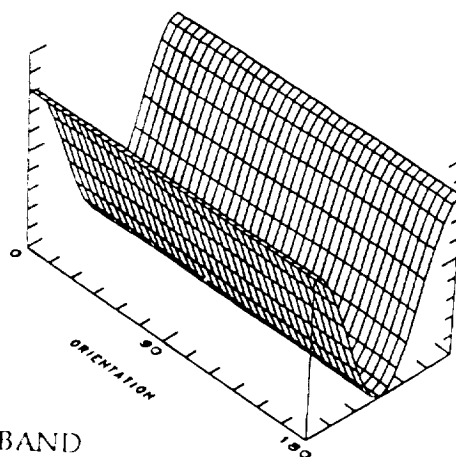
L-BAND
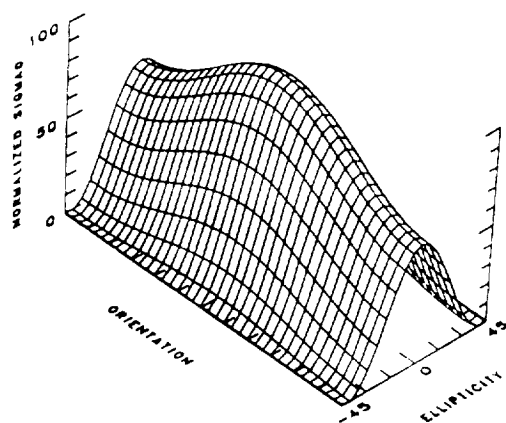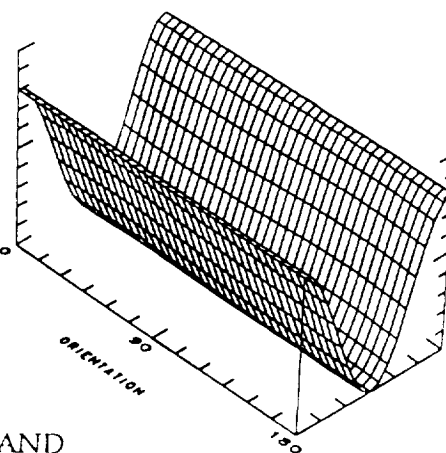
C-BAND
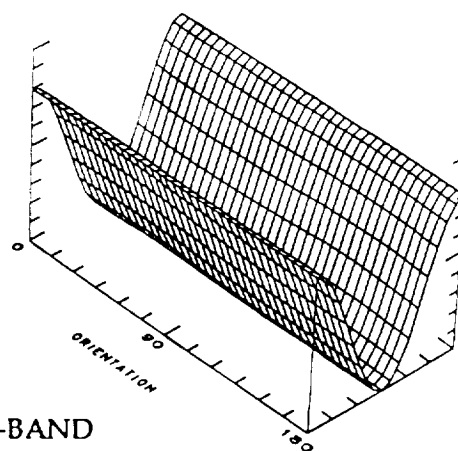
Figure 4-19   Physical optics model calculations, bare field, $\theta = 25°$, and $SM = 0.4 gm/cm^3$

PHYSICAL OPTICS MODEL CALCULATION
Soil Moisture = 0.4 gm/cm^3

COPOLARIZATION   CROSS-POLARIZATION
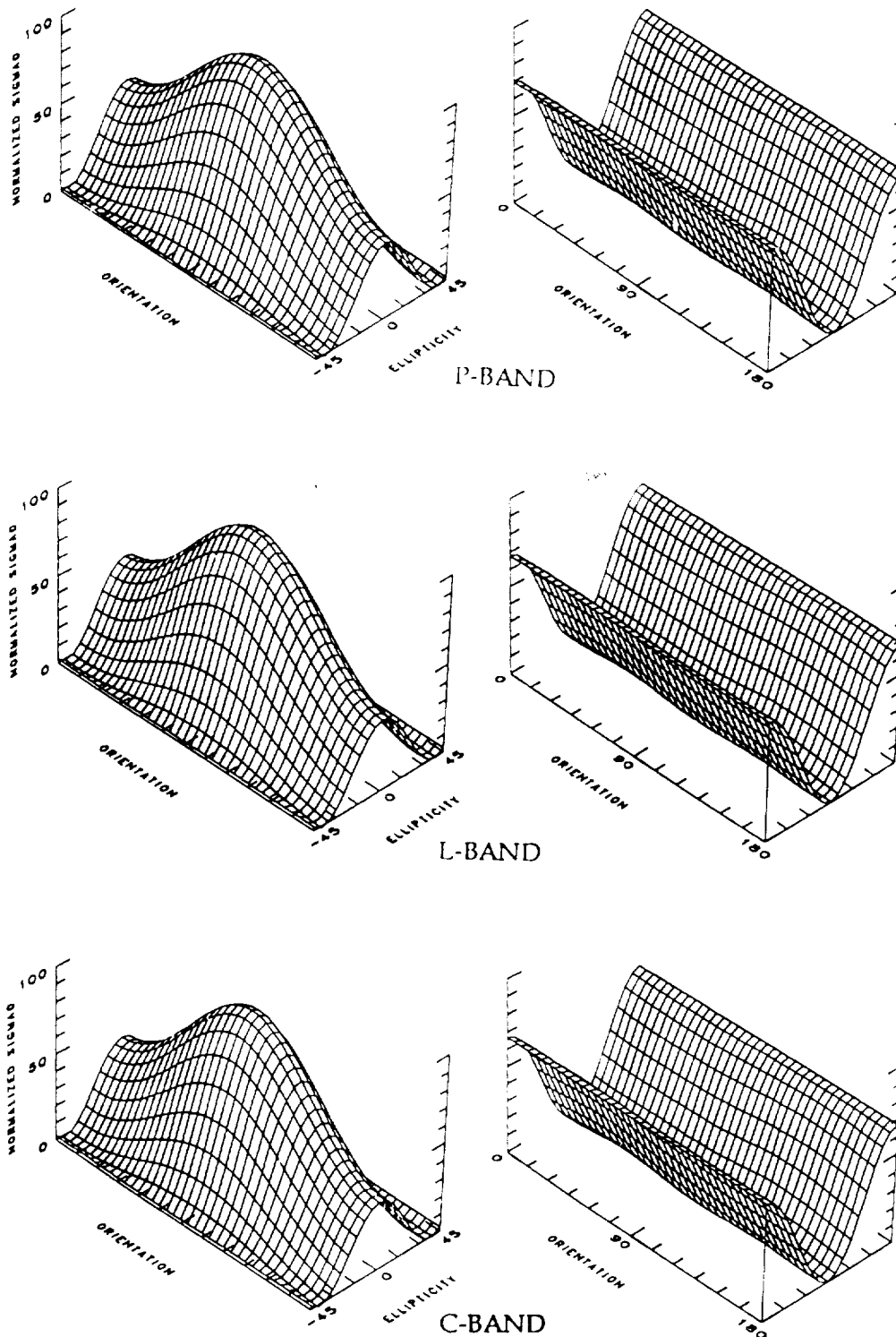
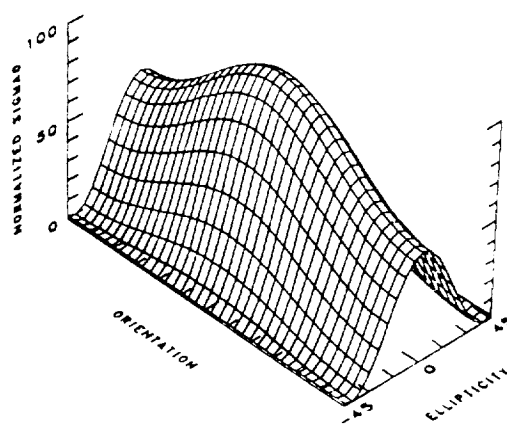P-BAND

L-BAND

C-BAND

Figure 4-20   Physical optics model calculations, bare field, $\theta = 37°$, and $SM = 0.4 gm/cm^3$

PHYSICAL OPTICS MODEL CALCULATION
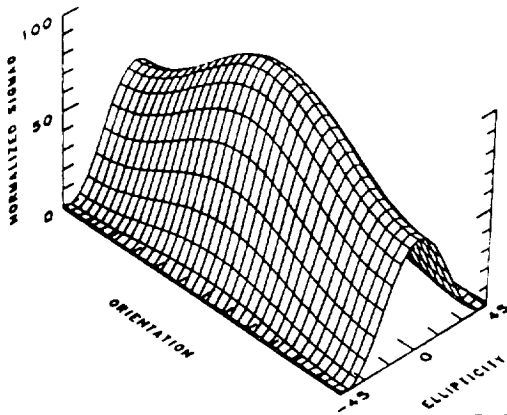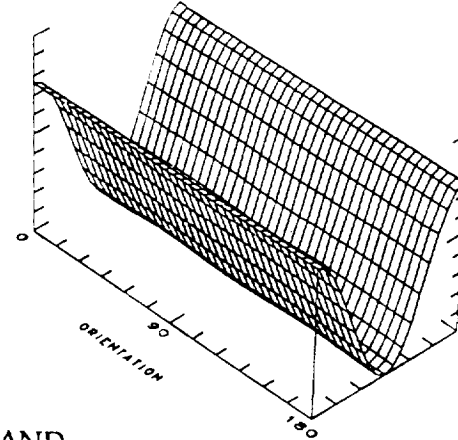## Soil Moisture = 0.4 gm/cm^3
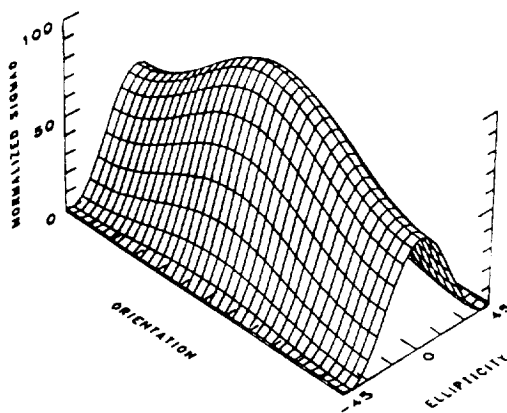
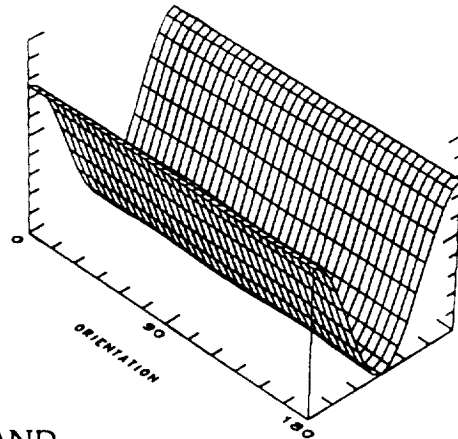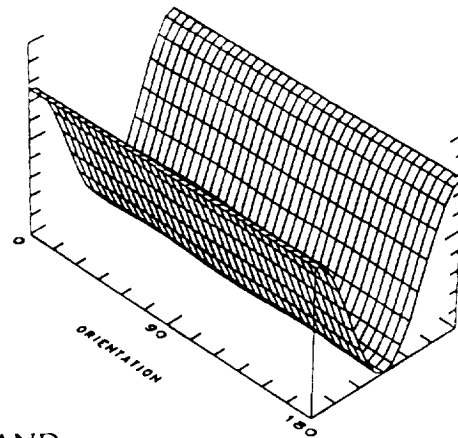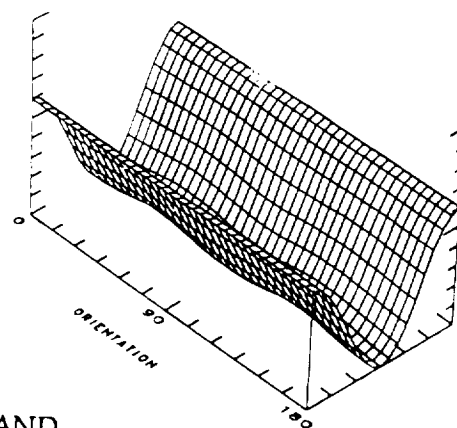COPOLARIZATION   CROSS-POLARIZATION
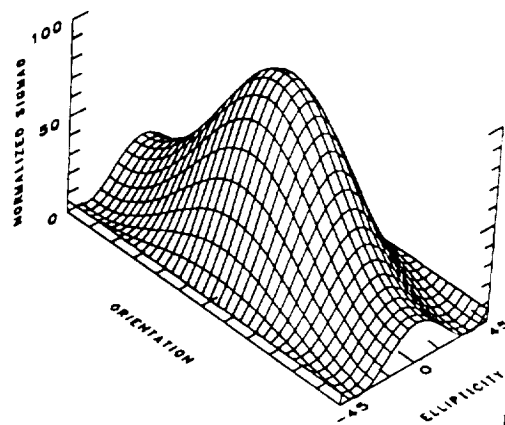
P-BAND
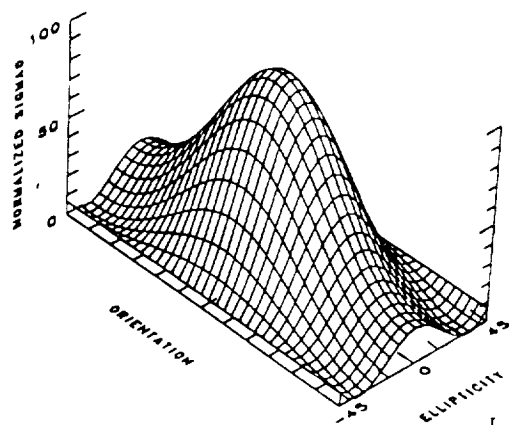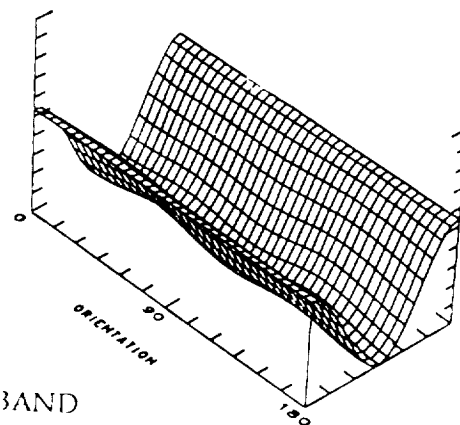
L-BAND
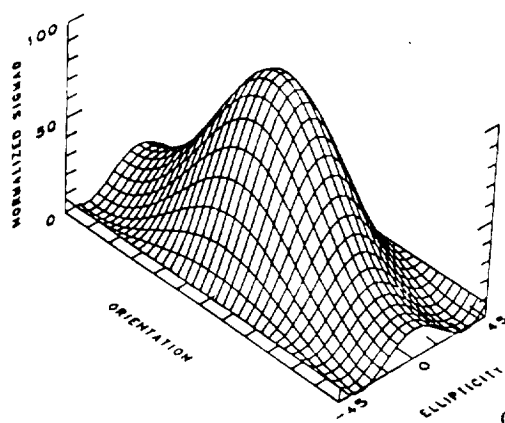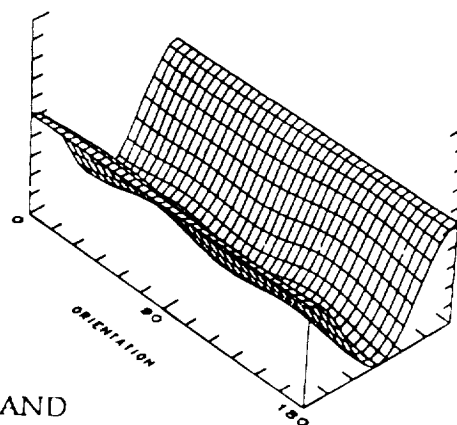
C-BAND
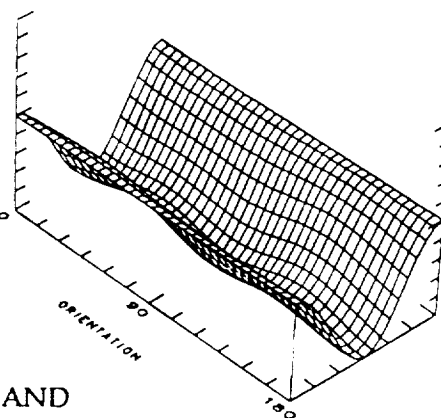
Figure 4-21 Physical optics model calculations, bare field, $\theta = 54°$, and $SM = 0.4gm/cm^3$

SECTION 5 - SCATTERING MATRIX OF A CYLINDER AND POLARIZATION SIGNATURES OF TREE-COVERED FIELDS

This section describes the scattering matrix of dielectric cylinders and polarization signatures of tree-covered fields. Figure 5-1 shows a sketch of the main scattering mechanisms which are taken into consideration for the calculations of radar scattering cross sections and the polarization signatures of tree-covered fields. The first one consists of two specular reflections, first from a vertical tree trunk or branch, and then from the ground surface. The outgoing reflected waves are also subject to forward scatterings. The second one is reflection from the non-vertical tree branches. A simple geometry shows that only those branches perpendicular to the direction of the incoming waves contribute to the SAR back-scattered signals. The derivation of the relevant formulas for this component is given in Appendix A. Both of these two scattering processes are subject to attenuation in passing through the canopy. Therefore, the third process is a propagation through the canopy, and it may also be considered as a forward scattering process.

The tree trunk and its branches are treated as dielectric cylinders of finite lengths. Also, we assume that the length L of the cylinder is much longer than the wavelength λ (i.e., $L \gg \lambda$), and that the cylindrical radius a satisfies the condition: $0.5 < ka < 10$ and $L \gg a$. Under these conditions, the scattered waves from the vertical cylinders of tree trunk and branches propagate only in the direction $\theta_s = \pi - \theta$. The scattering matrix $\mathbf{S}(\theta, \phi')$ of such cylinders of finite length L has been shown (References 21 and 29) for both the forward scattering case (where $\phi' = \pi$) and the specular scattering case (where $\phi' = 0°$) to be in the form

$$\mathbf{S}(\theta, \pi) = Q \begin{bmatrix} \sum_{n=-\infty}^{\infty} C_n^{TE} & 0 \\ 0 & \sum_{n=-\infty}^{\infty} C_n^{TM} \end{bmatrix} \qquad (5-1)$$

and

$$\mathbf{S}(\theta, 0°) = Q \begin{bmatrix} \sum_{n=-\infty}^{\infty} (-1)^n C_n^{TE} & 0 \\ 0 & \sum_{n=-\infty}^{\infty} (-1)^n C_n^{TM} \end{bmatrix} \qquad (5-2)$$

where Q is a factor due to finite length of the tree, and its value for the above two special cases is $Q = -\dfrac{iL}{\pi}$. The quantities C_n^{TE} and C_n^{TM} can be found in Reference 29 and are expressed in terms of the angle $(\pi/2 - \theta)$, cylinder radius a, and the complex dielectric constant ε_t of the cylinder for both the polarization TM (i.e., vertical) and TE (i.e., horizontal) waves.

We assume that the incoming waves interact only once with tree trunk or branches, which produce scatterings in the specular or forward direction. For the specular scattering case, the scattering matrix due to the two reflections can be represented by the product of two matrices $\rho S(\theta, 0°)$, and the Fresnel reflection coefficient matrix ρ for a rough surface is given by

$$\rho = \begin{bmatrix} \rho_h & 0 \\ 0 & \rho_v \end{bmatrix} e^{-2k^2 s^2 \cos^2\theta} \qquad (5-3)$$

where ρ_h and ρ_v are the Fresnel reflection coefficients of a smooth surface, and the subscripts h and v denote the horizontal and vertical polarizations, respectively. The exponential factor in Equation (5-3) takes into account the surface roughness, which is characterized by the rms surface height s and correlation length ℓ (References 30 and 31). The final outgoing scattered wave from the ground is subject to forward scattering, therefore the total 'effective' scattering matrix is given by

$$S_t(\theta) = S(\theta, \pi) \rho S(\theta, 0°) \qquad (5-4)$$

The scattering matrix in Equation (5-4) is then converted to Stokes matrix M_t for the trunk and vertical branches. The parameter s is fixed at s = 1 cm, which is the mean value of field measurements (Reference 23).

For the process of backscattering from a non-vertical branch which is in an arbitrary direction (θ_b, ϕ_b) with respect to the vertical tree-trunk direction, the scattering matrix can be written in the form (see Appendix A)

5-3

$$\mathbf{S}'(\theta, \theta_b) = Q \begin{bmatrix} \dfrac{\cos^2\theta_b}{\sin^2\theta} S_{hh} - \alpha S_{vv} & -\beta(S_{hh} + S_{vv}) \\[2ex] \beta(S_{hh} + S_{vv}) & -\alpha S_{hh} + \dfrac{\cos^2\theta_b}{\sin^2\theta} S_{vv} \end{bmatrix} \qquad (5-5)$$

where

$$\alpha = \sin^2\theta_b \sin^2\phi_b$$

$$\beta = \frac{\sin\theta_b \cos\theta_b \sin\phi_b}{\sin\theta} \qquad (5-6)$$

$$\sin\phi_b = \frac{\sqrt{-\cos(\theta + \theta_b)\cos(\theta - \theta_b)}}{\sin\theta \sin\theta_b}$$

The last formula in equation (5-6) specifies the condition for the occurrence of backscattering by non-vertical branches, and it requires $(\theta + \theta_b) \geq 90°$.

The quantities S_{hh} and S_{vv} are the same diagonal elements of scattering matrix for vertical cylinders as defined in Equation (5-2). The outgoing waves that are received by the antenna are the forward scattered parts, therefore the "total" scattering matrix for the backscattering process from non-vertical branches are given by

$$\mathbf{S}_b(\theta, \theta_b) = \mathbf{S}(\theta, \pi)\, \mathbf{S}'(\theta, \theta_b) \qquad (5-7)$$

where $\mathbf{S}(\theta, \pi)$ and $\mathbf{S}'(\theta, \theta_b)$ are defined in Equations (5-1) and (5-5), respectively.

Similarly, the total scattering matrix for process 3 in Figure 5-1 can be written as

$$\mathbf{S}_g(\theta) = \mathbf{S}(\theta, \pi)\, \mathbf{S}_s(\theta)\, \mathbf{S}(\theta, \pi) \qquad (5-8)$$

where $\mathbf{S}_s(\theta)$ is the scattering matrix of bare field surface. We chose the small perturbation model for which the scattering matrix is given by Equations (4-1) and (4-2). Equations (5-4), (5-7), and (5-8) define the scattering matrices corresponding to the three scattering mechanisms shown in Figure 5-1, respectively. These scattering matrices were converted into Stokes matrices, $\mathbf{M}_t$, $\mathbf{M}_b$, and $\mathbf{M}_g$,corresponding to trunk (and vertical branches), branches (non-vertical) , and ground, respectively. These Stokes matrices were used to simulate the observed polarization signatures of the tree-covered fields. Thus the total Stokes matrix $\mathbf{M}_{total}$ includes three terms

$$\mathbf{M}_{total} = <\mathbf{M}_t> + <\mathbf{M}_b> + <\mathbf{M}_g> \qquad (5-9)$$

where the notation $< \cdots >$ indicates that in applying Equation (5-9) for calculation of the polarization signature of the tree-covered fields, the Stokes matrix was averaged over the radius a and branch angle θ_b (in case of non-vertical branches are involved). Cylindrical radius a and length L of a tree and its branches are related by an empirical equation (Reference 3)

$$L = 116.28a - 0.30 \qquad (5-10)$$

5-5

where the radius a varies from 0.5 to 10 cm. The branch angle θ_b are in the range of $0° - 50°$. We assume that the branches distribute uniformly in both the radius a and angle θ_b.

Figure 5-2 show a comparison of the calculated and observed polarization signatures of a orchard tree field. The data shown in Figure 5-2a were obtained at a look angle $\theta = 25°$, while another one at $\theta = 43°$ is shown in Figure 5-3a , with its corresponding simulation given in Figure 5-3b. The observed polarization signatures shown in Figures 5-2 and 5-3 have large pedestals on bottom of both co- and cross-polarizations. This is due to a relatively high unpolarized return (perhaps caused by multiple scatterings) from the tree-covered fields. This unpolarized component of the polarization signatures can be taken into account, if the Stokes vectors in Equation (2-5) is written as a sum of two parts (Reference 26)

$$\mathbf{Y}^r = \begin{bmatrix} d \\ d\,cos2\psi_r \cos 2\chi_r \\ d\,sin2\psi_r \cos 2\chi_r \\ d\,\sin 2\chi_r \end{bmatrix} + \begin{bmatrix} 1 - d \\ 0 \\ 0 \\ 0 \end{bmatrix} \qquad (5-11)$$

where the first part in Equation (5-11) corresponds to the polarized component of the received signals from the tree-covered field, and the second part is the unpolarized component. The parameter d represents the degree of polarization purity, and its value was varied in the calculation of polarization signatures to best match the observed ones. It was found that

the d values in the range of 0.2 - 0.4 can produce reasonably good results for matching the observed polarization signature from the tree-covered fields. The calculations shown in Figures 5-2 and 5-3 were obtained with d = 0.25.

Figures 5-2 and 5-3 show that the simulated polarization signatures obtained with our cylindrical tree model are in reasonably good agreement with the observations, particularly at $\theta = 25°$. The simulated vertical polarization at $\theta = 43°$ (Figure 5-3) is smaller than observation. This is attributed to the fact that the vertically polarized Fresnel coefficient ρ_v is very small in comparison to the horizontally polarized ρ_h. For example, if the dielectric constant of the ground surface is assigned a numerical value of $\varepsilon = 5.0 + j\,0.5$, calculation gives $|\rho_v|^2 = 0.07$ and $|\rho_h|^2 = 0.24$ at $\theta = 43°$. This example shows that specular reflection from ground suppresses vertical polarization considerably at this large incidence angle. The relatively large vertical polarization observed in Figure 5-3 is most probably originated from some scattering mechanism, which is not involved with any specular ground reflection. The three scattering processes included in this study seem inadequate to account for this large contribution of vertical polarization. Further investigation in this area is required.
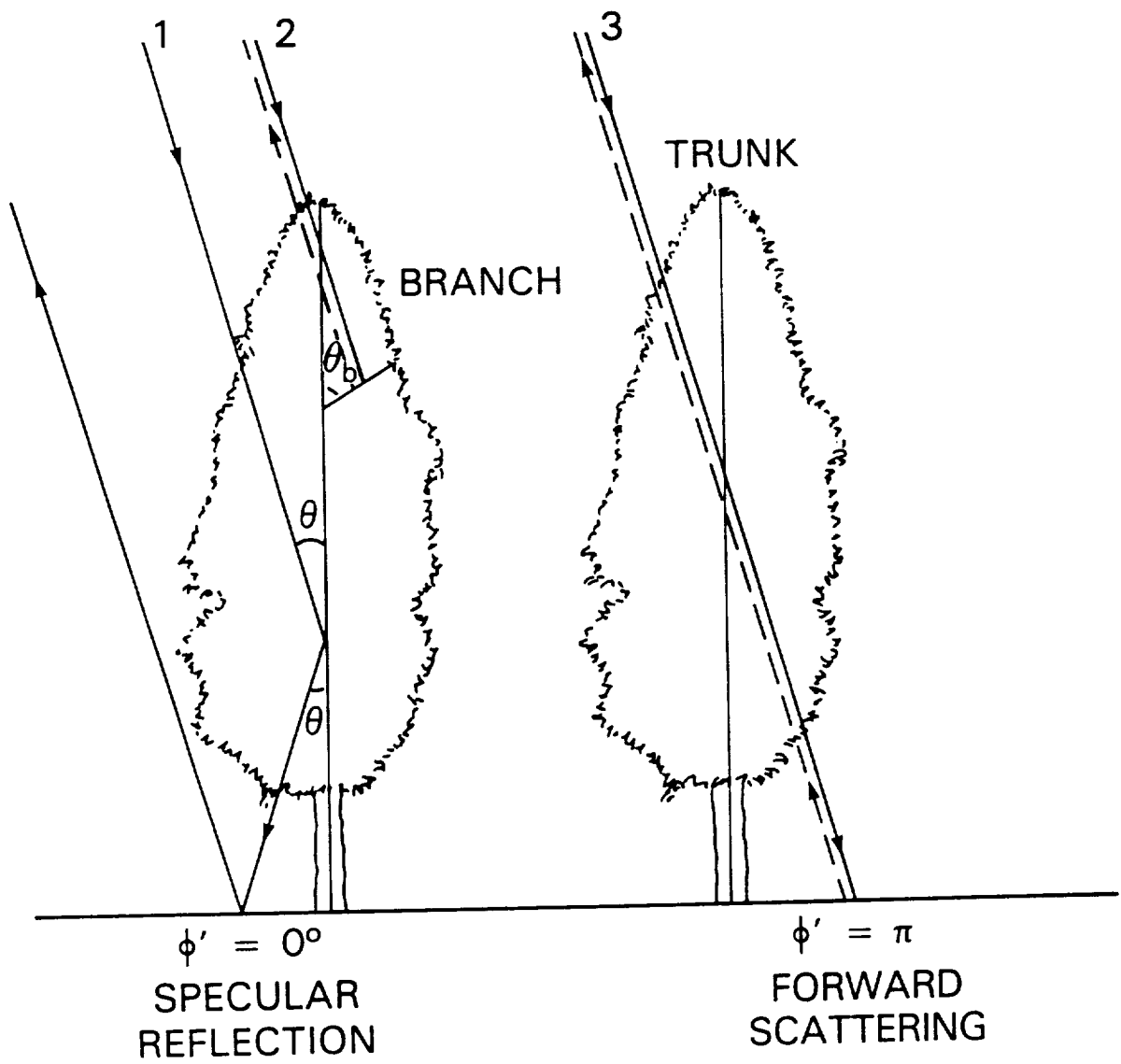
Figure 5-1   Sketch of tree scattering geometry.

CO-POLARIZATION   CROSS-POLARIZATION

(a) Observation at $\theta = 25°$
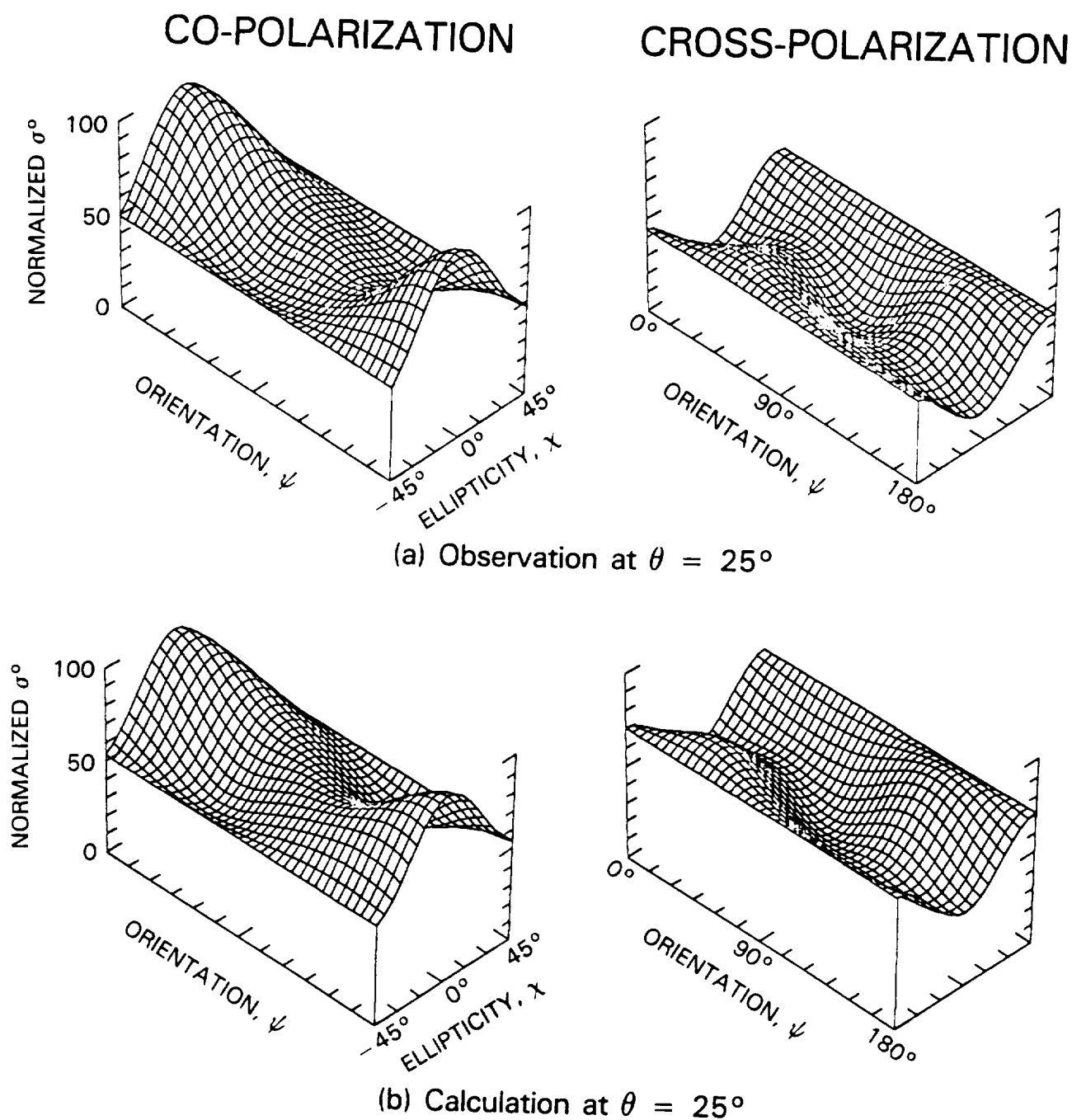
(b) Calculation at $\theta = 25°$

Figure 5-2   Comparison of observed and simulated polarization signatures from an orchard tree-covered field at $\theta = 25°$:(a) Observations, and (b) Simulations.

CO-POLARIZATION

CROSS-POLARIZATION
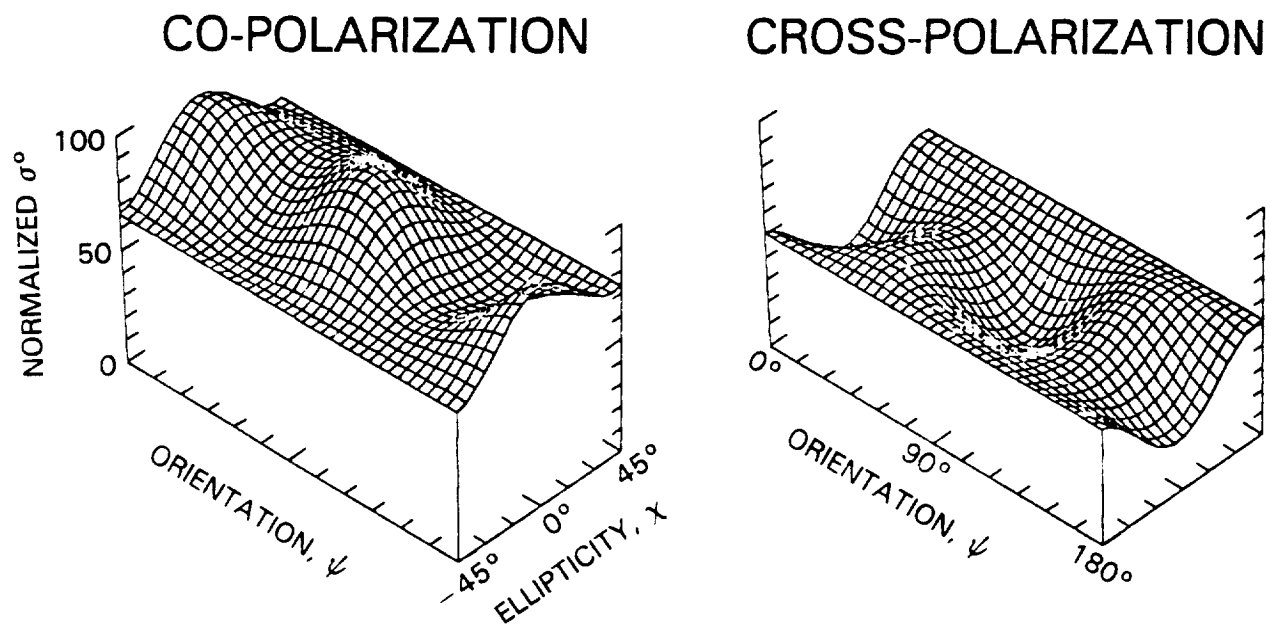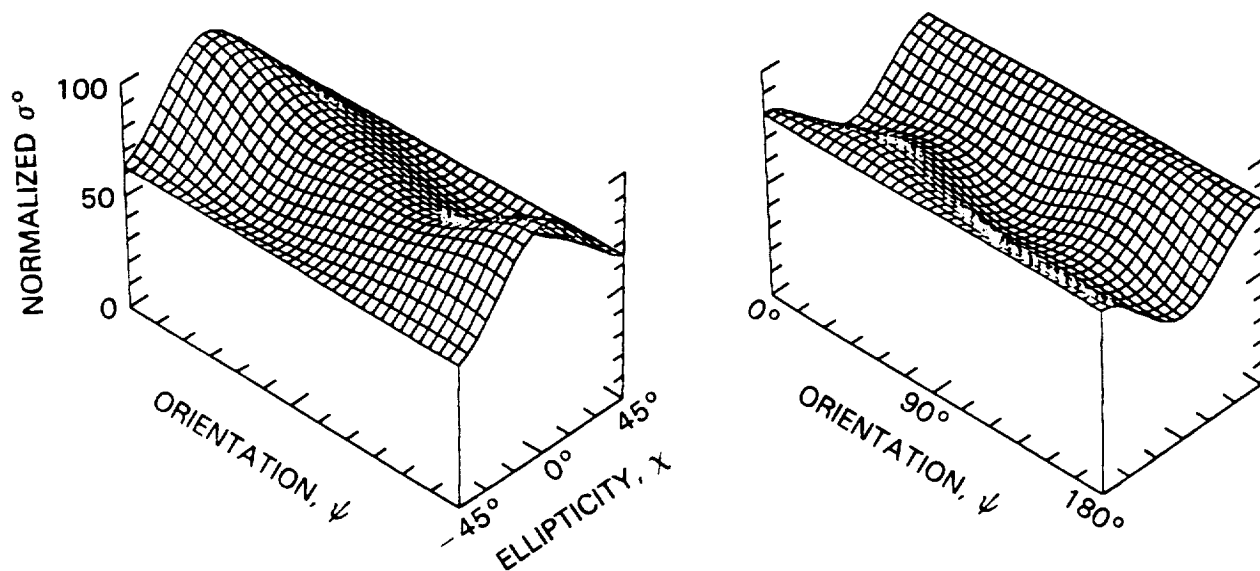
(a) Observation at $\theta = 43°$

(b) Calculation at $\theta = 43°$

Figure 5-3   Comparison of observed and simulated polarization signatures from an orchard tree-covered field at $\theta = 43°$:(a) Observations, and (b) Simulations.

SECTION 6 - POLARIZATION PHASE DIFFERENCE

Since the scattering matrices for all scattering mechanisms are already developed in Sections 2 and 5, it is relatively simple to obtain the formulas for the polarization phase difference (PPD) between the horizontal and vertical polarizations. By definition, the PPD (or $\Delta\Phi$) corresponding to a scattering matrix, [S], can be obtained from the product

$$S_{hh} S_{vv}^* = |S_{hh}| \ |S_{vv}| \ e^{i\Delta\Phi} \qquad (6-1)$$

where S_{hh} and S_{vv} are the diagonal elements of [S], and S_{vv}^* denotes the complex conjugate of S_{vv}. The quantity $\Delta\Phi$ is given by (References 4 and 19)

$$\Delta\Phi = \tan^{-1}\left[\frac{\mathrm{Im}\left\{\dfrac{S_{hh}}{S_{vv}}\right\}}{\mathrm{Re}\left\{\dfrac{S_{hh}}{S_{vv}}\right\}}\right] \qquad (6-2)$$

Substituting the two matrix elements in Equation (5-2) into Equation (6-2), one obtains the $\Delta\Phi_t$, corresponding to the specular reflection at the tree trunk or a vertical branch. Similarly, using the matrix elements in

Equations (5-3) and (5-5), we can obtain the $\Delta\Phi_g$ and $\Delta\Phi_b$, corresponding to the PPD for ground Fresnel reflection and backscattering from a non-vertical branch, respectively.

Additionally, there is also a PPD due to the propagation through the canopy. This PPD, $\Delta\Phi_{pt}$, due to propagation through the trunk or vertical branches, can be obtained from Equation (6-2) and the forward scattering matrix elements in Equation (5-1). Similarly, the $\Delta\Phi_{pb}$ due to propagation through non-vertical branches can be calculated by using the elements in Equation (A15). Therefore, the total PPD, $\Delta\Phi$, can be written as

$$
\begin{aligned}
\Delta\Phi &= <\Delta\Phi_t> + <\Delta\Phi_g> + <\Delta\Phi_{pt}>, \quad \text{for trunk and vertical branches} \\
&= <\Delta\Phi_b> + <\Delta\Phi_{pb}>, \quad \text{for non-vertical branches} \qquad (6\text{-}3)
\end{aligned}
$$

where the average $< \cdots >$ is performed over the radius a and also over the angle θ_b in the case of non-vertical branches.

The PPD data were obtained from the same tree-covered fields, which produced our polarization signatures. The PPD data provided by JPL were in the complex form $\mathbf{c} = \mathbf{a} + j\,\mathbf{b}$ stored on magnetic tape. We created the PPD image pixels corresponding to the quantity $\Delta\Phi = \arg(\mathbf{c})$ with a VAX computer and an image display system. Figure 6-1 shows one of such PPD image over the area of our investigation. The $\Delta\Phi$ values (also called pixel values) displayed in this image are in digital numbers (DN), ranging from 0 to 255, which represents an actual PPD interval of 2π. The PPD values can only be determined within module of 2π, and our PPD

image values were originally created in the range of $-\pi$ to π. Thus, those PPD values, which are larger than π, would become negative and appear in the low DN region. In practical applications, it is more convenient to work in the range of 0 to 2π. This can be accomplished by a simple conversion of adding 2π to the negative PPD values. To arrive at a correct representative PPD distribution, a part of the histogram is moved from the low DN region to the high DN region (where DN > 255) until a complete PPD distribution curve is obtained.

The dark areas in Figure 6-1 indicate low DN values and the bright spots represent high DN's. The tree-covered fields appear as white square or rectangular blocks in the image. The radar look angle θ is labeled on the right edge. The near-range part of the image corresponds to an incidence angle $\theta \cong 15°$ and the far range is $\theta \cong 55°$. Since the data were not absolutely calibrated, the PPD values obtained from arg(c) are arbitrary within an additive constant, which must be determined before one can make comparison with any theoretically predicted results.

For an azimuthally symmetric target, it is normally expected (Reference 4) that the backscattering characteristics are the same for both hh and vv polarizations at normal (or near normal) incidence. In this study, we assumed $\Delta\Phi = 0°$ for bare field targets at the near-range part (where $\theta \cong 15°$) within the image. In fact, it has been shown (Reference 4) that the assumption $\Delta\Phi(\theta) = 0°$, is valid, within experimental uncertainties, for all bare fields in the whole incidence angle range $\theta \cong 15° - 55°$. Figure

6-2 shows a PPD distribution versus the image digital number (DN) for a bare field at $\theta \cong 15°$. The mean value of these PPD values is 59.4, which is approximately the peak position of this distribution. This mean value from the bare field will be adopted as a zero-base reference and it will be denoted by $DN_0 = 59.4$, which corresponds to the absolute 0° in the $\Delta\Phi$ distribution from all targets in the image.

Figure 6-3 displays a PPD distribution versus DN for a tree-covered field at $\theta \cong 17°$. The PPD distribution in Figure 6-3 shows a series of small peaks across the whole range DN, in contrast to a smooth curve, as in the case of a bare field (Figure 6-2).

The mean DN value of the PPD distribution in Figure 6-3 is 297.5, which is approximately equal to the maximum peak position. One can convert this mean DN value into the average PPD value in degrees by the formula

$$\overline{\Delta\Phi}(\theta) = \frac{360°}{255} (\overline{DN} - 59.4) \qquad (6-4)$$

where the zero reference $DN_0 = 59.4$ and the conversion factor $r = 360°/255$, have been used. Similarly, the average PPD values $\overline{\Delta\Phi}(\theta)$ at other six θ's are obtained and these are shown in Figure 6-4 as open circles. One can see from this plot that the PPD values decrease gradually as θ increases from 20° to 45°. Our interest is to reproduce these data, using the model developed in this report.

The solid and dashed curves in Figure 6-4 represent calculated results with our model. The solid one is for the total PPD and the dashed one excludes the component due to propagation. The trunk radius a and tree density used in the calculations were estimated from field survey. The complex dielectric constant of tree trunk and branches (i.e., ε_t) is highly variable quantity. Field measurements indicated (Reference 32) that the diurnal change in this parameter can be up to an order of magnitude. We varied this parameter to obtain the results that would match the data, and found that a large range of ε_t (from $20 + j2$ to $40 + j4$) could all yield reasonably good results in matching the observed PPD data within experimental uncertainty.

-15°
-20°

$\Theta = 17^o$

$N = 567$

$\overline{DN} = 297.5$

$\overline{\triangle\Phi} = 335.3^o$

14

12

10

8

6

4

PERCENT OCCURRENCE

PHASE DIFFERENCE (DEGREES) vs **INCIDENCE ANGLE θ (DEGREES)**

TREE PARAMETERS:

a = 10 cm

N = 0.1 m^{-2}

ε = 28 + j2.8

O DATA
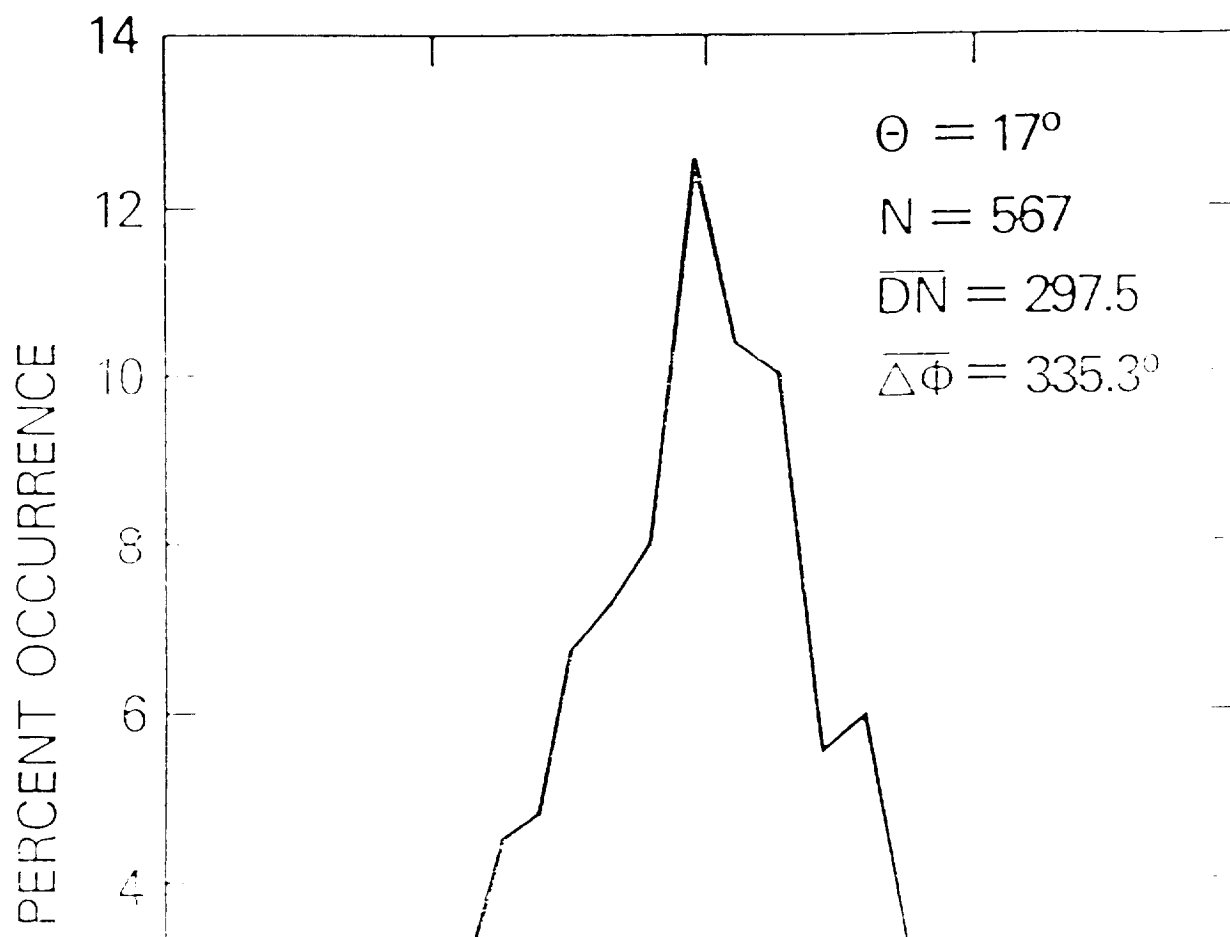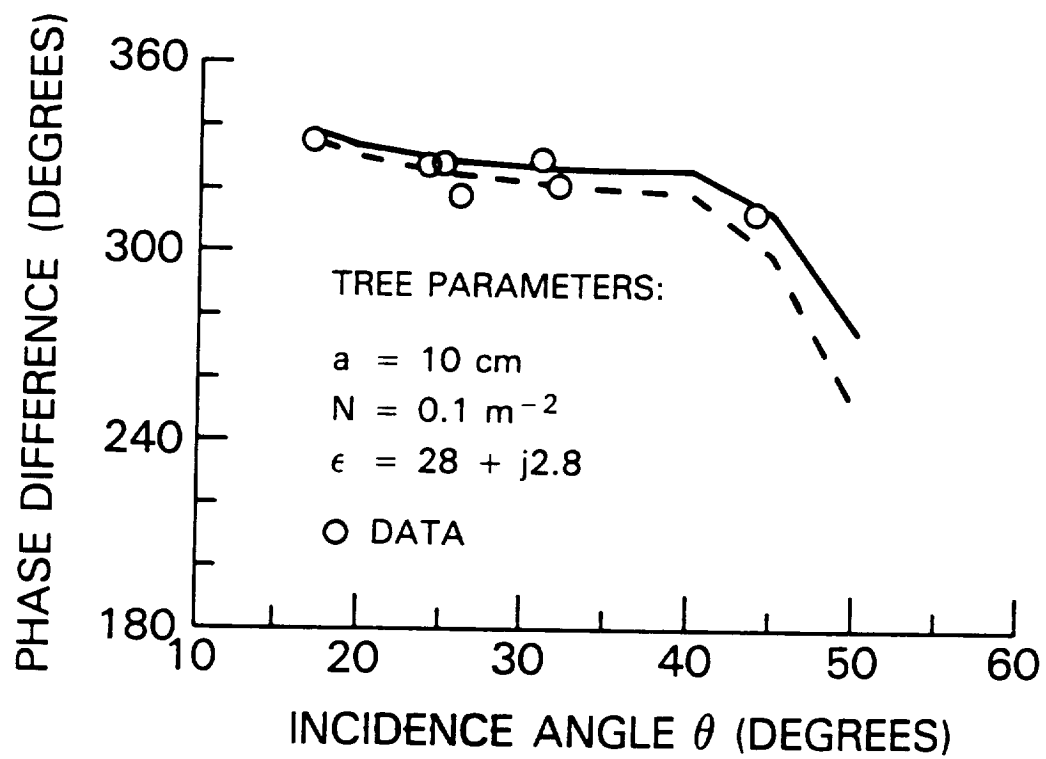
Figure 6-4   Comparison of the observed and simulated PPD.

SECTION 7 - THREE-LAYER EMISSIVITY MODEL

This section presents a model for passive remote sensing of a vegetation-covered soil surface. In this model, the microwave emission from the canopy and its underlying ground soil layers are detected by a radiometer. It is assumed that the vegetation or crop canopy forms a uniform layer covering the soil surface and that this canopy layer has a constant temperature T_c. The soils is divided into two layers (Figure 7-1). Each of the layers is assumed to have a constant temperature T_i (where i = 1 or 2) and dielectric constant ε, corresponding to its volumetric soil moisture SMV. The vegetation layer is characterized by a single scattering albedo ω and optical depth τ.

In a previous investigation (Reference 9), Mo et al., showed that the brightness $T_p(\theta)$ above the canopy for such a vegetation-covered field can be given by

$$
T_p(\theta) = T_p^s(\theta)e^{-\tau/\mu} + (1 - \omega)T_c(1 - e^{-\tau/\mu}) \\
+ R_1(1 - \omega)T_c(1 - e^{-\tau/\mu})e^{-\tau/\mu}
\tag{7 - 1}
$$

where $\mu = \cos\theta$, $T_p^s(\theta)$ is the brightness temperature of the underlying soil surface, and R_1 represent the reflectivity at the interface between the veg-

etation canopy and the top layer of soils. The subscript p ($=$h or v) in the formula is a polarization index. The quantity $T_p^{(s)}(\theta)$ represents the brightness temperature just above the canopy-soil interface. It consists of the upwards emissions from both layer 1 and layer 2 as shown in Figure 7-1. It was shown that $T_p^{(s)}(\theta)$ can be written in the form (Reference 10)

$$T_p^{(s)}(\theta) = e_{eff} \left[\left(1 + \frac{R_2}{L} \right) \left(1 - \frac{1}{L} \right) (1 - \omega_s) T_1 + \left(\frac{1 - R_2}{L} \right) T_2 \right] \quad (7 - 2)$$

with

$$e_{eff} = \frac{1 - R_1}{1 - \left(\dfrac{R_1 R_2}{L^2} \right)} \quad (7 - 3)$$

where ω_s is the single scattering albedo of the top soil layer and the L is the loss factor for layer 1. The e_{eff} is the effective emissivity of soil surface, including multiple scatterings at the top and bottom surfaces of layer 1.

Following previous investigations (Reference 10), the loss factor can be given by

$$L = \exp \left[\frac{\kappa_e d}{\cos \theta_1} \right] \quad (7 - 4)$$

where d is the thickness of the soil layer 1 and κ_e is the extinction coefficient of the soil layer. The extinction coefficient κ_e is related to the soil dielectric constant ε by (References 10 through 12)

$$\kappa_e = \frac{4\pi}{\lambda} \, |\, Im(\sqrt{\varepsilon}\,)\,|\qquad\qquad (7-5)$$

where λ is the wavelength in free space.

Using the formula in Equations (7-1) through (7-5), we calculate the brightness temperatures above the canopy as a function of volumetric soil moisture SMV1 in the top layer, while the soil moisture SMV2 in layer 2 is assumed constant. Figure 7-2 shows the calculated results (L-band and horizontal polarization at $\theta = 10°$), assuming three values for SMV2.

Results in Figure 7-2 show that the soil moisture in layer 2 affects the brightness temperature above the canopy if the top soil layer is dry and has SMV1 $< 0.15 \, gm/cm^3$, above which the effect of soil moisture in layer 2 vanishes. This is because of the fact that the penetration depth of the L-band emission decreases as the soil moisture increases and that its penetration depth is less than 5 cm (the thickness of layer 1) at SMV1 $= 0.15$ gm/cm^3. Figure 7-2 demonstrates that the calculated brightness temperatures with SMV2 $= 0.5$ and $0.25 \, gm/cm^3$ differ by 12K at SMV1 $= 0.05$ gm/cm^3, but only by 6K at SMV1 $= 0.10 \, gm/cm^3$. These results are in good agreement with recent field measurements (Reference 33).

CANOPY $\quad \theta \quad \omega, \tau, \ Tc$

SOIL
LAYER1 $\quad \theta_1 \quad \omega_s, \kappa_e, T_1, SM1$

SOIL
LAYER2 $\quad \omega_s \kappa_e, T_2, SM2$

d
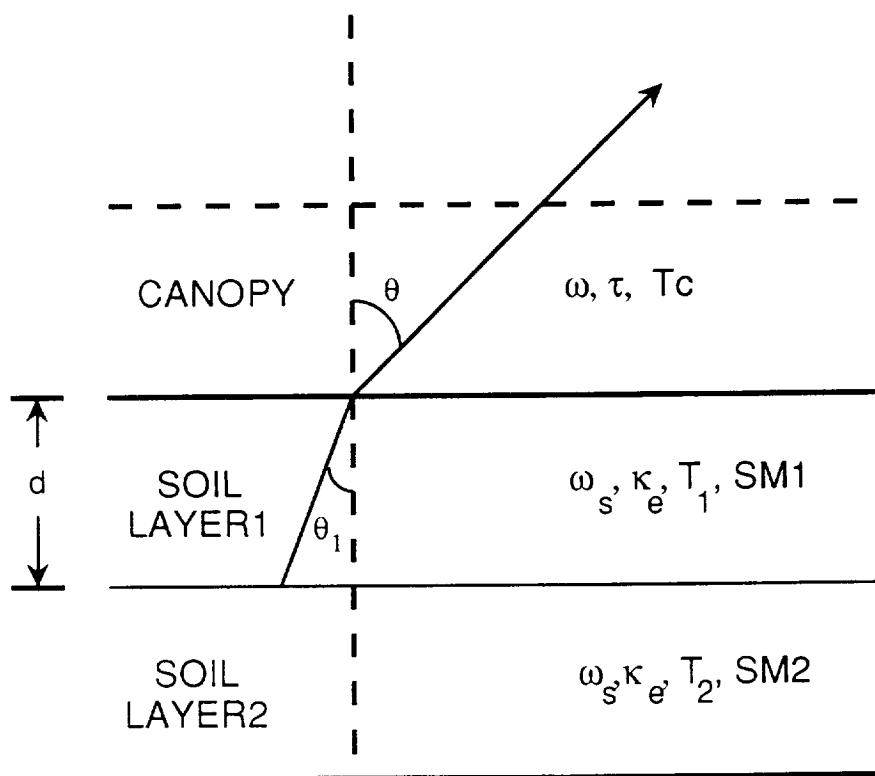
Figure 7-1   Geometry for Three-layer model.
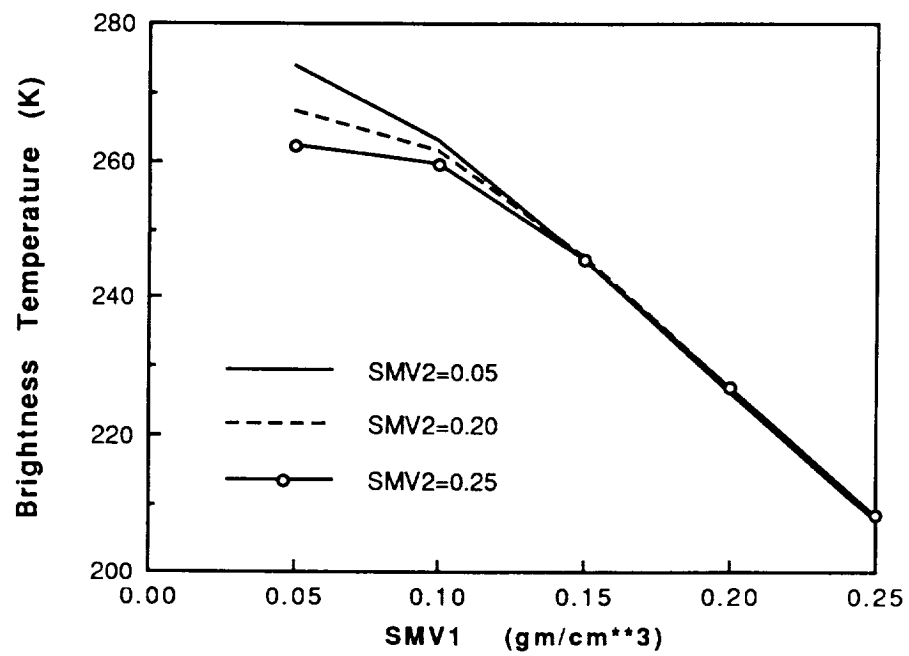
Figure 7-2   Calculated results from the three-layer model.

SECTION 8 - SUMMARY AND DISCUSSION

We have developed a series of electromagnetic wave scattering models for simulating the observed polarization signatures from both bare soil surfaces and tree-covered fields. The models are based on the electromagnetic wave scatterings from randomly rough surface and from dielectric cylinders, which replace the tree trunk and its branches. The tree branches are allowed to vary in size (both radius and length) and in direction relative to the vertical trunk direction.

Polarization phase differences of tree-covered fields are also investigated, and the theoretical results are compared with observed ones.

In addition, a model for passive remote sensing of vegetation-covered surface is developed. In this model, the microwave emission from the canopy and its underlying ground soil layers are detected by a radiometer. Two soil layers with individual temperatures and soil moisture contents are included in the model. The model results compare favorably with field measurements.

8-1

In simulation of observations from bare fields, we performed a series of calculations of the polarization signatures with three theoretical models for scattering from a randomly rough surface. The models used consist of the small perturbation model, the physical optics model and the geometrical optics model. The model calculations of polarization signatures were calculated at P-, L- and C-band frequencies, respectively. The calculated results were compared with observed polarization signatures acquired with the NASA/JPL airborne imaging radar polarimeter. The effects of surface roughness parameters and soil moisture contents on the polarization signatures were also studied.

It was found that the effects of parameters of surface roughness on the polarization signature are negligibly small. This is primarily due to the normalization process which eliminates the effects of surface roughness parameters on the backscattering coefficients. On the other hand, soil moisture has significant effect on the polarization signatures obtained from the small perturbation and physical optics models.

Calculations from both the small perturbation and physical optics models show strong dependence on the radar look angle θ. However, calculated polarization signature at fixed angle θ are insensitive to frequency variation.

Comparison of the calculated and observed polarizations signatures from bare fields at $\theta = 25°$, $\theta = 37°$ and $\theta = 54°$, respectively, shows good agreement, especially for the results at P-band.

Polarization signatures obtained with the geometrical optics model are independent of frequency, radar look angle, surface roughness parameters and soil moisture contents.

In simulation of observations from tree-covered fields, the main scattering mechanisms taken into consideration in the model are: (1) Specular reflection from the vertical tree trunk or branch, followed by another reflection from the ground surface (also specularly), (2) backscattering from non-vertical branches, and (3) propagation through the canopy, as represented by the forward scattering.

The simulated results for both polarization signatures and polarization phase differences are in reasonably good agreement with observations. The model can indicate which scattering mechanism is dominant in interpretation of the observed polarization signatures and polarization phase differences. Parameters of tree and surface properties may also be extracted by best matching the simulated and observed results.

The results presented in this studies should be useful for the polarimetric investigation of interaction between the vegetation and the underlying scattering surface which is ubiquitously involved in the scattering process.

REFERENCES

1. J. R. Wang, E. T. Engman, T. Mo, T. J. Schmugge, and J. C. Shuie, "The Effects of Soil Moisture, Surface Roughness, and Vegetation on L-Band Emission and Backscatter, " IEEE Trans. Geosci. Remote Sensing, GE-25, pp. 825-833, 1987.

2. M. W. Whitt and F. T. Ulaby, "Millimeter-Wave Polarimetric Measurements of Artificial and Natural Targets," IEEE Trans. Geosci. Remote Sensing, vol.26, pp. 562-573, 1988.

3. J. A. Richards, G. Q. Sun, and D. S. Simonett, "L-band Radar Backscatter Modeling of Forest Stands, " IEEE Trans. Geosci. Remote Sensing, GE-25, pp. 487-498, 1987.

4. F. T. Ulaby, D. Held, M. C. Dobson, K. C. McDonald, and T. B. A. Senior, "Relating Polarization Phase Difference of SAR Signals to Scene Properties," IEEE Trans. Geosci. Remote Sensing, GE-25, pp.83-92, 1987.

5. T. Le Tuan and H. Laur, "Multi-temporal and Dual Polarization Observations of Agricultural Crops by X-band SAR Images," 1988 International Geoscience and Remote Sensing Symposium, vol. 3, pp. 1291-1294, September 12-16, 1988, Edinburgh, U K

6. T. Mo, T. J. Schmugge, and J. R. Wang, "Calculations of microwave brightness temperature of rough soil surfaces: Bare field," NASA Goddard Space Flight Center, Greenbelt, MD, Tech. Memo. 86200; also, IEEE Trans, Geosci. Remote Sensing, vol. GE-25, pp. 47-54, 1987.

7. T. Mo and T. J. Schmugge, "A Parameterization of the Effect of Surface Roughness on Microwave Emission," IEEE Trans. Geosci. Remote Sensing, GE-25, pp. 481-485, 1987.

8. T. Mo, J. R. Wang, and T. J. Schmugge, "Estimation of Surface Roughness Parameters from Dual-Frequency Measurements of Radar Backscattering Coefficients," IEEE Trans. Geosci. Remote Sensing, Vol. 26, pp. 574-579, 1988.

9. T. Mo, B. J. Choudhury, T.J. Schmugge, J. R. Wang, and T. J. Jackson, "A model for microwave emission from vegetation-covered fields," J. Geophys. Res., vol. 87, pp. 11229-11237, 1982.

10. F. T. Ulaby, R. K. Moore, and A. K. Fung, Microwave Remote Sensing: Active and Passive , Vol. 1, Addison-Wesley Publishing Company, Reading, Massachusetts, 1981.

11. F. T. Ulaby, R. K. Moore, and A. K. Fung, Microwave Remote Sensing: Active and Passive , Vol. 2, Addison-Wesley Publishing Company, Reading, Massachusetts, 1982.

12. F. T. Ulaby, R. K. Moore, and A. K. Fung, Microwave Remote Sensing: Active and Passive , Vol. 3, Artech House, Dedham, MA, 1986.

13. D. L. Evans, T. G. Farr, J. J. van Zyl, and H. A. Zebker, "Radar Polarimetry: Analysis Tools and Applications," IEEE Trans. Geosci. Remote Sensing, vol. 26, pp. 774-789, 1988.

14. C. Elachi, W. E. Brown, J. B. Cimino, T. Dixon, D. L. Evans, J. P. Ford, R. S. Saunders, C. Breed, H. Masursky, J. F. McCauley, G. Schaber, L. Dellwid, A. England, H. MacDonald, P. Martin-Kaye, and F. Sabins, "Shuttle Imaging Radar Experiment," Science, 218, pp. 996-1003, 1982.

15. J. F. McCauley, G. G. Schaber, C. S. Breed, M. J. Grolier, C. V. Haynes, B. Issawi, C. Elachi, and R. Blom, "Subsurface Valleys and Geoarcheology of the Eastern Sahara Revealed by Shuttle Radar," Science, 218, pp. 1004-1020, 1982.

16. L. Tsang, J. A. Kong, and R. T. Shin, Theory of Microwave Remote Sensing , John Willy, New York, 1985.

17. J. J. van Zyl, H. A. Zebker, and C. Elachi, "Imaging Radar Polarization Signature: Theory and Observation," Radio Science, vol 22, pp. 529-543, 1987.

18. H. A. Zebker, J. J. van Zyl, and D. N. Held, "Imaging Radar Polarimetry from Wave Synthesis," J. Geophys. Res., vol. 92, NO. B1, pp. 683-701, 1987.

19. T. Mo and J. R. Wang, "A Study of SAR Polarization Signature and Phase Difference of Orchard Trees", IEEE Trans. Geosci. Remote Sensing, 1989, Submitted for publication.

20. T. Mo and J. R. Wang, "Modelling of SAR Polarization Phase Difference from Trees," 1988 International Geoscience and Remote Sensing Symposium, vol. 1, pp. 55-58, September 12-16, 1988, Edinburgh, U K.

21. F. T. Ulaby, K. Sarabandi, K. McDonald, M. Whitt, and M. C. Dobson, "Michigan Microwave Canopy Scattering Model (MIMICS)," Report 022486-T-1, July 1988, Department of Electrical Engineering & Computer Science, Uiversity of Michigan, Ann Arbor, Michigan

22. H. C. van de Hulst, Light Scattering by Small Particles , Dover Publications, Inc., New York, 1981.

23. J. R. Wang, E. T. Engman, J. C. Shiue, M. Rusek, and C. Steinmeier, "The SIR-B observations of microwave backscatter dependence on soil moisture, surface roughness, and vegetation covers," IEEE Transaction on Geoscience and Remote Sensing, GE-24(4), pp. 510-516, 1986.

24. H. A. Zebker and Y. Lou, "Phase Calibration of Imaging Radar Polarimeter Stokes Matrix," 1989 International Geoscience and Remote Sensing Symposium, pp. 2881-2884, July 10-14, 1989, Vancouver, Canada.

25. L. Norikane and F. Burnette, "Multiview Guide," Technical Report, August 1987, Jet Propulsion Laboratory, Pasadena, CA 91109

26. J. D. Kraus, Radio Astronomy , New York: McGraw Hill, 1966.

27. A. Ishimaru, Wave Propagation and Scattering in Random Media , p.480-481, Academic Press, New York, 1978.

28. M. T. Hallikainen, F. T. Ulaby, M. C. Dobson, M. A. El-Rayes, and L.-K. Wu, "Microwave Dielectric Behavior of Wet Soil - Part I: Empirical Models and Experimental Observations," IEEE Trans. Geosci. Remote Sensing, Vol. GE-23, pp. 25-34, 1985.

29. G. T. Ruck, D. E. Barrick, W. D. Stuart, and C. K. Krichbaum, Radar Cross-Section Handbook (see Section 4.2, pp. 266-274) , New York, Plenum, 1970.

30. T. Mo and T. J Schmugge, "A Parameterization of the Effect of Surface Roughness on Microwave Emission," IEEE Trans. Geosci. Remote Sensing, GE-25, pp. 481-485, 1987.

31. B. J. Choudhury, T. J. Schmugge, R. W. Newton, and A. Chang, "Effect of Surface Roughness on the Microwave Emission from Soils," J. Geophys. Res., vol. 13, pp. 329-344, 1983.

32. M. C. Dobson, "Diurnal and Seasonal Variations in the Microwave Dielectric Constant of Selected Trees," 1988 International Geoscience and Remote Sensing Symposium, vol 3, p. 1754, September 12-16, 1988, Edinburgh, U K

33. J. R. Wang, private communication, 1989.

34. F. Varosi, private communication, 1989.

APPENDIX A - STOKES MATRIX

The matrices, which appear Sections 2, 5 and 6, are defined in this Appendix. Since detailed derivations of these matrices can be found elsewhere (References 17 and 21) or in textbooks (Reference 16), only a brief description and the defining equations are given here.

If a radar wave traveling in the $\hat{k}$ direction, its electric field $\mathbf{E}$ is given by

$$\mathbf{E} = (E_h\hat{h} + E_v\hat{v})\, e^{-i(\omega t - \mathbf{k} \cdot \mathbf{r})} \qquad (A1)$$

where E_h and E_v represent the components of horizontal and vertical polarizations along the directions of the unit vectors $\hat{h}$ and $\hat{v}$, respectively. The Stokes vector $\mathbf{F}$, which represents the polarization state of the wave, is given by

$$\mathbf{F} = \begin{bmatrix} |E_h|^2 + |E_v|^2 \\ |E_h|^2 - |E_v|^2 \\ 2\text{Re}(E_h E_v^*) \\ 2\text{Im}(E_h E_v^*) \end{bmatrix} = S_o \begin{bmatrix} 1 \\ \cos 2\psi \cos 2\chi \\ \sin 2\psi \cos 2\chi \\ \sin 2\chi \end{bmatrix} \qquad (A2)$$

A-1

where $S_o = |E_h|^2 + |E_v|^2$ is the average total power carried by the wave. The Stokes matrix [M] is defined as

$$\mathbf{M} = \mathbf{\tilde{R}}^{-1} \, \mathbf{W} \, \mathbf{R}^{-1} \qquad (A4)$$

where

$$\mathbf{W} = \begin{bmatrix} S_{hh}S_{hh}^* & S_{hv}S_{hv}^* & S_{hh}S_{hv}^* & S_{hv}S_{hh}^* \\ S_{vh}S_{vh}^* & S_{vv}S_{vv}^* & S_{vh}S_{vv}^* & S_{vv}S_{vh}^* \\ S_{hh}S_{vh}^* & S_{hv}S_{vv}^* & S_{hh}S_{vv}^* & S_{hv}S_{vh}^* \\ S_{vh}S_{hh}^* & S_{vv}S_{hv}^* & S_{vh}S_{hv}^* & S_{vv}S_{hh}^* \end{bmatrix} \qquad (A5)$$

and

$$\mathbf{R} = \begin{bmatrix} 1 & 1 & 0 & 0 \\ 1 & -1 & 0 & 0 \\ 0 & 0 & 1 & 1 \\ 0 & 0 & -i & i \end{bmatrix} \qquad (A6)$$

Scattering Matrix from a Non-vertical Branch

Simple geometry shows that only normally incident waves on non-vertical branches can be backscattered and received by an airborne antenna. Thus, we only derive the scattering matrix for normally incident waves on the non-vertical branches.

In general, a branch is along the $\hat{z}_b$-direction, which makes angles (θ_b, ϕ_b) with respect to the coordinate system $(\hat{x}, \hat{y}, \hat{z})$, with the $\hat{z}$-direction along

the vertical tree trunk. We assume a corresponding coordinate system, $(\hat{x}_b, \hat{y}_b, \hat{z}_b)$ to represent the unit coordinates local to the cylindrical branch (Figure A1). It can be shown that

$$
\begin{aligned}
\hat{x}_b &= \cos \theta_b \cos \phi_b \, \hat{x} + \cos \theta_b \sin \phi_b \, \hat{y} - \sin \theta_b \, \hat{z} \\
\hat{y}_b &= - \sin \phi_b \, \hat{x} + \cos \phi_b \, \hat{y} \\
\hat{z}_b &= \sin \theta_b \cos \phi_b \, \hat{x} + \sin \theta_b \sin \phi_b \, \hat{y} + \cos \theta_b \, \hat{z}
\end{aligned}
\tag{A7}
$$

We assume that the incidence wave is in the x-y plane and travels in the direction

$$
\hat{k}_i = - \sin \theta \, \hat{x} - \cos \theta \, \hat{z}
\tag{A8}
$$

where θ is the angle between $\hat{k}_i$ and the $\hat{z}$-axis. For normal incidence waves, we have

$$
\hat{k}_i \cdot \hat{z}_b = 0 = - \sin \theta \sin \theta_b \cos \phi_b - \cos \theta \cos \theta_b
\tag{A9}
$$

Therefore

$$
\cos \phi_b = - \cot \theta \cot \theta_b
\tag{A10}
$$

Equation (A10) specifies the condition for the waves normally incident on non-vertical branches.

It has been shown (Reference 21) that the scattering matrix for such an arbitrarily oriented cylindrical branch can be given by

A-3

$$S'(\theta, \theta_b, \phi') = Q \begin{bmatrix} (\hat{\mathbf{h}}_s^b \cdot \hat{\mathbf{h}}_s) & (\hat{\mathbf{v}}_s^b \cdot \hat{\mathbf{h}}_s) \\ (\hat{\mathbf{h}}_s^b \cdot \hat{\mathbf{v}}_s) & (\hat{\mathbf{v}}_s^b \cdot \hat{\mathbf{v}}_s) \end{bmatrix} \begin{bmatrix} S_{hh} & S_{hv} \\ S_{vh} & S_{vv} \end{bmatrix} \begin{bmatrix} (\hat{\mathbf{h}}_i \cdot \hat{\mathbf{h}}_i^b)) & (\hat{\mathbf{v}}_i \cdot \hat{\mathbf{h}}_i^b) \\ (\hat{\mathbf{h}}_i \cdot \hat{\mathbf{v}}_i^b) & (\hat{\mathbf{v}}_i \cdot \hat{\mathbf{v}}_i^b) \end{bmatrix} \qquad (A11)$$

where $S_{hv} = S_{vh} = 0$ for normal incidence waves, and

$$\begin{aligned} S_{hh} &= \sum_{n=-\infty}^{\infty} (-1)^n C_n^{TE}(\theta)\, e^{in\phi'} \\ S_{vv} &= \sum_{n=-\infty}^{\infty} (-1)^n C_n^{TM}(\theta)\, e^{in\phi'} \end{aligned} \qquad (A12)$$

where $\phi' = 0°$ for backscattering, and $\phi' = \pi$ for forward scattering. The polarization vectors $(\hat{\mathbf{h}}_i, \hat{\mathbf{v}}_i)$ for incidence waves and $(\hat{\mathbf{h}}_s, \hat{\mathbf{v}}_s)$ for scattered waves, refer to the $(\hat{\mathbf{x}}, \hat{\mathbf{y}}, \hat{\mathbf{z}})$ coordinate system, and the corresponding $(\hat{\mathbf{h}}_i^b, \hat{\mathbf{v}}_i^b)$ and $(\hat{\mathbf{h}}_s^b, \hat{\mathbf{v}}_s^b)$ refer to the $(\hat{\mathbf{x}}_b, \hat{\mathbf{y}}_b, \hat{\mathbf{z}}_b)$ system. These polarization vectors can be obtained from the relations,

$$\hat{\mathbf{h}}_i = \hat{\mathbf{k}}_i \times \hat{\mathbf{z}}, \quad \hat{\mathbf{v}}_i = \hat{\mathbf{h}}_i \times \hat{\mathbf{k}}_i ; \qquad \hat{\mathbf{h}}_s = \hat{\mathbf{k}}_s \times \hat{\mathbf{z}}, \quad \hat{\mathbf{v}}_s = \hat{\mathbf{h}}_s \times \hat{\mathbf{k}}_s \qquad (A13)$$

where $\hat{\mathbf{k}}_s = - \hat{\mathbf{k}}_i$ for the case of backscattering. Similarly, we have

$$\hat{\mathbf{h}}_i^b = \hat{\mathbf{k}}_i \times \hat{\mathbf{z}}_b, \quad \hat{\mathbf{v}}_i^b = \hat{\mathbf{h}}_i^b \times \hat{\mathbf{k}}_i ; \qquad \hat{\mathbf{h}}_s^b = \hat{\mathbf{k}}_s \times \hat{\mathbf{z}}_b, \quad \hat{\mathbf{v}}_s^b = \hat{\mathbf{h}}_s^b \times \hat{\mathbf{k}}_s \qquad (A14)$$

Using Equations (A7) and (A8), we can find all the polarization vectors in Equations (A13) and (A14), which are then combined with Equation (A11) to obtain the required scattering matrix for backscatterings from

A-4

non-vertical branches. The final result is given in Equation (5-5) in the text.

Following the same procedure, we can derive the scattering matrix of forward scatterings by the non-vertical branches (for normal incidence waves), if $\hat{k}_s = \hat{k}_i$ is used in Equations (A13) and (A14). The final result is

$$
\mathbf{S}'(\theta, \theta_b, \pi) = Q \begin{bmatrix} \dfrac{\cos^2\theta_b}{\sin^2\theta} S_{hh} + \alpha S_{vv} & -\beta(S_{hh} - S_{vv}) \\[2em] -\beta(S_{hh} - S_{vv}) & \alpha S_{hh} + \dfrac{\cos^2\theta_b}{\sin^2\theta} S_{vv} \end{bmatrix} \tag{A15}
$$

where the α, β and $\sin \phi_b$ are the same as given in the text (see Equations 5-5 and 5-6). The S_{hh} and S_{vv} in Equation (A15) are defined in Equation (A12) with $\phi' = \pi$.
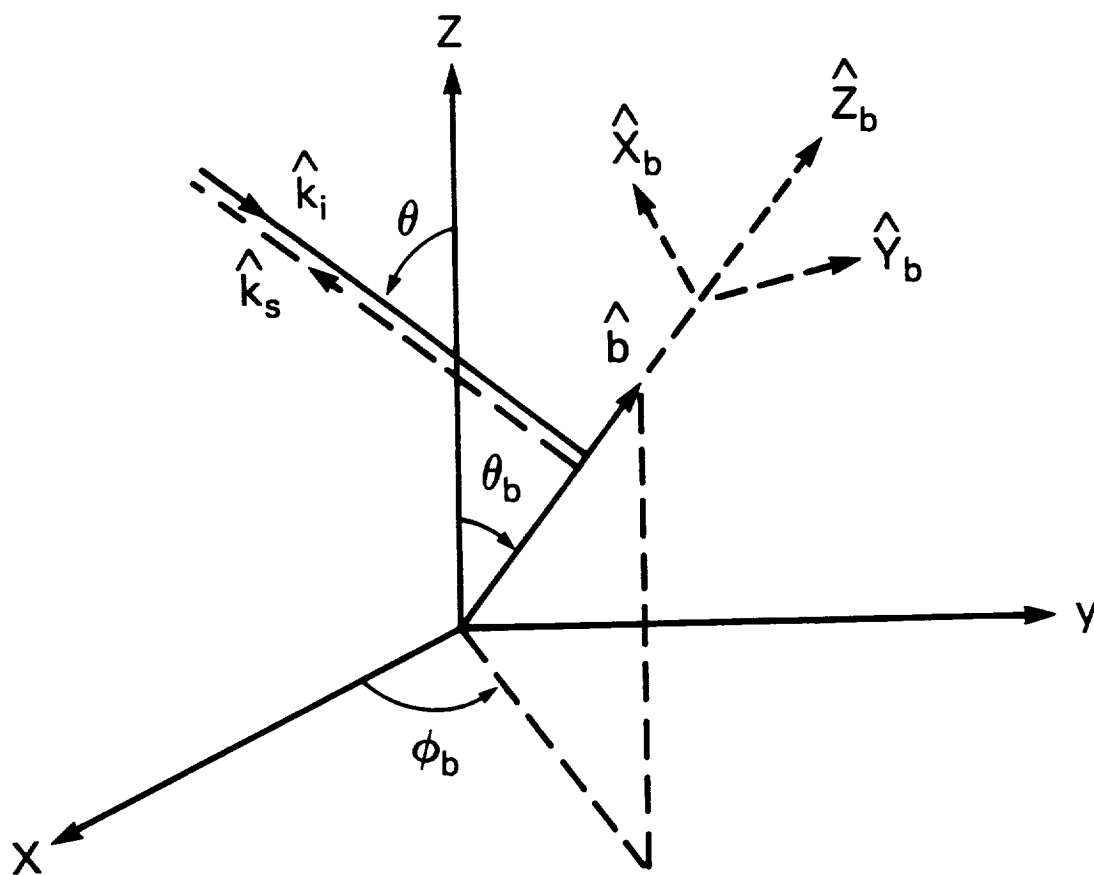
Figure A-1 Scattering geometry and coordinate systems used in the backscatterings of waves by non-vertical branches.

C-2

APPENDIX B - MULTIVIEW USER'S GUIDE

This user's guide was prepared to assist users of the modified version of the JPL MULTIVIEW software package (References 25 and 34) for processing the specific data acquired with the NASA/JPL SAR polarimeter. The JPL MULTIVIEW package consists of three independent parts, each of which may be executed separately. However, they are collectively required to process a set of the JPL compressed polarimetry data of polarization signatures and for proper calibration of an image file in co-polarization phases. The three parts in the package are:

- MULTIVIEW.FOR : The main program

- RECAL.FOR : Calibration of polarimetric image

- CREATE_TP.FOR : Create total power of Stokes Vector

The original JPL MULTIVIEW software package was modified at the Goddard Space Flight Center (GSFC) (Reference 34) and adopted for running on the VAX computer at the GSFC Ocean Laboratory.

For detailed description of the MULTIVIEW package, the users should refer to the JPL MULTIVIEW Guide (Reference 25). In this document,

we primarily provide the essential instructions which are required for executing the MULTIVIEW software package with the interactive Ocean VAX computer.

We start with reading data from the JPL tape of compressed polarimeter data and creating data file on disk. The created imaging data file is then re-calibrated in the co-polarization phase, using the RECAL.FOR program. From the calibrated imaging data file, one runs the CREATE_TP.FOR program to create a total-power image file.

After the imaging data are properly calibrated, the main MULTIVIEW program can be executed to perform various functions. In MULTIVIEW, there is a menu with 16 options which can be selected to perform appropriate studies of the polarimeter data.

The executable modules of all the programs are stored in the dataset OCEAN1$DUB2:[SIBTM.POLAR] at the Ocean VAX computer.

The followings are some examples for executing some of the modules. (User's inputs are printed in **bold** in the sessions)

B.1 Examples of Terminal Session

We illustrate the running of the individual MULTIVIEW programs by actual terminal sessions which show exactly what one would see on the

screen of the VAX terminals. Text entered by user is in **bold** face type. For questions which appear to have no answer, a carriage return will bring the default value into effect.

B.1.1 Get the Image files from the Tape

The JPL tape usually contains groups of 3 files for image data of P-, L-, and C-bands, respectively. In this example, the second file (L-band) is read off the tape and a image file named "L122888" is created on disk. It should be noted that the tape read program, TAP_READ, is a locally developed program which is written in IDL (Interactive Data Language) and is not part of the original MULTIVIEW software package. If you try to get the first file(P band), you can skip MTU (VAX Magnetic Tape Utility) and go directly to the DEFINE statement. The steps to get an image file are shown on the following VAX session lines.

$ MOUNT/FOREIGN MFA1

$ MTU

***** MTU - VAX/VMS Tape Processing Utility V5.0 *****

```
Enter INPUT tape drive  >  MFA1
Enter INPUT tape density (DEFAULT  =  6250) >
%MTU-W-DEVALMNT- You already have mfa1        mounted!
Do you choose to continue  < Y/N > ?Y
Enter OUTPUT tape drive (DEFAULT  =  6250) >
** Enter MTU function  >  SKIP

** WARNING - Next few questions refer only to INPUT tape MFA1

Enter number of records or files to skip  >  1
Enter type of skip ("?" will list options)  >  FF
A total of 1 records/files were skipped
```

```
** Enter MTU function  >  EXIT
MTU exiting


$ DEFINE MT1 MFA1
$ XIDL


VAX IDL, (C) Copyright 1983-1988, Research Systems, Inc.
Site  300, Licensed for use by: locf
IDL > @TAP_READ
      10240
Output filename

L122888
FILE OPENED SUCCESSFULLY
ASSOCIATED FILE SUCCESSFULLY
ABOUT TO READ TAPE
TAPE READ SUCCESSFUL
IDL > exit


$ DISMOUNT MFA1
```

B.1.2 Re-Calibration of Image Files

Image file created from the JPL polarimetric data tape requires re-calibration by renormalizing co-polarization difference to 0° for all pixels within a chosen area, which is normally a slightly rough soil surface. How to choose such an area is at users decision.

The **RECAL.FOR** program within the **MULTIVIEW** software package is used to re-calibrate the image file. The following example demonstrates the re-calibration of the image file **L122888** (created in B.1.1). The calibrated image file is named **L122888CALB** (output filename).

```
$ RUN RECAL
```

Filename of data to be recalibrated -- > **L122888**
File L122888
opened read-only on channel =   128

Output Filename -- > **L122888CALB**
File L122888CALB
 of size 20500 blocks created on channel =   144
 general scale factor: 5.4700092E + 07
 calibration factors are:
(1.000000,0.0000000E + 00) (0.7514449,0.6597958) (1.000000,0.0000000E + 00)
(1.000000,0.0000000E + 00)
Cursor defined window -- >
 enter the coordinates (x,y) of the top left corner:

100,100

 enter the coordinates (x,y) of the bottom right corner:

112,112

 window Up-Left: 100   100 Low-Right: 112   112
 is this okay (Y/n) ?
 computing the co-phase...
 number of points summed: 169
 estimated co-phase in degrees: 2.739639
 do you want a different window (y/N) ?
 enter expected co-phase in degrees:**0.0**
 updated calibration factors are:
(0.9988570,-4.7797505E-02) (0.9439604,0.3300586) (0.9271055,-0.3748003)
(1.000000,0.0000000E + 00)
        processing line: 50
        processing line: 100
        processing line: 150
        processing line: 200
        processing line: 250
        processing line: 300
        processing line: 350
        processing line: 400
        processing line: 450
        processing line: 500
        processing line: 550
        processing line: 600
        processing line: 650
        processing line: 700
        processing line: 750
        processing line: 800
        processing line: 850
        processing line: 900
        processing line: 950
        processing line: 1000

B.1.3 Create Total Power

Before running **MULTIVIEW**, it is necessary to run the program **CREATE_TP.FOR** once for each compressed data set. The program **CREATE_TP.FOR** creates a 512 × 512 total-power image and stores it on the disk in a file with the same name as the compressed data set but with the extension '.TP.' MULTIVIEW expects a compressed data set to have a corresponding '.TP' file with a pre-calculated total-power image.

The following terminal session illustrates the process of running **CREATE_TP.FOR** to create a total power image named **L122888.TP** .

$ RUN CREATE_TP

Select IIS device 0 or 1 -- > **0**
%SYSTEM-S-NORMAL, normal successful completion

Input Filename -- > **L122888CALB**
File L122888CALB
 opeed read-only on channel = 144
File L122888CALB.tp
 of size 512 blocks created on channel = 160

Scale Factor (> 1.0 yields brighter picture) -- >

A default scale factor of 1.0 will be used...

Computing scale factor of image...

Drawing initial image (total power)...
1024

B.2 Running MULTIVIEW

The 16 options in the **MULTIVIEW** program are:

1) Change current image size (256)
2) Change current zoom factor (1)
3) Erase an image
4) Plot an image, given a polarization chosen from signature
5) Plot an image, given an arbitrary polarization
6) Compute a new polarization signature
7) Toggle signature display (T)
8) Change current scale factor (1.0000)
9) Toggle snap-to-grid mode (T)
10) Display and Write 3-D signatures to disk files
11) Find local maximum or minimum in polarization signature
12) Find maximum or minimum in polarization signature
13) Delete a polarization signature
14) Compute ratio of two signatures
15) Roam (512x512) window in (1024x1024) virtual display
16) Quit

Option 6 is used to compute new polarization signatures and option 10 to create 3-D plots of co-polarization and cross-polarization signatures. Options 10 also creates two datasets for storing data for plots. All other options are described in Reference 25 in detail.

The following example shows a **MULTIVIEW** running session that creates a set of 3-D plots:

S RUN MULTIVIEW

< < <   Welcome to MULTIVIEW, Version 1493.27   > > >

Recover Mode (y/N) -- > **N**

Select IIS device 0 or 1 -- > **0**

%SYSTEM-S-NORMAL, normal successful completion

Input Filename -- > **p122888calb**
File p122888calb
 opened read-only on channel =   176
File p122888calb.tp
 opened read-only on channel =   192

Scale Factor (> 1.0 yields brighter picture) -- >

A default scale factor of 1.0 will be used...

Computing scale factor of image...

Drawing initial image (total power)...

%SYSTEM-S-NORMAL, normal successful completion

     MAIN MENU

1) Change current image size (256)
2) Change current zoom factor (1)
3) Erase an image
4) Plot an image, given a polarization chosen from signature
5) Plot an image, given an arbitrary polarization
6) Compute a new polarization signature
7) Toggle signature display (T)
8) Change current scale factor (1.0000)
9) Toggle snap-to-grid mode (T)
10) Display and Write 3-D signatures to disk files
11) Find local maximum or minimum in polarization signature
12) Find maximum or minimum in polarization signature
13) Delete a polarization signature
14) Compute ratio of two signatures
15) Roam (512x512) window in (1024x1024) virtual display
16) Quit

Choose one -- > **6**

Cursor defined area (Y/n) -- > **N**

Upper-Left X,Y of area in original 1024 image -- > **100,100**
Lower-Right X,Y of area in original 1024 image -- > **112,112**

Some of the pixels being looked at:
%SYSTEM-S-NORMAL, normal successful completion
  62 56 40 37 56 64 65
  54 44 57 57 73 68 54
  82 72 43 66 63 51 52
  76 52 54 50 45 41 38
  59 48 62 77 61 45 42
  51 51 38 49 47 69 52
  57 49 39 46 45 58 64

Is this ok (Y/n) -- > **Y**

%SYSTEM-S-NORMAL, normal successful completion
Upper-Left Corner of subset is at   100   100

Drawing Signatures...

        MAIN MENU

1) Change current image size (256)
2) Change current zoom factor (1)
3) Erase an image
4) Plot an image, given a polarization chosen from signature
5) Plot an image, given an arbitrary polarization
6) Compute a new polarization signature
7) Toggle signature display (T)
8) Change current scale factor (1.0000)
9) Toggle snap-to-grid mode (T)
10) Display and Write 3-D signatures to disk files
11) Find local maximum or minimum in polarization signature
12) Find maximum or minimum in polarization signature
13) Delete a polarization signature
14) Compute ratio of two signatures
15) Roam (512x512) window in (1024x1024) virtual display
16) Quit

Choose one -- > 10

creating CO-polarization signature file: p122888calb.COPS
creating CROSS-polarization signature file: p122888calb.CRPS
Drawing 3-D Signature...

The program creates two output files (named P122888CALB.COPS and P122888CALB.CRPS), which contain the 3-D plot coordinates on the VAX system. One can transfer the files to the IBM SCFMVS system by using the following commands.

$ COPY P122888CALB.COPS SCFMVS:: < USRID > ANY.COPS

$ COPY P122888CALB.CRPS SCFMVS:: < USRID > ANY.CRPS

Then, two datasets are created under your ID on IBM disk.

B.3 Produce 3-D Plots on IBM

The data transferred to IBM computer can be plotted, using the Template Graphic Plotting Subroutines. A software package for plotting the polarization signatures in 3-d surface form was developed. The 3-d plots presented in this report were generated by this software package.

The following JCL program shows how to execute a program OPTICSMD, that requires two subroutines named PHOPTICS and GAUSS, respectively.

```
//USRIDOPT JOB (xxxxx,V678,10),'PHY.OPTICS MOD',TIME=(1,59),
// MSGCLASS=A,NOTIFY=USRID
// EXEC G38PLOT,PARM.FORT='NOMAP,NOXREF',
//        PARM.LKED='NOMAP,NOXREF',REGION.GO=0K
//FORT.SYSIN DD DSN=USRID.dsn(OPTICSMD),DISP=SHR
//        DD DSN=USRID.dsn(PHOPTICS),DISP=SHR
//        DD DSN=USRID.dsn(GAUSS),DISP=SHR
//LKED.SYSLIB DD
//        DD
//        DD DSN=SYS2.IMSLD,DISP=SHR
/*
```